Doctor of Philosophy

PLASMONIC NANOANTENNAS FOR EFFICIENT INFRARED (IR) ABSORBERS, DETECTORS, AND ENERGY HARVESTING DEVICES

The Graduate School

of The University of Ulsan

Department of Electrical, Electronic and Computer Engineering

MOHAMAD KHOIRUL ANAM

PLASMONIC NANOANTENNAS FOR EFFICIENT INFRARED (IR) ABSORBERS, DETECTORS, AND ENERGY HARVESTING DEVICES

Supervisor: Prof. Choi Sangjo

A Dissertation

Submitted to

the Graduate School of the University of Ulsan

In partial Fulfillment of the Requirements

for the Degree of

Doctor of Philosophy

by

MOHAMAD KHOIRUL ANAM

Department of Electrical, Electronic and Computer Engineering
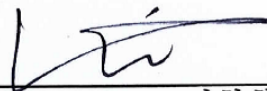
University of Ulsan, Republic of Korea

August 2022

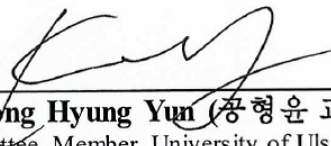# PLASMONIC NANOANTENNAS FOR EFFICIENT INFRARED (IR) ABSORBERS, DETECTORS, AND ENERGY HARVESTING DEVICES

This certifies that the dissertation of Mohamad Khoirul Anam is approved.
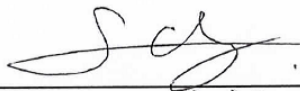
Prof. Choi Sangjo (최상조 교수)
Committee Chair, Kyungpook National University

Prof. Kim Hyeon Cheol (김현철 교수)
Committee Member, University of Ulsan, Advisor

Prof. Kong Hyung Yun (공형윤 교수)
Committee Member, University of Ulsan

Prof. Song Jiho (송지호 교수)
Committee Member, University of Ulsan

Prof. Park Jong Eon (박종언 교수)
Committee Member, Korea Maritime and Ocean University

Department of Electrical, Electronic and Computer Engineering

University of Ulsan, Republic of Korea

August 2022

VITA

MOHAMAD KHOIRUL ANAM was born in Lamongan, Indonesia, on 11th June 1990. He received B.Sc degree from Department of Physics, Faculty of Mathematics and Natural Sciences, Gadjah Mada University (UGM), Indonesia, in 2013. Since 2014, He has been working at the Research Center for Testing Technology and Standard, the National Research and Innovation Agency of Republic Indonesia (BRIN, formerly known as LIPI). In 2017, He became a Junior Researcher and a member of the applied electromagnetic research group. In March 2018, He pursued the M.S. and Ph.D. combined degree program in the Department of Electrical/Electronic and Computer Engineering, University of Ulsan, the Republic of Korea, under the supervision of Professor Choi Sangjo. His main research interests include the design and optimization of plasmonic nanoantennas for efficient infrared (IR) absorbers, detectors, and energy harvesting devices.

To my parents: Bpk. Kasdi and Ibu. Tasimah

To my parents in law: Bpk. Nurhaji and Ibu. Ucik Windarti

To my wife: Hilda Pasca Bella

To my children:

Muhammad Al-muqaffa Rusydan Dhiyaullah

Muhammad El-raffasya Rizhan Dhiyaullah

Raihannah Humaira Qianan Dhiyaunnisa

ACKNOWLEDGEMENT

ABSTRACT

PLASMONIC NANOANTENNAS FOR EFFICIENT INFRARED (IR) ABSORBERS, DETECTORS, AND ENERGY HARVESTING DEVICES
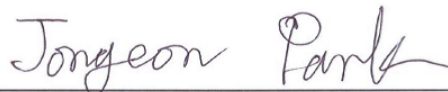
By. Mohamad Khoirul Anam

An infrared (IR) radiation contributes almost half of the total solar radiation, and such a large IR energy density is only suspected as thermal wasted energy. This increases the opportunity to use IR radiation in various fields such as thermography, heating, night vision, and communications. However, the investigation of converting IR radiation into another form of energy, such as electricity, has not been done before. Therefore, the IR detection method is needed to capture the IR radiation and convert it into another form of energy. Previously, thermal and photon were the common method to detect IR radiation, but these methods suffer from several limitations, such as low detectivity and slow response time. Therefore, an alternative approach for detecting IR radiation with high sensitivity is needed to overcome those limitations. Recently, nanoantenna has attracted significant attention due to their distinctive properties, such as high absorption and field confinement at terahertz frequency range. These characteristics enable the antenna to be widely used to improve the performance of optical and IR detectors by increasing the detector's photoresponse due to electric energy enhancement. Accordingly, this dissertation emphasized designing nanoantenna with high field enhancement and absorption rate. For application as IR harvesting devices, we developed a thermoelectric nanoantenna with high current density at the antenna center and fabricated the antenna using a common nano-fabrication technique. Finally, nanoantenna measurement was done using an IR measurement set up to determine the fabricated thermoelectric nanoantenna's open-circuit voltage (V_{oc}).

First, we proposed a bowtie nanoantenna array integrated with an artificial impedance surface to achieve high field enhancement and perfect absorption at the same time. We implement the artificial impedance surface as a metallic patch array on a

grounded 50 nm-thick SiO_2 substrate with reactive impedance surface (RIS) or high impedance surface (HIS) characteristic. We designed a bowtie nanoantenna array on an optimum RIS patch array through the proposed design method. We achieved a high field enhancement factor (E/E_0) of 228 and a nearly perfect absorption rate of 98% at 230 THz. This novel design outperforms the previously reported nanoantenna structures and the same bowtie nanoantenna array designed using a conventional grounded SiO_2. We also show that the HIS-integrated bowtie antenna array cannot realize both goals at the same time because the highly reactive HIS cannot guarantee perfect absorption. The proposed RIS-combined nanoantenna array with high field enhancement and near-perfect absorption can be used for efficient infrared (IR) and optical detectors, sensors, and energy harvesting devices.

Second, we proposed a new structure of MIM (metal insulator metal) based IR absorber to overcome the low field enhancement from the standard MIM absorber structure. The proposed absorber uses a reactive impedance surface (RIS) to boost field enhancement without an ultra-thin spacer and maintains near-perfect absorption due to impedance-matching with the vacuum. Unlike conventional metallic reflectors, the RIS is a metallic patch array on a grounded dielectric substrate that can change its surface impedance. The final circular nanodisk array mounted on the optimum RIS offers an electric field enhancement factor of 180 with a nearly perfect absorption of 98% at 230 THz. The proposed absorber exhibits robust performances even with a change in polarization of the incident wave. The proposed RIS-integrated MIM absorber with such good performance can enhance the sensitivity of a localized surface plasmon resonance sensor and surface-enhanced infrared spectroscopy.

Last, for IR energy harvesting application, we designed a novel thermoelectric bowtie nanoantenna with a high Seebeck effect and utilized the maximum resonances from the vertical and horizontal dimensions of a SiO_2 substrate instead of the membrane. The bowtie nanoantenna was made with a single metal, titanium (Ti), without a thermal conductivity discontinuity at the antenna center to lower the heat spread. Then, a nickel (Ni)-Ti bimetal nano-thermocouple with a high Seebeck coefficient gradient was connected at the center. Finally, the nanoantenna utilized a quarter wavelength-thick SiO_2 backed by a metal reflector and an optimum lateral size of the open-ended SiO_2 to launch the maximum signal peak of standing waves at the antenna center. The simulation results showed the highest V_{oc} of 2.06 μV from a temperature gap (ΔT) of 76.33 mK among the

state-of-arts of substrate-mounted thermoelectric nanoantenna operating at $\lambda_0 = 10.6$ μm. For proof of concept, we fabricated the thermoelectric nanoantennas using typical nano-lithography and deposition methods and showed a similar V_{oc} of 2.03 μV using a CO_2 laser-based IR measurement system. In conclusion, we expect that the proven thermoelectric nanoantenna design with the highest V_{oc} from the novel antenna topology and the engineered substrate can be used for a high DC output massive nanoantenna array.

TABLE OF CONTENTS

LIST OF FIGURES

xvi

LIST OF TABLES

LIST OF ABBREVIATIONS

IR	:	Infrared
AMC	:	Artificial magnetic conductor
HIS	:	High impedance surface
RIS	:	Reactive impedance surface
THz	:	Terahertz
HFSS	:	High frequency structure simulator
FEM	:	Finite element method
PBC	:	Periodic boundary condition
PEC	:	Perfect electric conductor
PMC	:	Perfect magnetic conductor
PML	:	Perfectly matched layer
LSP	:	Localized surface plasmon
PCs	:	Photonic crystal
MIM	:	Metal insulator metal
LSPPs	:	Localized surface plasmon polaritons
LSPR	:	Localized surface plasmon resonance
FTIR	:	Fourier transform infrared
EBL	:	Electron beam lithography
FIB	:	Focussed ion beam
ALD	:	Atomic layer deposition
RIE	:	Reactive ion etching
BOE	:	Buffered oxide etch
SNOM	:	Scanning near-field optical microscopy
PTFE	:	Polytetrafluorosthylene
PECVD	:	Plasma enhanced chemical vapor deposition
IPA	:	Isopropyl alcohol
PR	:	Photoresists
SEM	:	Scanning electron microscope

Chapter 1

Introduction

1.1 Background

Infrared (IR) radiation (~700 nm to ~1 mm) is a part of electromagnetic radiation with a wavelength longer than visible light but shorter than radio waves [1]–[3]. The IR radiation with a longer wavelength ranging from 30 μm to 100 μm is also considered as a terahertz (THz) radiation or terahertz waves [4]. The IR radiation was discovered by William Herschel in 1800 by dispersing sunlight through transparent prims and measuring the temperature for each color in the visible spectrum. He found that IR radiation is an invisible light in the spectrum and has lower energy than red light [5]. Generally, every object emits IR radiation at a different level; however, the common natural sources of IR radiation are heat generated by solar radiation and fire [6], [7]. The IR energy emitted by an artificial source such as heating devices is also considered as IR radiation [8], [9]. This radiation covers a wide range of wavelengths in the electromagnetic wave spectrum, where the IR energy is determined by the temperature and surface property of the objects [10], [11]. In addition, all objects with a temperature over 0 K also radiate IR energy; for example, the human body radiates IR radiation with a wavelength near 10 μm at a temperature of 310 K (37°C) [12], [13]. Recently, the IR radiation is widely used in various fields such as tomography [14], [15], thermography [16]–[18], night vision [19], [20], imaging [21], [22], heating [23], [24], and communications [25], [26]. However, IR radiation is rarely investigated and used to be converted into other forms of energy such as electricity. On the other hand, IR radiation contributes almost the half of the solar radiation that falls to the Earth's surface and radiate in the form of terrestrial radiation [27]. Moreover, such a large IR energy flux is usually considered as thermal waste and is not used for massive practical applications; thus, this increases the opportunity for researchers to develop a method or device for harvesting IR radiation. To achieve that purpose, the IR detection method is needed to capture the IR radiation and convert it into another form of energy.

Generally, there are two types of IR detection methods, i.e., thermal and photonic [28]–[30]. The thermal IR detector works based on the absorption of IR radiation that can change the temperature of materials; therefore, the response of the thermal IR detector depends on the material properties. The thermal IR detector operates in a room temperature and covers a wide range of IR wavelengths; however, this detector suffers from low detectivity because it is affected by the surrounding temperature condition [31], [32]. The sensitivity of the thermal-based IR detector can be increased by thermally insulating the detector from ambient temperature; unfortunately, the increased sensitivity has an impact on increasing response time [33], [34]. Meanwhile, the photon-based IR detection method mainly works based on the semiconductor concept. In this method, the absorbed IR radiation by the semiconductor material will generate an electrical signal due to the difference in electron energy density distribution from the electron interaction [35]–[37]. This allows the photon-based IR detector to exhibit a good signal-to-noise ratio and fast response performance. However, cryogenic cooling is needed to achieve such performance, and the cooling requirement makes the detector bulky and expensive; thus, this cooling stuff can be the main drawback for their broader use as an IR detector system [38], [39]. Therefore, an alternative IR detection method is needed to overcome these drawbacks and realize compact devices with a good detection performance, such as better sensitivity, absorptivity, and fast responses. In this regard, nanometer-sized metallic antenna so-called nanoantenna with high IR frequency selectivity and enhanced localized field can be a viable option for realizing the efficient and cooling-free IR detector [40]–[42].

Recently, the nanoantenna has been exploited as a promising device to enhance the performance of optical and IR detectors [43]–[45]. The performance enhancement of the nanoantenna coupled IR detector is marked by the increase of photoresponse due to the rise of electric energy density and high absorption from the nanoantenna [43]. Therefore, field enhancement and perfect absorption are the critical parameters to enhance the sensitivity of IR detector-based nanoantenna. Generally, the field enhancement of the nanoantenna can be improved by narrowing the distance between two nano-shaped structures to launch in-plane coupling [46]. Another method to enhance nanoantenna's field enhancement is using far-field coupling from an array structure; the in-phase coupling between localized surface plasmon (LSP) from the individual antenna and the scattered wave from the array leads to an optimum electric field enhancement [47].

However, the nanoantenna with optimum electric field enhancement exhibits low absorption efficiency due to the absence of magnetic field energy. To increase the absorption efficiency, an ultra-thin grounded dielectric substrate is used to generate magnetic responses that trap the incident waves [48]–[50]. Nevertheless, nanoantenna on ultra-thin dielectric shows low electric field enhancement due to the antennas current and its image in the bottom reflector canceling each other [48]. Based on the aforementioned reasons, the conventional nanoantenna design method cannot realize high field enhancement and a perfect absorption simultaneously. To resolve this issue, we utilized the high impedance surface (HIS) and reactive impedance surface (RIS) to change the surface impedance along the IR frequency range. Unlike a common reflector, HIS and RIS show high surface impedance and surface reactance, respectively, at a resonant frequency [51], [52]. This feature enables them to be integrated with nanoantennas by optimizing the HIS and RIS with the desired resistive and inductive features. One part of this dissertation introduces a detailed method to realize both high field enhancement and absorption rate in a nanoantenna design using HIS and RIS. Further, the possibility of nanoantenna application as IR detectors and energy harvesting devices will be discussed.

The proposed nanoantenna design method for high field enhancement and absorption rate using HIS and RIS is briefly described as follows. First, the geometry of a single antenna, such as antenna length and thickness should be optimized to achieve high field enhancement. One thing that should note is that the optimum substrate thickness might be different than the optimum thickness for antenna design in radio-frequency (RF). In the RF antenna, the in-phase coupling between the incident and reflected from a quarter-wavelength substrate thickness increases antenna radiation efficiency [53]. However, in the THz regime, the low conductivity and metal skin effect from the bottom reflector change the optimum substrate thickness due to improper reflection; thus, the substrate thickness should also be optimized to achieve optimum field enhancement [54]. Second, the nanoantenna with optimum geometry is arranged in a two-dimensional array. The optimum array pitch should also be determined to provide in-phase coupling between the localized surface plasmon (LSP) from the individual antenna and the scattered waves from the array. Finally, the nanoantenna with the optimum pitch size was combined with the optimized HIS and RIS, and the field enhancement and absorption rate were calculated and analyzed through numerical simulations.

Next, we also investigated a design method of an IR absorber using RIS to improve the absorption efficiency and increase field enhancement. Metal insulator metal (MIM) based absorber is the most common effective IR absorber due to their simple design and superior performance, such as high absorption efficiency in the IR regime [55]. However, low field enhancement due to current cancellation makes the MIM structure limited in applications. Therefore, the integration of RIS with MIM absorber needs to be investigated to achieve perfect absorption with high field enhancement at the IR regime. In the end, the performance of the RIS-based IR absorber is analyzed, and the possibility of polarization-independent responses are also investigated.

Further, we investigated nanoantenna structures integrated with rectification devices for energy harvesting purposes. Despite their application for IR detector performance enhancement, several types of nanoantennas such as dipole, bowtie, and spiral, are recently investigated and optimized as alternative devices for energy harvesting purposes [56]. The dipole-shaped nanoantenna offers several advantages, including simplicity in fabrication and high field confinement in the antenna gap. An ultra-fast rectifier coupled to the antenna is required to generate a DC signal. Generally, a tunnel diode based on metal oxide metal (MOM) is frequently used as a rectifying device to rectify the THz radiation [57], [58]. Another type of rectification system uses a metal insulator metal (MIM) diode, formed by sandwiching an ultra-thin insulator between the overlapping area of dipole antenna arms [59]. This configuration generates a DC output signal due to electron tunneling driven by the high field enhancement from the sharp tip of the bowtie nanoantenna. In the implementation, a structure with high responsivity is needed for high rectification efficiency. The common method to improve the efficiency is by increasing the DC current per unit power of the incident waves, which can be done by increasing barrier height. However, higher barrier height makes the structure suffer from high DC resistance, thus, lowering rectification efficiency.

Another method to rectify the IR radiation is thermoelectric nanoantenna, this device is used due to its capability of direct conversion from IR radiation to electricity without requiring additional converting devices. The antenna consists of a dipole antenna to capture IR radiation and a combined nano-thermocouple to convert the induced antenna current into electricity. The conversion mechanism is based on the Seebeck effect, which generates an open-circuit voltage (V_{oc}) due to the temperature difference (ΔT). For optimum V_{oc}, the antenna should be optimized to generate high temperature at the antenna

center. Also, the antenna's material with low thermal conductivity is needed to avoid heat transfer and maintain a high temperature at the antenna center. Moreover, the coupling between the antenna's electric fields and standing waves from the open-ended grounded dielectric substrate determine the ΔT; thus, the lateral substrate size optimization is required in our proposed thermoelectric nanoantenna to achieve optimum ΔT. Lastly, the fabricated thermoelectric nanoantenna is measured using an IR measurement system, and the device performance is investigated and analyzed.

1.2 Research Objective

This dissertation focuses on designing nanoantenna for efficient infrared (IR) absorbers, detectors, and energy harvesting devices using a numerical simulation and verification in the experiment. In detail, the objectives of this dissertation are detailed below:

a. To design a nanoantenna array with a high field enhancement and absorption rate using numerical simulations. Instead of using a common metallic reflector, we use an artificial impedance surface that can behave like a high impedance surface (HIS) and reactive impedance surface (RIS).

b. To apply the method mentioned above for an IR absorber based on metal insulator metal (MIM) structure to achieve near-perfect absorption with high field enhancement.

c. To design a thermoelectric nanoantenna that consists of a single metal bowtie nanoantenna and a bimetal nano-thermocouple with high current density at the antenna center for the energy harvesting purpose.

d. To fabricate the proposed thermoelectric nanoantenna design using the nanofabrication techniques such as electron beam lithography, electron beam evaporation, and UV lithography.

e. To investigate the output voltage (V_{oc}) response from the fabricated thermoelectric nanoantenna device by illuminating the devices with an external IR radiation in an IR measurement setup.

f. To demonstrate the IR detecting performance of the thermoelectric nanoantenna by illuminating the structure with different IR radiation power levels.

g. To investigate the effect of the lateral substrate size on the V_{oc} response of the proposed device in regard to the excited standing waves on the substrate. The V_{oc} of the proposed thermoelectric nanoantenna device will be maximum when the antenna's electric field constructively coupled to the standing waves

1.3 Dissertation Outline

This dissertation presents a novel nanoantenna design to achieve high field enhancement and near-perfect absorption simultaneously. Instead of mounting the antenna over a grounded dielectric substrate, we combined the antenna with an artificial impedance surface that can behave like a high impedance surface (HIS) and reactive impedance surface (RIS) at a resonant frequency. For an IR energy harvesting application, we designed a thermal nanoantenna-combined nano-thermocouple to convert IR radiation into electricity. The antenna fabrication process, the measurement setup, and the antenna performance are also discussed.

1. Chapter 1 discusses the research background, and the objective of the research will be addressed with appropriate references at the beginning of the chapter.

2. Chapter 2 discusses a bowtie nanoantenna array integrated with an artificial impedance surface (AIS) to simultaneously achieve high field enhancement and a perfect absorption in the IR range. A high-frequency structure simulator (HFSS) is performed to determine optimum antenna parameters and calculate field enhancement and absorption rate. The high field enhancement and absorption rate were achieved due to the antenna gap's capacitance cancellation by the inductive nature of the reactive impedance surface (RIS).

3. Chapter 3 discusses perfect IR absorbers based on MIM (metal-insulator-metal) structure with high field enhancement using a circular nanodisk array combined with the reactive impedance surface (RIS). The near-perfect absorption with high field enhancement was achieved due to impedance matching between the structure and vacuum. Additionally, the discussion about a polarization-independent response from the proposed absorber is presented.

4. Chapter 4 discusses a single metal nanoantenna combined with a bimetal nano-thermocouple for IR detector and energy harvesting applications. The antenna design utilizes COMSOL multiphysics 5.0, employing microwave heating and heat transfer module to calculate the antenna current density and temperature difference (ΔT) between hot and cold junctions, respectively. To achieve optimum ΔT at the resonant frequency, the antenna structure is optimized based on the coupling between antenna's electric field and standing waves from the open ended-substrate with a quarter-wavelength thickness.

5. Chapter 5 discusses an experimental method of the proposed thermoelectric nanoantennas, covering several common nano-fabrication techniques such as electron beam lithography (EBL), electron beam evaporation, UV lithography, and thin film deposition. Also, the detailed electrical and IR measurement setups will also be presented in this chapter.

6. Chapter 6 discusses thermoelectric nanoantenna measurement results and performance analysis of a single bowtie nanoantenna combined with a bimetal nano-thermocouple. First, we performed the electrical measurement for the device's DC resistance. Then, the open-circuit voltage (V_{oc}) measurement and a polarization-dependent response are discussed. Also, the effect of lateral substrate size on the V_{oc} response is shown. Finally, the performance comparison between the proposed single thermoelectric nanoantenna structure and the state-of-the-art single nanoantenna mounted on the grounded substrate is presented.

7. Chapter 7 discusses a summary of achievements, and the potential study for future works is introduced.

Chapter 2

Bowtie Nanoantenna Integrated with Artificial Impedance Surface (AIS) for High Field Enhancement and Absorption Rate

In this chapter, we evaluated the performance of a bowtie nanoantenna array integrated with an artificial impedance surface (AIS) and compared it to a conventional nanoantenna array mounted on a dielectric substrate. The AIS usage aims to achieve a high field enhancement and absorption rate simultaneously. In this study, the AIS was represented with a high impedance surface (HIS) and reactive impedance surface (RIS), which can change its surface impedance differently from the common metallic reflector. Numerical simulation using a high-frequency structure simulator (HFSS) based finite element method (FEM) was performed to calculate the electric field enhancement and absorption rate. The Drude model formula for the metal in the high frequency was used to calculate the electric field enhancement and the absorption rate of the proposed nanoantenna structure.

2.1 Introduction

Nanoantennas have been attracting attention as devices capable of concentrating and enhancing diffraction-limited light within subwavelength sizes and absorbing incident light efficiently [40]–[42]. Field enhancement on the nanometer scale from metallic nanoantennas is originated from the charge accumulation at the nanoantenna terminals due to localized surface plasmon resonance (LSPR) [60], [61]. The confined and enhanced fields of the nanoantenna can be used to excite fluorescent molecules and detect single molecules [62]. Additionally, with the high absorption rate, the nanoantenna can be used to improve the efficiency of infrared (IR) detectors [43], [63], plasmonic sensors [64], [65], surface-enhanced IR absorption spectroscopy [66], solar energy collection [67], and IR energy harvesting devices [59], [68]. To improve the field enhancement of the nanoantennas,

researchers have been actively utilizing three methods: 1) in-plane coupling between two metallic arms of the nanoantenna [46], [69], 2) out-of-plane coupling between the nanoantenna and its image using a dielectric spacer with a metallic reflector or film [70], and 3) coupling between nanoantenna elements using nanoantenna array structures [47], [71], [72]. Using the grounded spacer and the array structure, optimum geometric conditions such as spacer thickness and distance between nanoantennas in the array (array pitch) to maximize the field enhancement have been studied [48], [73], [74]. In [74], the spacer thickness of dipole nanoantenna is varied after fixing the array pitch to 600 nm and achieved the maximum field enhancement (E/E_0) of 89 at a wavelength of 880 nm with the spacer thickness of 60 nm, which is shorter than a quarter wavelength. However, the absorption rate was limited to 70% because the array pitch was not optimized for absorption improvement. Further, the optimum distance between nanoantenna elements in the array for the maximum field enhancement or absorption has been studied [75]–[79]. All of the array structures with an optimum array pitch exhibited field enhancement values (E/E_0) lower than 200 in the visible and IR range and the absorption was not perfect. Among them, the highest field enhancement value of ~160 from the bowtie nanoantenna array was shown near 700 nm wavelength when the distance between the nanoantennas is 425 nm [78]. Theoretical studies also showed that the maximum field enhancement and absorption rate occur at a certain array pitch in which the scattered waves from in the array and the localized surface plasmon (LSP) of each nanoantenna are coupled in-phase [80]–[82].

Furthermore, nanoantennas were designed with engineered resonant structures such as nanodisk arrays and photonic crystals (PCs) to maximize field enhancement via coupling between two different structures. Zhou *et al.* combined a bowtie nanoantenna with a hybrid nanoparticle array and provided a high field enhancement value of ~2×10^3 at a wavelength of 750 nm; however, this device was not optimized for high absorption [83]. In addition, Eter *et al.* integrated a bowtie-nanoantenna with a PC resonator and achieved a high field intensity > ~10^3 at 1272 nm without considering perfect absorption [84]. The high field enhancement values from both cases were possible partially due to the sharp tips of the antennas in addition to the coupling. Thus far, nanoantenna structures designed for the maximum field enhancement could not achieve perfect absorption due to dominant electric responses from the nanoantenna. For perfect absorption, a grounded ultra-thin dielectric layer can be used to induce magnetic response inside the substrate [48]–[50], [85]. A bowtie nanoantenna array backed by a grounded 5 nm-thick ($\lambda/200$) SiO_2 substrate showed perfect

absorption at 1035 nm wavelength because the LSP from the nanoantenna is coupled to the ground plane. However, the field enhancement factor for this device was limited to 86 [48]. Similarly, a metal patch array with a ~λ/150-thick dielectric spacer showed almost perfect absorption by trapping incoming waves via the induced magnetic dipoles inside the cavity; nonetheless, this device also suffered from a low field enhancement value [49], [50], [85]. The reason for the low field enhancement is that the current on the nanoantenna and its image cancel each other out due to the very thin substrate. To overcome this issue, a method of simultaneously achieving perfect absorption and high field enhancement was introduced. Instead of dipole-like nanoantenna structures, triangular nanodisks were mounted on the grounded 10 nm-thick Al_2O_3 substrates, allowing for a high absorption rate of 95% and a field enhancement value of 211 at the near-IR regime [86]. The structure used an ultra-thin substrate for perfect absorption and the field enhancement was boosted by the sharp tips of the triangle shape. However, the coupling strength in such an ultra-thin substrate can be significantly affected by the surface roughness of the bottom reflector [87].

In this chapter, instead of using an ultra-thin substrate with a metallic reflector, we utilized an artificial impedance surface to simultaneously fulfill the high field enhancement (> 200) and perfect absorption ($> 98\%$) of a bowtie nanoantenna array in the IR range. Here, the artificial impedance surface changes its surface impedance differently from the metallic reflector and this structure was chosen with a metallic patch array on a grounded substrate. Previously, the patch arrays have been used as the IR and optical absorbers [49], but they also have been used as a high impedance surface (HIS) and reactive impedance surface (RIS) to improve the antenna performance at microwave frequencies [51], [52], [88]–[90]. Because the HIS has a high surface impedance, even when the antenna is placed close to the surface, the current on the antenna and its image can be coupled in-phase. Thus, the radiation characteristic of the antenna can be improved [51], [88]. Meanwhile, the RIS can improve antenna impedance matching by offsetting the capacitive near-field characteristic of the antenna through its inductive surface impedance characteristic [52], [89], [90]. Recently, the RIS was utilized in a MIM (metal-insulator-metal) absorber design in the near-IR range and the structure showed the increase of field enhancement along with nearly perfect absorption due to the impedance matching between the structure and the vacuum [91].

In our study, we applied both HIS and RIS to bowtie nanoantenna design to achieve the maximum field enhancement and perfect absorption at the same time. The final bowtie nanoantenna array integrated with the optimum artificial impedance surface showed an

almost perfect absorption of 98% at 230 THz (λ = 1.3 µm) with a superior field enhancement factor (E/E$_0$) of 228. This field enhancement is ~1.4 times higher than the maximum value of ~160 from similar nanoantenna array structures [74]–[79]. The proposed device also showed perfect absorption without the use of an ultra-thin spacer and outperformed the triangular nanodisks-based ultra-thin structure in terms of field enhancement [86]. It should be noted that a high field enhancement value of 211 from the triangle-shaped structure is partially due to a very sharp tip, which is not utilized in the antenna terminal (gap) of our design.

In this chapter, we began with the design of a single bowtie nanoantenna on a grounded SiO$_2$ substrate and arranged the bowtie nanoantennas in a two-dimensional array. Then, we found the optimum pitch between the mountains in the array, allowing for the high field enhancement and absorption rate at 230 THz. Based on the optimum array pitch for the bowtie nanoantenna array, various metallic patch arrays for HIS and RIS were designed and integrated into the nanoantenna array. Finally, we exhibited the nanoantenna array coupled with an optimum artificial impedance surface that realizes the maximum field enhancement and perfect absorption at the desired wavelength and also analyzed the coupling phenomena between the artificial impedance surface and the nanoantenna structure.

2.2   Methods

The methods used in this study involve both numerical simulation and effective mode volume (V$_{eff}$) calculation. The numerical simulation section describes several parameters in the nanoantenna structure, such as material properties, detailed simulation methods, and field enhancement and absorption rate calculation. At the same time, the V$_{eff}$ calculation aims to quantify the effects of a high field excitation near the antenna structures on the field enhancement and confinement in the nanoantenna gap.

2.2.1 Numerical Simulation

In this study, gold and silicon dioxide (SiO$_2$) were used for modeling all the metallic elements and substrate material, respectively. We used the dielectric constants of SiO$_2$ in the near-IR region based on the previous experiments [92], [93]. The relative permittivity and conductivity of gold were calculated using the Drude model formula in (2.1) and (2.2), respectively. The angular plasma frequency (ωp) and the carrier scattering time (τ) are $2\pi \times 2080 \times 10^{12}$ rad/s and 18 fs, respectively [94], [95]. As a results, the relative permittivity

$$\varepsilon(\omega) = 1 - \frac{\omega_p{}^2 \tau^2}{1 + \omega^2 \tau^2} \tag{2.1}$$

$$\sigma(\omega) = \frac{\varepsilon_0 \omega_p{}^2 \tau}{1 + \omega^2 \tau^2} \tag{2.2}$$

(a) **(b)**
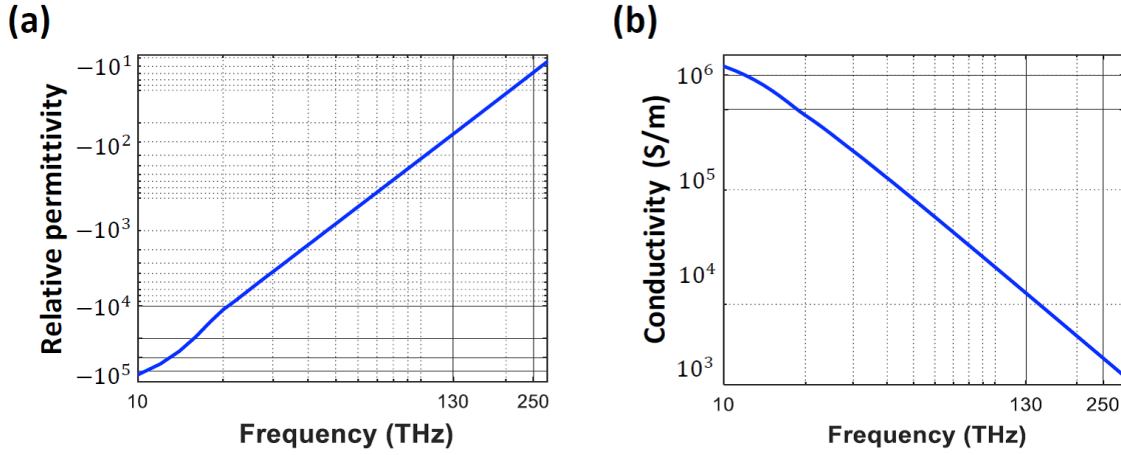
Figure 2.1. The relative permittivity and conductivity of gold as a function of frequency in the THz range.

For numerical simulation, high-frequency structure simulator (HFSS) based on the finite element method (FEM) was used. In the simulations for a single bowtie nanoantenna, radiation boundaries were used for all the six surfaces of the simulation boundary box. In addition, to model an infinite bowtie nanoantenna array, we used the master and slave boundaries on the y−z and x−z planes of the simulation boundary box, and radiation boundaries were assigned on the top and bottom of the box as shown in Figure 2.2. To calculate the field enhancement and absorption rate, the nanoantenna unit was illuminated with an x-polarized plane wave in a normal direction from the top. The electric fields from the structure is calculated using equation (2.3):

$$\nabla \times \left(\frac{1}{\mu_r} \nabla \times E \right) - k_o{}^2 \varepsilon_r E = \vec{J}_{source} \tag{2.3}$$

Where $k_o{}^2 = \omega^2 / c^2$. ε_r, μ_r and c are the permittivity, the permeability, and the velocity of light in vacuum. In this case, $\vec{J}_{source}$ represents of any source in the structure. The electric field enhancement was defined as (E/E_0), where E and E_0 are the magnitudes of the

electric fields at the center of the nanoantenna gap and the incident electric field, respectively. For accurate field calculations at the nanoantenna gap, mesh sizes smaller than 1 nm were used in the nanoantenna gap region within a volume of 20 nm × 20 nm × 10 nm. Using the reflected (P_r), transmitted (P_t), and incident (P_i) powers, the absorption rate of the nanoantenna array was determined using the equation $A = 1 - (P_r/P_i) - (P_t/P_i)$.
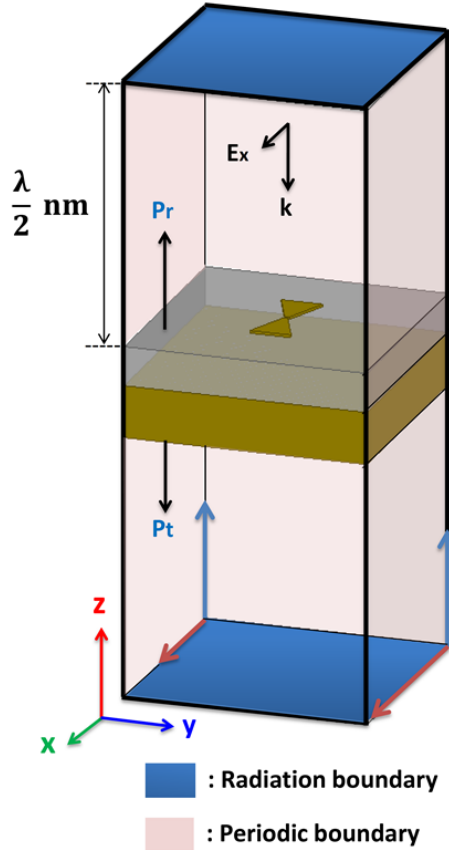
Figure 2.2. Schematic view of the nanoantenna array simulation using high-frequency structure simulator (HFSS) software.

In numerical simulations for the artificial impedance surface, the PEC and PMC boundaries along the y−z and x−z planes of the simulation boundary were used to model an infinite array of metallic patches. The magnitude and phase of the reflection coefficient of the patch array were calculated using wave ports. The surface resistance and reactance of the artificial impedance surface were determined from the reflection coefficient (Γ) using the equation (2.4). Here, Z_0 is the characteristic impedance of the vacuum.

$$Z_{surface} = \frac{1+\Gamma}{1-\Gamma} \times Z_0 \qquad (2.4)$$

Meanwhile, the capacitance in the nanoantenna gap was determined with voltage gap excitation in the gap inside the radiation boundary. Then, the input reactance (X_c) was converted to the nanoantenna gap capacitance (C) using equation (2.5):

$$C = \frac{1}{2\pi f_{res} X_c} \tag{2.5}$$

2.2.2 Effective Mode Volume (V_{eff}) Calculation

In this chapter, the effective mode volume (V_{eff}) of the bowtie nanoantenna array was calculated as the ratio between the total electromagnetic energy and the peak energy density [96], [97].

$$V_{eff} = \frac{U_m}{\mu_E(r_0)} = \frac{\int \mu_E(r) d^3 r}{\mu_E(r_0)} \tag{2.6}$$

Here, U_m is the total electromagnetic energy inside the simulation boundary and μ_E is the electric field energy density. The simulation boundary for calculating U_m was used with the boundary of the unit cell for the nanoantenna array. Thus, r includes all the points inside the boundary. In the denominator, r_0 is the position in which energy is concentrated in the system. Here, we chose r_0 to coincide with the center of the nanoantenna gap; this was because the nanoantenna array was used to maximize the field enhancement in the nanoantenna gap. For an accurate calculation for U_m, the energy density inside the metallic structures needs to be considered due to the nonnegligible field magnitude near the metal surface. Thus, the energy density inside the metal was calculated using equation (2.7) [98].

$$\mu_{E(metal)}(r) = \frac{1}{2}\left[\varepsilon_R + \frac{2\omega\varepsilon_I}{\gamma}\right]|E(r)|^2 \tag{2.7}$$

Here, $\varepsilon(\omega) = \varepsilon_R(\omega) + i\varepsilon_I(\omega)$ is the complex permittivity of the metal. ω, γ, and $E(r)$ are the angular frequency, Drude damping constant, and electric field magnitude at an arbitrary position (r), respectively. Additionally, the electric field energy density at a position, r in the dielectric medium was calculated using (2.8) [99].

$$\mu_{E(dielectric)} = \frac{\varepsilon_0}{2}\varepsilon_d|E(r)|^2 \tag{2.8}$$

where ε_d is the dielectric constant of the medium. $\mu_E(r_0)$ was calculated using (2.8) because r_0 is located inside the vacuum medium between the metallic nanoantenna arms.

2.3   Nanoantenna on SiO_2 Substrate

We started evaluating the performance of nanoantenna mounted directly on dielectric grounded substrates. First, a single nanoantenna was optimized to achieve high field enhancement at its center frequency of 230 THz (1.3 µm wavelength). Then, a two-dimensional array was designed using the optimized parameter from the single nanoantenna, and the array pitch size (P) was tuned to obtain optimum field enhancement and absorption rate. The simulation shows that the optimum array pitch size (P) is 1 µm, which is longer than half of the center wavelength (650 nm). This pitch array distance enables the in-phase coupling between the localized surface plasmon (LSP) from the individual antenna and the scattered field of the array.

2.3.1 Single Bowtie Nanoantenna
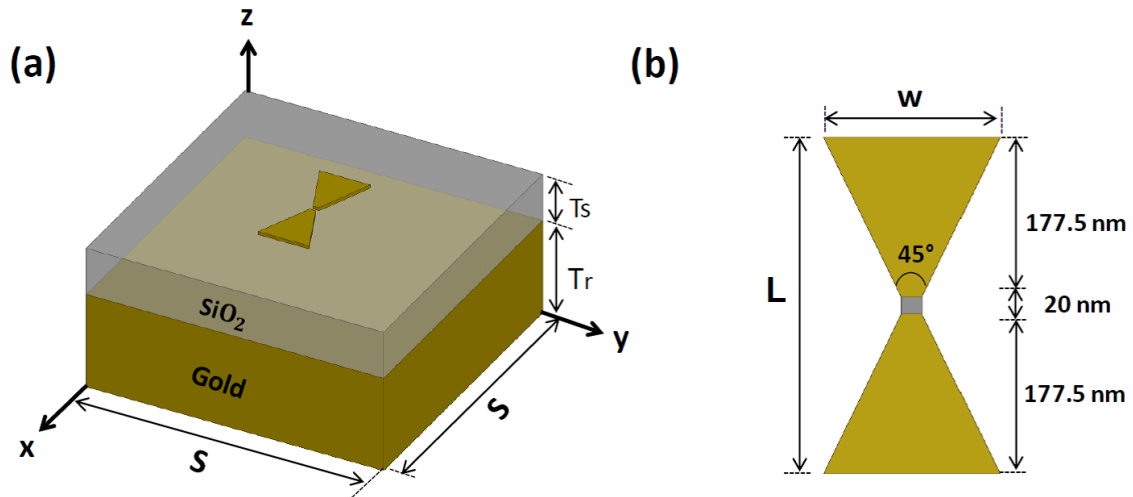
Figure 2.3. (a) Schematic view of the bowtie nanoantennas on a SiO_2 grounded substrate. (b) The detailed bowtie nanoantenna structure.

A single bowtie nanoantenna was designed on a SiO_2 substrate supported by a gold reflector and its center wavelength was chosen with 1.3 µm (230 THz in frequency). The detailed design of the proposed nanoantenna is presented in Figure 2.3. Here, L, w, and T_s are the nanoantenna length, width, and the SiO_2 substrate thickness, respectively. The nanoantenna air gap volume between two nanoantenna arms was fixed with 20 nm × 20 nm × 10 nm, and the thickness of the nanoantenna of 10 nm and the bowtie shape's angle of 45° were used. The substrate size (S) was set to a wavelength size (1.3 µm) such that diffraction from the edges does not change the resonant frequency of the nanoantenna. A

200 nm-thick gold reflector (T_r), which is much thicker than the metal skin depth at 230 THz, was used for proper reflection [100]. For excitation, an x-polarized plane wave with a field intensity of 1 V/m (E_0) was normally incident from above the nanoantenna and a field enhancement factor was calculated using E/E_0, where E is the electric field intensity at the center of the nanoantenna gap. With the given dimensions and excitation, we varied the nanoantenna length (L) and the SiO_2 substrate thickness (T_s) and calculated the field enhancement factor.
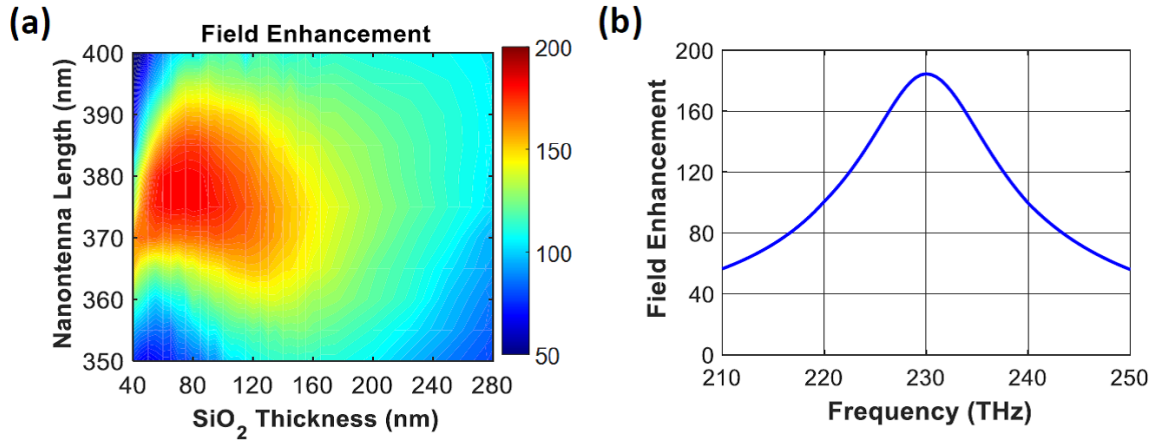
Figure 2.4. (a) The field enhancement at 230 THz with a single bowtie nanoantenna as a function of nanoantenna length (L) and SiO_2 thickness (T_s). (b) The field enhancement values versus frequency for the bowtie nanoantenna with L = 375 nm and Ts = 80 nm.

Field enhancement values at 230 THz as a function of the nanoantenna length (L) and SiO_2 thickness (T_s) are presented as a contour plot in Figure 2.4(a). From Figure 2.4(a), it can be seen that the maximum field enhancement at 230 THz is achieved when L and T_s are 375 nm and 80 nm, respectively. Electric field enhancement of the corresponding bowtie nanoantenna versus frequency is shown in Figure 2.4(b), showing a maximum field enhancement of 183 at 230 THz. With the 80 nm-thick SiO_2 substrates, the LSP excited by the 375 nm-long bowtie nanoantenna was optimally coupled with its image in the reflector, allowing for the maximum field enhancement at the nanoantenna gap at 230 THz. It is important to note that the thickness (80 nm) of SiO_2 for achieving the maximum field enhancement lies between a quarter-wavelength inside SiO_2 (225 nm) and an ultra-thin thickness such as 40 nm, which indicates that the radiation and absorption are balanced. This result also means that the in-phase far-field coupling between the

nanoantenna and its image with a quarter-wave distance does not guarantee the maximum field enhancement in the nanoantenna gap.

2.3.2 Bowtie Nanoantenna Array

Using a single bowtie nanoantenna that maximizes the field enhancement at 230 THz, we designed a two-dimensional array using the master and slave boundaries and the array pitch was varied to find the optimum value for the maximum field enhancement and absorption rate. The field enhancement and the absorption rate of the nanoantenna array as a function of the array pitch and frequency are presented in figures 2.5(a) and 2.5(b). From Figures 2.5(a) and 2.5(b), it can be observed that as the pitch increases, the electric field enhancement increases and the resonance is redshifted. The absorption rate also exhibits a redshift, but a longer pitch provides a lower absorption rate near 230 THz. Because array pitches for the maximum field enhancement and the perfect absorption do not correspond to each other, we picked an optimum array pitch (P) of 1 μm for the balanced values in both parameters at 230 THz. One thing to note is that the optimum array pitch of 1 μm is longer than half of the center wavelength (650 nm), which is normally used as the optimum array distance between the microwave antennas to maximize radiation at the boresight. Previous studies also showed that the optimum pitch sizes in the nanoantenna arrays occur at lengths longer than half-wavelengths [75]–[79], [101]. In the optical nanoantenna array, the in-phase coupling between the LSP from the individual nanoantenna and the scattered field from the array determined the optimum array pitch for the maximum field enhancement and absorption [48], [101]. With the optimum array pitch (P), the electric field enhancement and absorption rate of the nanoantenna array versus frequency were calculated, as shown in Figures 2.5(c) and 2.5(d). The maximum values for the field enhancement and the absorption rate are 223 and 93%, respectively, at 230 THz. This maximum field enhancement of 223 from the bowtie nanoantenna array is higher than 184 from the single bowtie nanoantenna due to the aforementioned LSP and array resonance. It should be noted that the absorption rate is high but not perfect due to the 80 nm-thick substrate, which does not perfectly eliminate radiation loss.
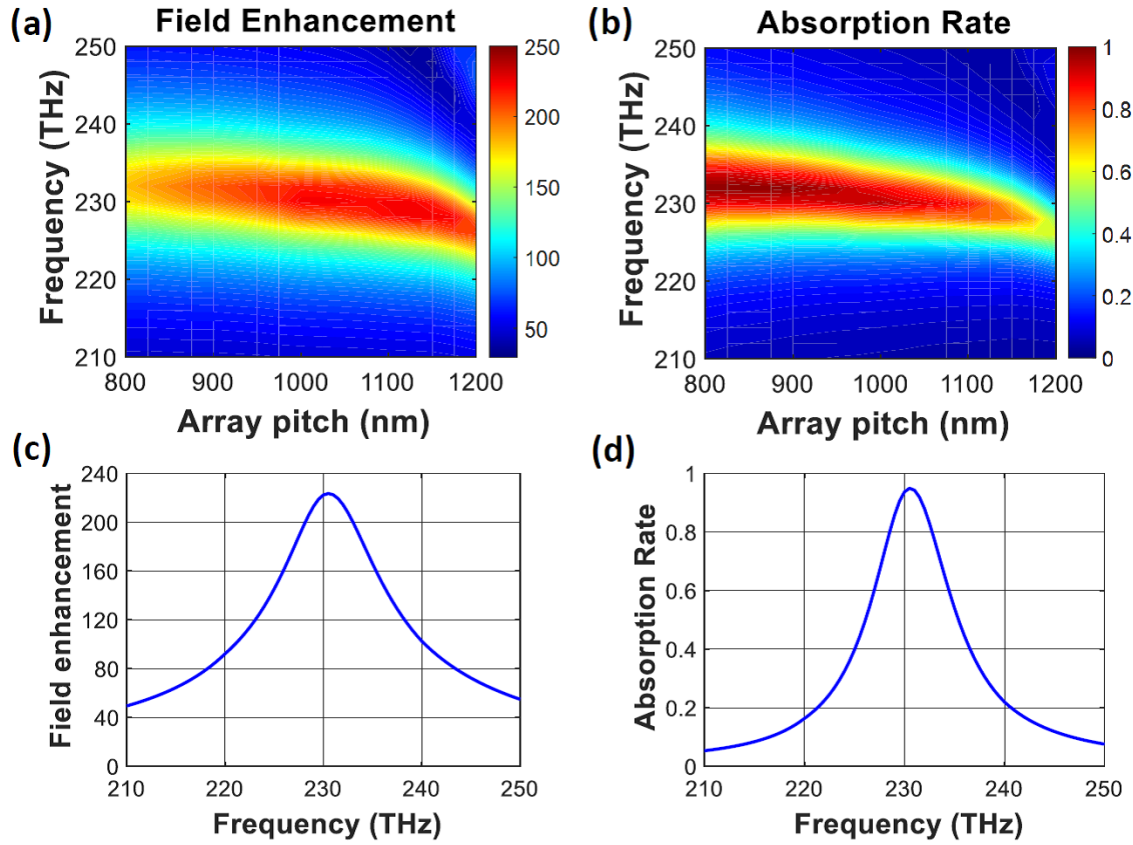
Figure 2.5. (a) The field enhancement and (b) absorption rate of the bowtie nanoantenna array on a grounded 80 nm-thick SiO$_2$ substrate as a function of the nanoantenna array pitch (P) and frequency. (c) The field enhancement and (d) absorption rate of the bowtie nanoantenna array with a 1 μm array pitch (P) with respect to frequency.

To compare the coupling between the antenna structure and the metallic reflector for both single nanoantenna and the nanoantenna array, we present the cross-sectional view of the z component of the electric field (E$_z$) along the antenna's central axis on the x−z plane in Figure 2.6. Figures 2.6(a) and 2.6(b) effectively show that the nanoantenna array exhibits higher coupling between the antenna and the metallic reflector; this is because the LSP of the individual nanoantenna is coupled to the scattered field from the nanoantenna array [48]. In addition, higher radiation near the edges of the single nanoantenna can be seen in Figure 2.6(a). Therefore, the stronger array coupling and the lower radiation resulted in higher field enhancement from the bowtie nanoantenna in the array.
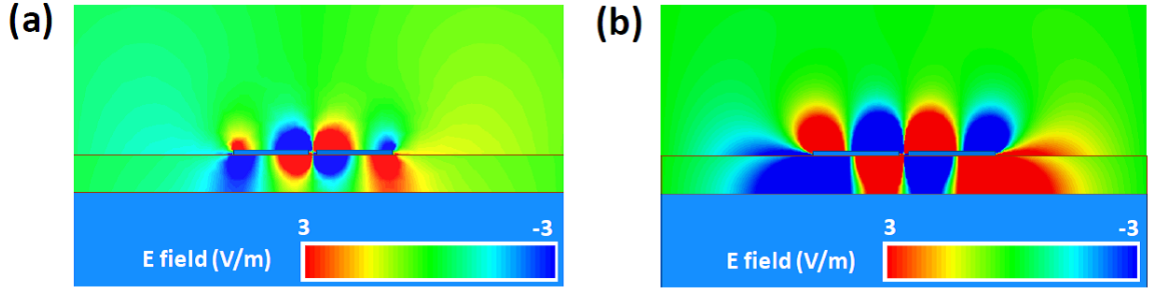
Figure 2.6. The z component of the electric field (E_z) along the antenna's central axis on the x-z plane for (a) the single bowtie nanoantenna on the grounded SiO_2 substrate with an area of 1.3 μm × 1.3 μm and (b) the bowtie nanoantenna array on the substrate with a 1 μm pitch (P). Note that an 80 nm SiO_2 thickness is used for both cases.

2.4   Artificial Impedance Surface (AIS)

To achieve high field enhancement and perfect absorption of the bowtie nanoantenna array at the same time, we utilized the artificial impedance surface in the form of a metallic patch array on a grounded 50 nm-thick SiO_2 substrate. On top of the patch array, a 50 nm-thick SiO_2 was placed as a spacer for the nanoantenna. Then, the top surface of the SiO_2 spacer was used as a reference plane for the calculation of the reflection coefficient. The patch arrays for HIS with high resistance and RIS with high reactance were designed to achieve 0° and 90° reflection phases, respectively, in the resonant frequency of 230 THz. The detailed simulation setup for the patch array is provided in Figure 2.7. The thickness of the metallic patch, the SiO_2 spacer thickness (t), and the metallic reflector thickness (T) were fixed with 10 nm, 50 nm, and 200 nm, respectively. Based on the optimum pitch (P = 1 μm) for the bowtie nanoantenna array, we chose four possible patch periodicities (D) that can be fitted inside the 1 μm × 1 μm area under the single bowtie nanoantenna. The patch periodicity values (D) were chosen as 100 nm, 125 nm, 200 nm, and 250 nm, such that 10 × 10, 8 × 8, 5 × 5, and 4 × 4 numbers of metallic patches per each periodicity can be mounted under one bowtie nanoantenna. The patch width (W) was then varied under each patch periodicity and the reflection phases along the frequency range were calculated.
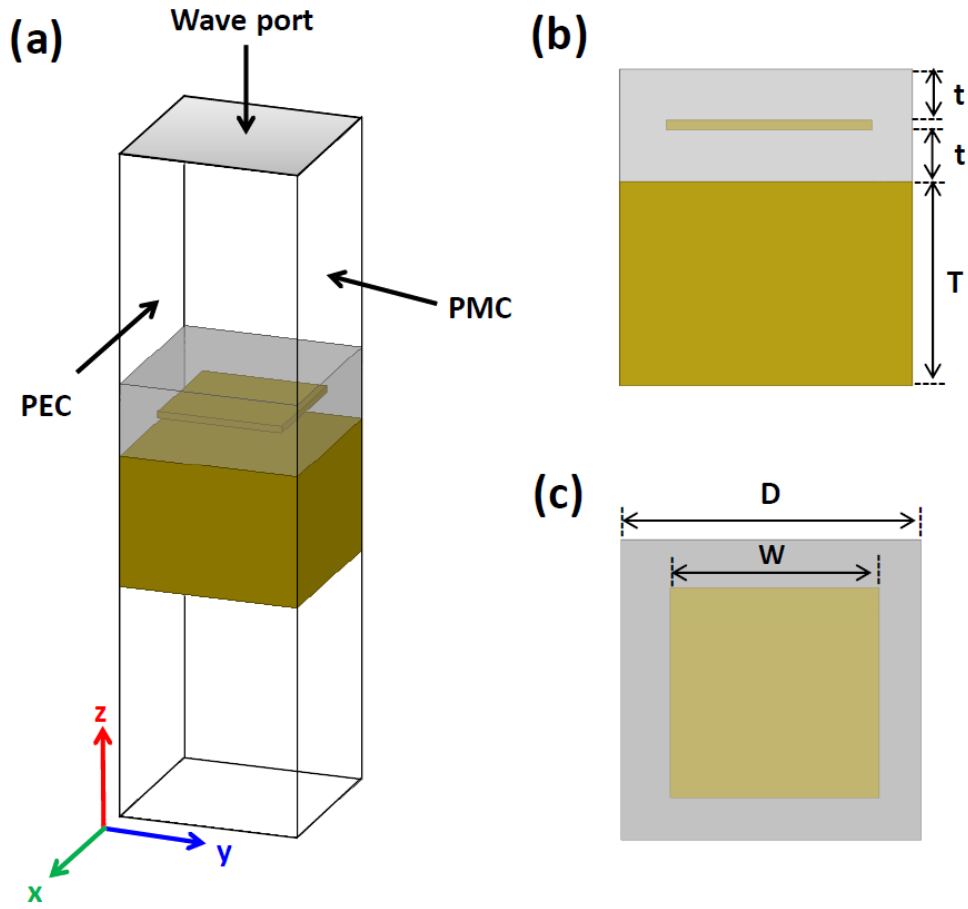
Figure 2.7. (a) Schematic view of the metallic patch unit cell simulation. (b) Side view (y-z plane) with given dimensions of t = 50 nm and T = 200 nm. (c) Top view (x-y plane) with the patch periodicity (D) and patch width (W).

Figure 2.8 shows the reflection phases of the patch arrays as a function of the patch width (W) and frequency with four different patch periodicity cases. Because of the fixed equivalent inductance via the fixed substrate thickness of the patch array, the capacitance change due to variation of the patch width resulted in a resonant frequency shift. In Figure 2.8, we observe that the given patch width variation corresponds to the reflection phase shift from -100° to +100° at around 230 THz. Based on this, we chose specific points in which the patch arrays function as HIS and RIS using 0° and 90° reflection phases, respectively. The blue and red dots in Figure 2.8 represent the points for RIS and HIS at 230 THz. A summary of the specific patch widths (W) and patch periodicities (D) for HIS and RIS is given in Table 1. In Table 1, per each periodicity (D), two different patch widths (W) for HIS and RIS are listed along with the corresponding reflection (S11) phase, surface resistance (R), and surface reactance (X). The patch widths of 77.5 nm, 95 nm, 125

nm, and 135 nm show purely resistive properties with a 0° reflection phase at 230 THz, whereas the patch widths of 45 nm, 60 nm, 85 nm, and 95 nm provide inductive reactances with a 90° reflection phase at 230 THz under the patch periodicities (D) of 100 nm, 125 nm, 200 nm, and 250 nm, respectively. The table shows that the smaller patch periodicity (D) provides higher surface resistance (R) of the patch arrays for HIS, but the reactance values for RIS are maintained near 400 ohms.
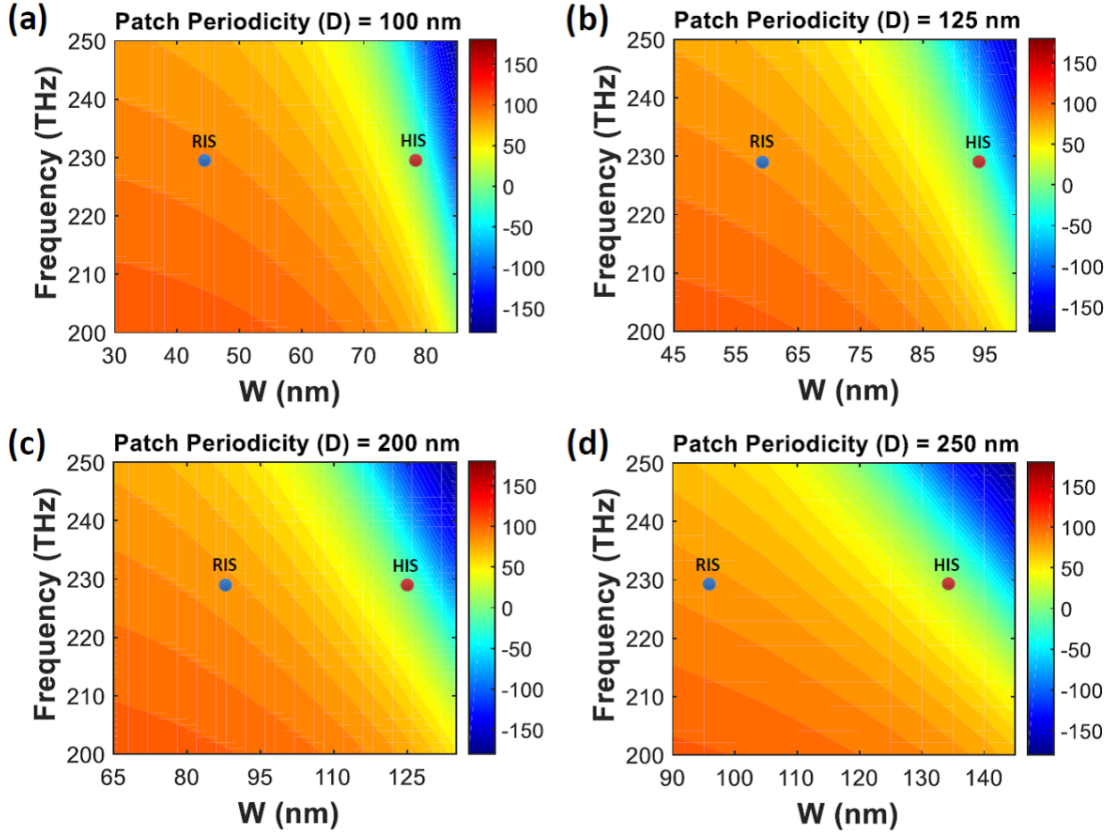
Figure 2.8. Reflection phases from the patch arrays with different patch widths (W) under the given patch periodicity (D) with (a) D = 100 nm, (b) D = 125 nm, (c) D = 200 nm, and (d) D = 250 nm.

Table 2.1. Summary of patch sizes and patch periodicities for the HIS and RIS at 230 THz.

D (nm)	W (nm)	S_{11} phase (º)	R (Ω)	X (Ω)	Note
100	77.5	0	6000	0	HIS
	45	90	4	383	RIS
125	95	0	5300	0	HIS
	60	90	5	405	RIS
200	125	0	4000	0	HIS
	85	90	6	427	RIS
250	135	0	3000	0	HIS
	95	90	6	421	RIS

2.5　AIS-Combined Bowtie Nanoantenna Array
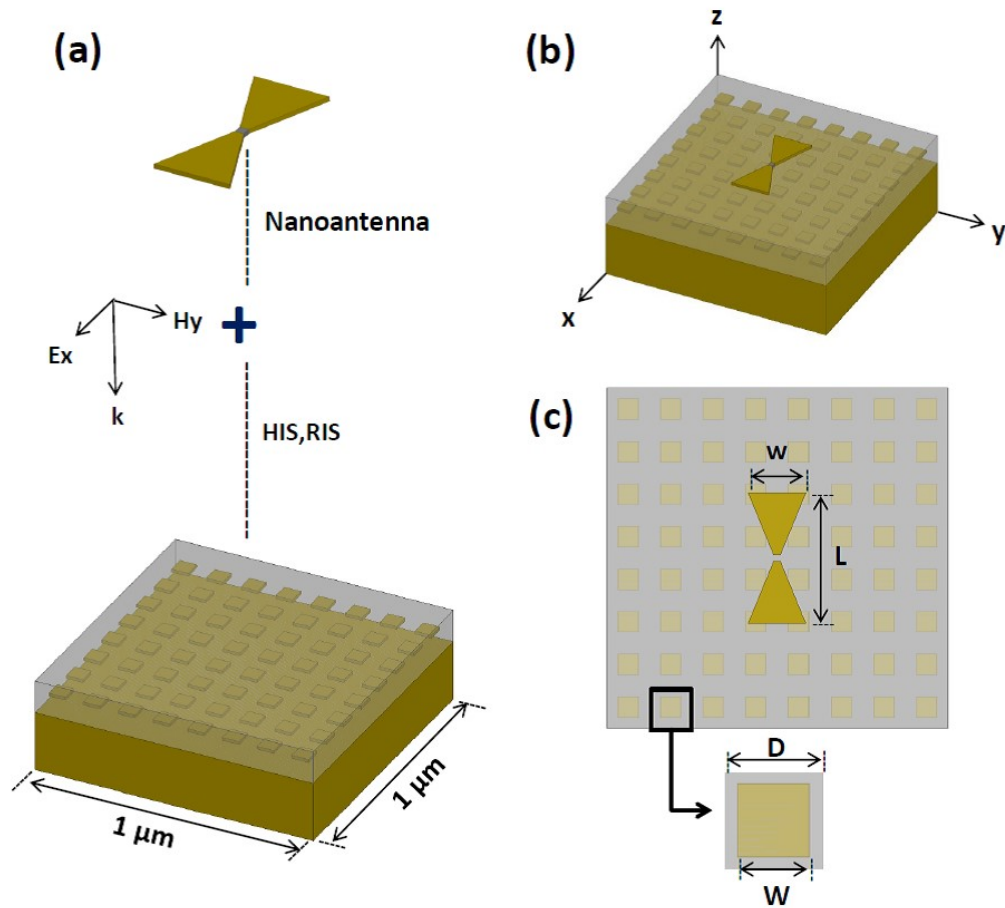
Figure 2.9. (a) Magnified view of the bowtie nanoantenna integrated with the metallic patch array. (b) 3D view of the integrated structure. (c) Top view of the combined structure.

Finally, the bowtie nanoantenna array was integrated with the patch arrays, which function as HIS or RIS and the field enhancement and the absorption rate were calculated in periodic boundary conditions. The nanoantenna structure was mounted on top of the patch array with a 50 nm-thick SiO_2 spacer and the overall area of the combined unit cell was set to 1 μm × 1 μm. Figure 2.9 shows a schematic view of the integrated structure using 8 × 8 patch array for RIS with a 60 nm patch width (W) and 125 nm periodicity (D) under a single bowtie nanoantenna. Here, the nanoantenna length (L) and width (w) were slightly adjusted to 370 nm and 140 nm from 375 nm and 145 nm to maintain resonance at 230 THz for the RIS-combined nanoantenna array cases.
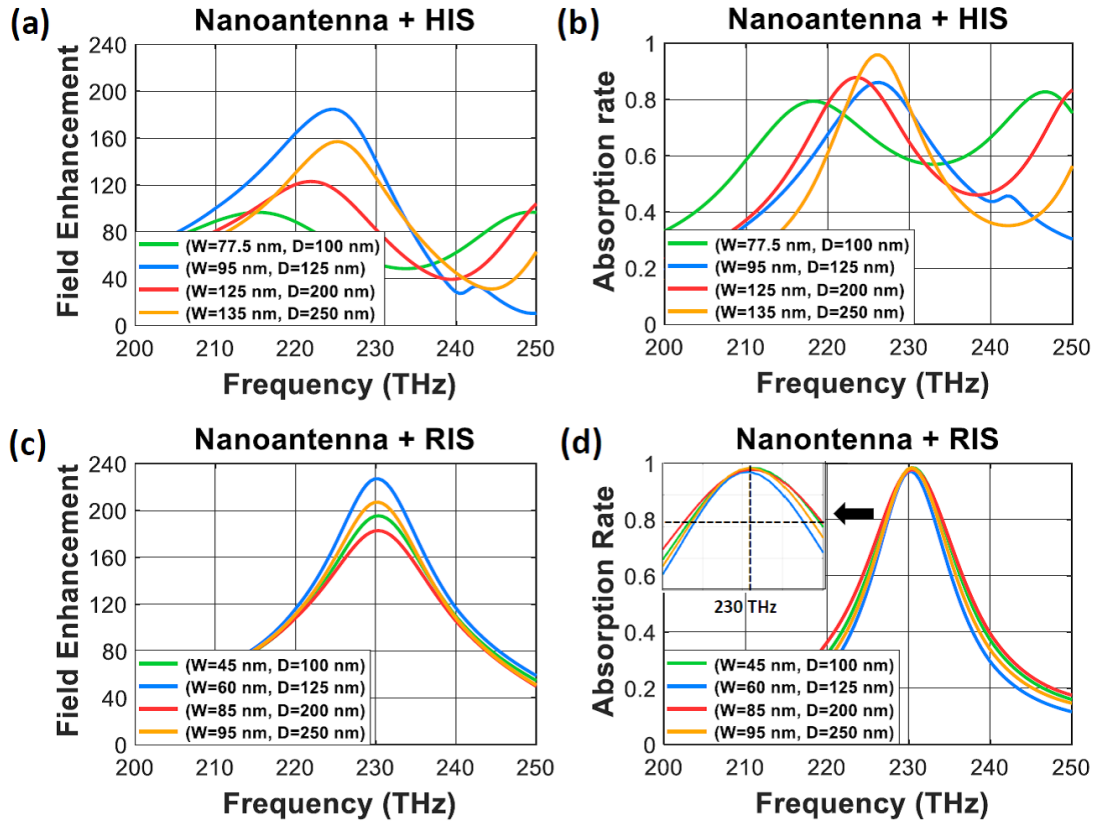
Figure 2.10. (a) Field enhancement and (b) absorption rate of the nanoantenna integrated with the HIS patch arrays. (c) Field enhancement and (d) absorption rate of the RIS-combined nanoantenna arrays.

The field enhancement and absorption rate of the bowtie nanoantenna array combined with the HIS and RIS patch arrays are presented in Figure 2.10. Overall, the nanoantennas combined with the RIS patches show higher field enhancements and absorption rates at 230 THz compared to the HIS-combined nanoantenna arrays. From

Figures 2.10(a) and 2.10(b), we find that the high surface resistance of the HIS patch arrays redshifts the resonant frequency of the nanoantenna and the maximum field enhancement values are limited at 185 near 225 THz. In detail, a HIS patch array with a smaller unit cell (W = 95 nm and D = 125 nm) supports a higher field enhancement value than that from the widest (W = 135 nm and D = 250 nm) patch. Because the HIS patch array with the shorter periodicity provides the higher surface resistance, we can understand that the nanoantenna array combined with the narrower HIS patch array provides higher field enhancement. In Figure 2.10(c), the RIS-combined nanoantennas exhibit superior field enhancement factors higher than 180 at 230 THz. Specifically, the 60 nm-wide RIS case has the highest electric field enhancement value of 228 at 230 THz, which is higher than the value of 223 of the bowtie nanoantenna with the grounded 80 nm-thick SiO_2. In addition, as shown in Figure 2.10(d), almost perfect absorption rates above 98% at 230 THz are achieved in all of the RIS cases; this value is also higher than the maximum absorption rate of 93% from the bowtie nanoantenna array with the grounded SiO_2. Note that all the RIS patch array cases maintain the resonant frequencies at 230 THz, in contrast to the HIS patch array cases.

We understand that the addition of the surface inductance from the RIS underneath the capacitive bowtie nanoantenna results in almost perfect absorption of the RIS-combined structures at 230 THz. To prove the mechanism quantitatively, we calculated the capacitance of the bowtie antenna using a parallel-plate capacitor with the same size as the antenna terminal in a full-wave simulation and we found that the value was 1.71 aF. This capacitance was found to be effectively canceled by the surface inductance of 0.28 pH (equivalent to the surface reactance of 405 Ω from the 60 nm-wide RIS patch array in Table 1) at 230 THz. Therefore, we conclude that the compensation via the inductive surface impedance of the RIS patch array realizes impedance matching between the bowtie antenna array and the vacuum for the perfect absorption at 230 THz. Figure 2.10(d) (inset) shows that the 60 nm-wide RIS patch case with the highest field enhancement at 230 THz exhibits the narrowest absorption bandwidth of 5.3% (based on the full width at half maximum) versus 6.82% from the 85 nm-wide RIS patch case with the lowest field enhancement.

2.6   Electric Fields Distribution Analysis

To understand the field distribution from the nanoantennas with the 95 nm and 135 nm-wide HIS patches, we calculated z-components of the electric fields (E_z) of both cases at 225 THz as shown in Figures 2.11(a) and 2.11(b). Figure 2.11(a) for the W = 95 nm case shows that strong fields are confined between the nanoantenna and the HIS patch array instead of the ground plane due to reflection from the HIS. We can understand that this reflection is a reason for the higher field enhancement and the lower absorption rate for the W = 95 nm case. However, Figure 2.11(b) for the 135 nm-wide HIS patch case shows that fields are distributed without significant discontinuity from the HIS and coupled to the ground similar to Figure 2.6(b) for the bowtie nanoantenna array with the grounded 80 nm-thick SiO_2. This means that the coupling happens mainly between the LSP and the array diffraction, leading to a higher absorption rate of 95%, as shown in Figure 2.10(b). However, the field enhancement is not increased compared to the antenna array with the 95 nm-wide HIS because the highly reflective nature from the 135 nm-wide HIS is not effective, as shown in Figure 2.11(b). Overall, we found that the bowtie nanoantenna array combined with the HIS patch arrays cannot guarantee perfect absorption and high field enhancement at the same time.
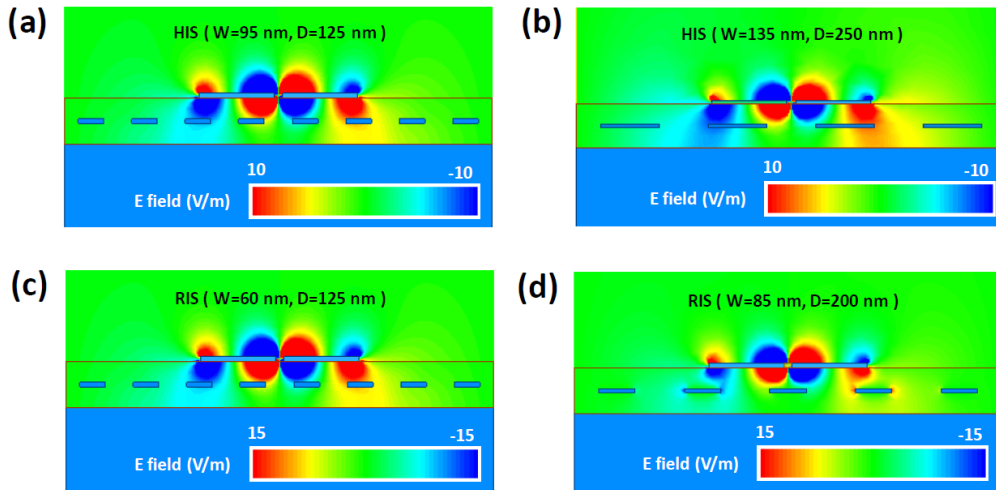
Figure 2.11. The electric field (E_z) distribution in the x−z plane of the bowtie nanoantenna combined with (a) a HIS patch (W = 95 nm , D = 125 nm) at 225 THz and (b) a HIS patch (W = 135 nm , D = 250 nm) at 225 THz. (c) a RIS patch (W = 60 nm , D = 125 nm) at 230 THz. (d) a RIS patch (W = 85 nm , D = 200 nm) at 230 THz.

25

To analyze the trade-off between the field enhancement and the bandwidth of the RIS-combined bowtie nanoantenna arrays, we calculated the E_z distribution of the 60 nm and 85 nm-wide RIS cases, as shown in Figure 2.11(c). In the bowtie nanoantenna with the 60 nm-wide RIS patch from Figure 2.11(c), a higher LSP magnitude is excited at the center of the nanoantenna and coupling between the LSP and the array diffraction is not perturbed despite the existence of the metallic patch array between the antenna and the reflector. A similar field distribution is shown in the 95 nm and 45 nm-wide RIS patch cases. However, in the 85 nm-wide RIS patch array case from Figure 2.11(d), the electric fields of the nanoantenna ends are coupled to the adjacent RIS patches; thus, high electric fields are also excited at the tips of the patches. Because one of the metallic patches is located below the nanoantenna gap, the distinctive coupling occurs and causes the lowest field enhancement in the antenna gap among the RIS cases. However, the energy confinement near the patch edges contributes to the high absorption rate of the integrated structure and realizes the widest absorption bandwidth from the 85 nm-wide RIS case.

2.7   Nanoantenna Fields Energy Density Analysis

To quantify the effects of a high field excitation near the edges of the RIS patch on the field enhancement and confinement in the nanoantenna gap, we calculated the effective mode volume (V_{eff}) [74], [99]. Because the high electric field near the metallic patches for the W = 85 nm case can hinder the field concentration in the nanoantenna gap, the V_{eff} calculation based on the energy density in the nanoantenna gap is a useful parameter for comparison. From the calculation given in the Methods section, the bowtie nanoantenna with the 60 nm-wide RIS patch array shows a V_{eff} of 6.03×10^{-4} μm^3, whereas the 85 nm-wide RIS case maintains a higher V_{eff} of 8.38×10^{-4} μm^3. This higher Veff from the 85 nm RIS case is correlated with the lower field enhancement at the terminal due to the excited fields near the metallic patches. Overall, the RIS-combined bowtie nanoantenna array achieved similar V_{eff} values compared to the triangle-shaped nanoantenna array [86]. Furthermore, V_{eff} can be related to the field enhancement magnitude based on the coupled-mode theory:

$$\frac{|E|^2}{|E_{inc}|^2} = A(\lambda_{res}) \frac{A_i \lambda_{res}}{\pi} \frac{Q_{abs}}{V_{eff}} \tag{2.9}$$

where $A(\lambda_{res})$ is the absorption rate of the nanoantenna at the resonant wavelength (λ_{res}), A_i is the spot size for incident waves with a normal direction, and Q_{abs} is the absorption quality factor. From this equation, we see that a higher Q factor and a smaller V_{eff} lead to a higher electric field enhancement. Thus, a lower V_{eff} of 6.03×10^{-4} μm^3 and a higher Q factor of 18.85 from the 60 nm-wide RIS patch case results in a higher field enhancement compared to the 85 nm-wide RIS case with V_{eff} of 8.38×10^{-4} μm^3 and Q_{abs} of 14.64. Furthermore, V_{eff} and Q_{abs} of the bowtie nanoantenna array on the grounded 80 nm-thick SiO_2 were calculated as 6.05×10^{-4} μm^3 and 22.54, respectively. From equation 2.8, it should be noted that the lower field enhancement from the nanoantenna array using the grounded 80 nm-thick SiO_2 compared to the 60 nm-wide RIS-combined nanoantenna array is due to the lower absorption rate, despite the similar V_{eff} and the higher Q_{abs} values.

2.8   Discussion on Fabrication Sensitivity Analysis
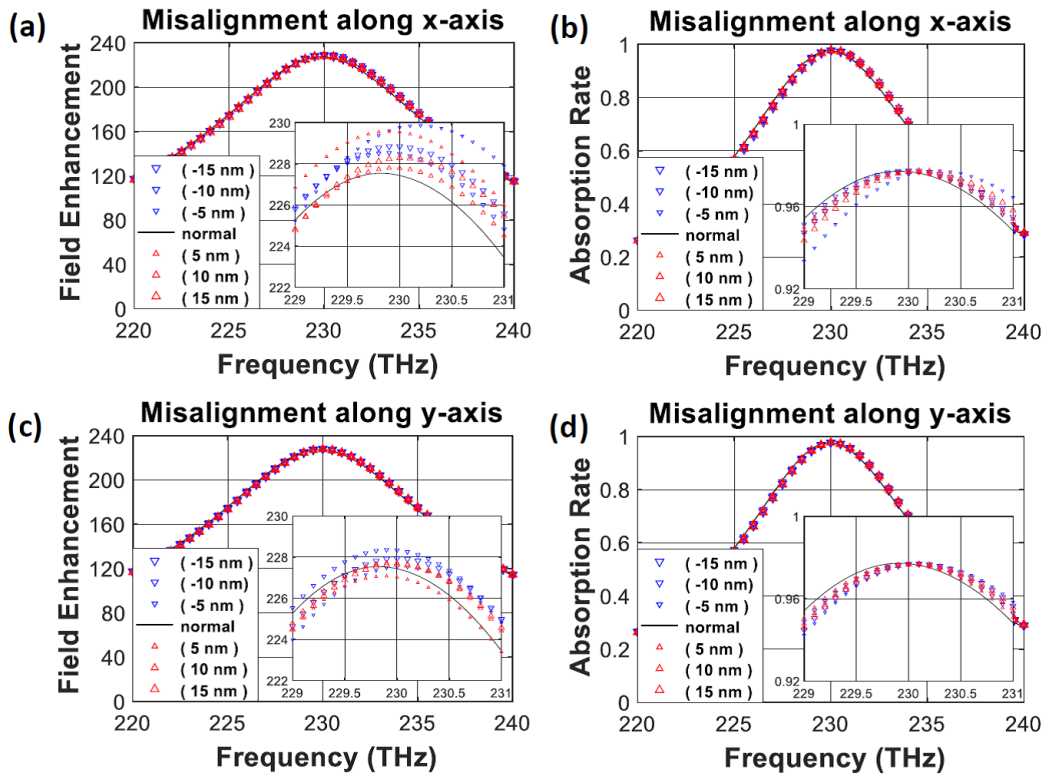
Figure 2.12. (a) Electric field enhancement and (b) absorption rate of the bowtie nanoantenna array combined with the 60 nm-wide RIS patch with the misalignment along the x-axis from the center of the patch array. (c) Electric field enhancement and (d) absorption rate of the structure with the exact misalignment along the y-axis.

The performance sensitivity of the RIS-combined bowtie nanoantenna array due to the possible fabrication uncertainty was investigated. Specifically, the misalignment between the nanoantenna and the patch array, and the property change of metal from surface roughness were considered because those changes may influence near-field coupling between multiple metallic layers of the proposed structure. First, we studied the effect of the geometrical misalignment on the field enhancement and the absorption rate by moving the bowtie nanoantenna along the x-axis and y-axis with -15 nm, -10 nm, -5 nm, 5 nm, 10 nm, and 15 nm from the center of the patch array. For simulations, we chose the bowtie nanoantenna array combined with the 60 nm-wide RIS patch. Figure 2.12 shows that ±15 nm misalignment results in field enhancement change less than 1% and stable absorption rates along with a merely 0.5 THz resonant frequency shift. In detail, Figures 2.12(a) and 2.12(c) indicate that field enhancement is relatively more sensitive to the misalignment along the x-axis instead of the y-axis because the nanoantenna is x-polarized. Figures 2.12(b) and 2.12(d) also show the absorption rate is less sensitive than the field enhancement because the misalignment does not perturb the surface impedance of the RIS patch array. Overall, we can conclude that the proposed structure maintains a minor change in the field enhancement and absorption rate due to the misalignment between the nanoantenna and metallic patch array.

The impact on the performance due to surface roughness of the metallic structures from fabrication was also studied. Recent papers showed that the metallic nanostructures fabricated by electron beam lithography (EBL) have surface roughness near 1 nm [102], [103]. Chen *et al.* modeled the fine roughness with 3D textures on the surface of gold nanoantennas and showed that the roughness does not change the optical property of the structures significantly in simulations [104]. On the other hand, Trugler *et al.* measured the complex permittivity of gold before and after the annealing process and showed that gold nanostructures modeled by the measured permittivity well predict the measurement result [103]. Thus, we applied the fabrication effect on metal in numerical simulations by using the complex permittivity of metal determined by a reported grain size after the annealing process. We selected a 40 nm grain size which corresponds to surface roughness of 1.7 nm after the annealing process and calculated a damping constant of gold using (2.9) [104], [105] :

$$\gamma_{\mathrm{g}} = \gamma_0 + \frac{1.37 V_F}{D} \frac{R}{1-R} \tag{2.9}$$

Here, γ_0 is a reference damping constant with infinite grain size and γg is the one that considers the grain size or surface roughness effect. $V_F = 1.35 \times 10^6$ m/s is the Fermi velocity of gold, D is the grain size, and R is the grain boundary reflection coefficient. From the calculation based on equation 2.9, $\gamma_g = 100.16 \times 10^{12}$ 1/s was obtained with D = 40 nm, R = 0.67, and $\gamma_0 = 6.28 \times 10_{12}$ 1/s [104]. Note that γg is 1.81 times larger than γ_{normal} (55×10^{12} 1/s) that was previously used for modeling gold in the bowtie nanoantenna and patch array. We converted the γ_g value to the complex permittivity via the Drude formula and applied that to all the metallic structures to consider the roughness effect. Here, the bowtie nanoantenna array on the grounded 80 nm-thick SiO_2 and the RIS-combined bowtie nanoantenna array (W = 60 nm and D = 125 nm) were simulated for comparison.
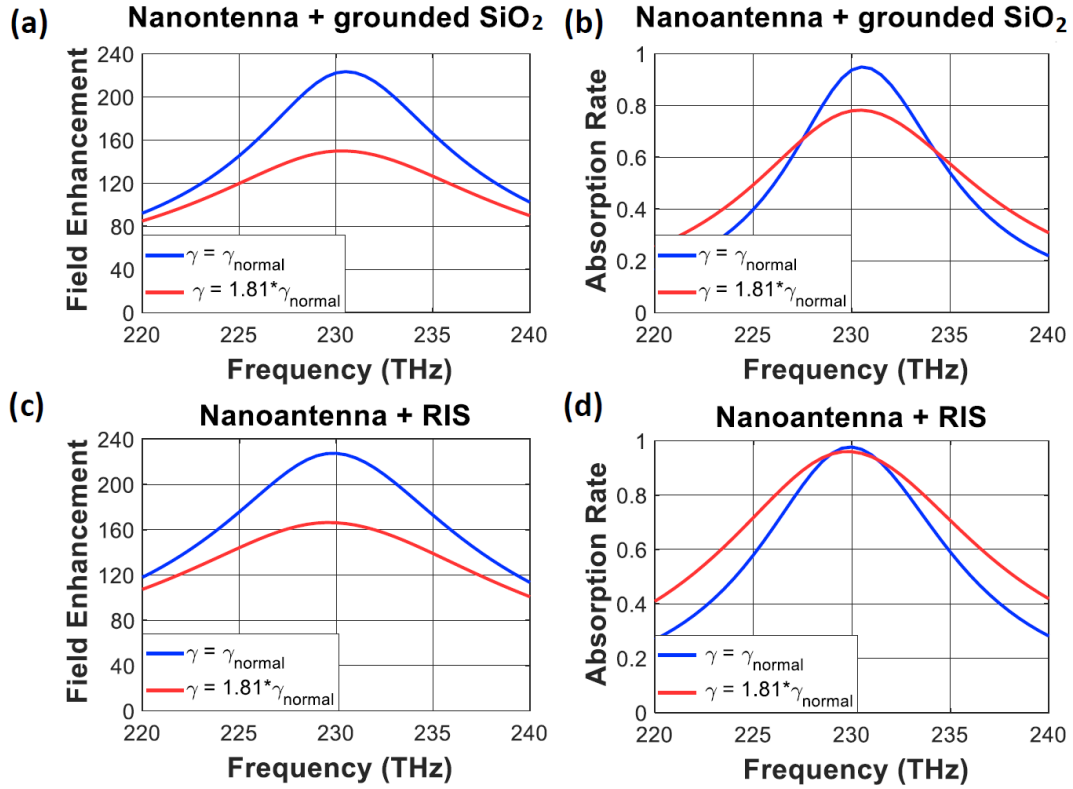
Figure 2.13. (a) Electric field enhancement and (b) absorption rate of the bowtie nanoantenna on SiO_2 grounded substrate with the different damping constants ($\gamma=\gamma_{normal}$ and $\gamma=\gamma_g=1.81 \times\gamma_{normal}$). (c) Electric field enhancement and (d) absorption rate of the bowtie nanoantenna combined with the 60 nm-wide RIS patch with the two different damping constants.

Figure 2.13 compares the electric field enhancement and the absorption rate from the aforementioned two structures modeled by gold without ($\gamma = \gamma_{normal}$) and with the surface roughness effect ($\gamma = \gamma_g = 1.81 \times \gamma_{normal}$). Overall, we observe that the field enhancement and the absorption are reduced with a broadened bandwidth and a slight redshift due to a higher metallic loss from the surface roughness. Among both, the bowtie nanoantenna combined with the RIS still maintains a high absorption rate of 95% and a field enhancement factor of 166 at 230 THz. These values are higher than 78% and 149 from the bowtie nanoantenna on the grounded SiO_2 spacer. Compared to the values from the case without considering the roughness effect, the RIS-combined structure shows 27% and 3% reduction in terms of the field enhancement and absorption rate; however, the counterpart suffers more with higher reduction rates, 33% and 16% for both parameters.

Table 2.2 State of the art electric field enhancement and absorption rate of the reported nanoantenna array structures.

Reference	Field enhancement (E/E_0)	Absorption rate (%)	Resonant wavelength (μm)	Nanoantenna structure in the array	Usage of lightning rod effect
Liu *et al.* 2008	80	80%	0.68	Elliptic dipole on a substrate	No
Seok *et al.* 2011	89	70%	0.88	Dipole nanoantenna on a grounded substrate	No
Zhou, *et al.* 2014	$2 \cdot 10^3$	-	0.75	Bowtie nanoantenna with a hybrid plasmonic array	Yes
Roxworthy, *et al.* 2014	160	-	0.7	Bowtie nanoantenna capped with a metallic slab	No
Eter, *et al.* 2014	$>10^3$	-	1.27	Bowtie nanoantenna with photonic crystals	Yes
Chen *et al.* 2014	126	60%	1.8	Bowtie nanoantenna with dielectric pillars	No
Lin *et al.* 2015	86	95%	1.03	Bowtie nanoantenna on a thin grounded substrate	Yes
Yong *et al.* 2016	109	98%	0.91	Circular nanodisk placed on a metallic film	No
Li *et al.* 2017	211	95%	0.9	Triangular nanodisk on a thin grounded substrate	Yes
This work	**228**	**98%**	**1.3**	**Bowtie shape + RIS**	**No**

From the simulation results, we can understand that increased metallic loss inside the patch array does not perturb its surface reactance significantly; thus, a high absorption rate from the RIS-combined nanoantenna array can be maintained. This high absorption, in turn, leads to the high field enhancement factor. From the simulation results, we conclude that the performance of the RIS-combined nanoantenna structure would be more robust than the conventional nanoantenna array even though the surface roughness effect is considered in both antenna and patch array. Performance comparison with the other reported nanoantennas is also provided in Table 2.2 and it can be found that the proposed structure shows the highest field enhancement factor among the cases with high absorption (> 90%). Note that our design achieves such a high field enhancement value without using a sharp tip for the lightning rod effect in the antenna gap that was used in the three cases with field enhancements higher than 200 in Table 2.2.

2.9   Conclusion

We showed that the nanoantenna array combined with the RIS patch array with an optimum surface reactance could simultaneously realize high electric field enhancement (> 200) and perfect absorption (> 98%) in the IR range. Our approach overcomes the fundamental limitation of the nanoantenna array designed on an ultra-thin dielectric spacer and a reflector. First, we designed a bowtie nanoantenna array with a conventional grounded substrate and proved that the structure could not achieve both conditions at the same time due to the trade-off between two parameters. It was also shown that the nanoantenna array with the HIS patch array could not realize high absorption due to its reflective nature. Finally, the bowtie nanoantenna array designed on an optimum patch array for RIS showed a field enhancement value of 228 and a near-perfect absorption rate of 98% at 230 THz. The structure outperforms the previously reported triangle-shaped patch array designed on an ultra-thin substrate [86]. Without using a grounded ultra-thin substrate that has been used in nanoantenna design, this work showed that a nanoantenna array combined with an optimum RIS achieved high field enhancement and perfect absorption at the same time. Additional numerical simulations showed that the performance of the RIS-combined nanoantenna array was less degraded from the surface roughness effect compared to the nanoantenna array with a conventional grounded dielectric spacer. We expect that the proposed RIS-combined bowtie nanoantenna array

with superior performance can be used to improve the efficiency of IR and optical detectors, plasmonic sensors, and IR energy harvesting devices.

Chapter 3

Circular Nanodisk Combined Reactive Impedance Surface (RIS) for Perfect Infrared (IR) Absorber

In this chapter, we proposed a perfect IR absorber by utilizing a circular nanodisk combined with a reactive impedance surface (RIS) to boost field enhancement. Unlike conventional metallic reflector, the RIS is a metallic patch array on a grounded dielectric substrate that can change its surface impedance. Without an ultra-thin spacer, the proposed structure maintains near-perfect absorption by impedance-matching with the vacuum. First, we designed a single circular nanodisk on a grounded SiO_2 substrate and selected a non-ultra-thin thickness for the SiO_2 and a disk diameter that produced maximum field enhancement at 230 THz. Second, a two-dimensional array using the optimum single circular nanodisk was designed, and the filling factor was optimized to maximize field enhancement. In simulations, the filling factor was tuned by tuning the distance between the antenna elements (array pitch). Third, we designed a metallic patch array as a RIS that can fit under the unit cell area of a single circular nanodisk set by the chosen array pitch. Finally, the absorption rate and the field enhancement are calculated and analyzed.

3.1 Introduction

The potential of infrared (IR) absorbers to achieve high efficiencies by controlling their shape and geometry has been the subject of intensive research [55]. Metal-insulator-metal (MIM) absorbers offer simple structures and the ability to realize high absorption using out-of-plane near-field coupling [70], [106]–[108]. In an MIM absorber, a periodic array of metallic structures comprising square or circular patches is patterned on a dielectric spacer grown on a bottom metallic reflector. For perfect absorption, the dielectric spacer should be ($\sim\lambda/100$) thinner than the resonant wavelength because a thin spacer gives rise to strong magnetic dipole resonance and allows for an effective loop current from the opposing currents on the patch and the reflector [49], [50], [85].

Oscillating charges due to localized surface plasmon polaritons (LSPPs) on the sides of the patch and the imaged charges on the reflector excite a pair of anti-parallel electric dipoles [109], [110]. The magnetic and electric energy stored by the dipole resonance modes and metallic loss effectively capture the incident power of the incoming wave, achieving perfect absorption [49], [50], [85]. Because the absorption behavior caused by confined LSPPs from the MIM absorber is sensitive to a surrounding medium change even at the nanometer scale, MIM absorbers have been considered for sensor applications, such as thermal IR sensors [111], [112], gas sensors [113], biosensors [114], localized surface plasmon resonance (LSPR) sensors [115], and surface-enhanced IR spectroscopy [66], [116], [117].

MIM absorbers with various metallic patch shapes using the ultra-thin spacer for perfect absorption have been reported [49], [50], [64], [85], [86], [118]. A gold nanostripe-based MIM with a dielectric spacer thickness of $\sim\lambda/530$ achieved a 90% absorption rate near a wavelength of 1.5 µm [118]. In a similar spectrum, near-perfect absorption of 95% was achieved using a 10 nm–thick grounded Al_2O_3 substrate with circular, square, and triangular patches [86]. However, MIM absorbers with ultra-thin spacers suffer from low field enhancement (< 100)[86], [118], which is defined as the ratio between the incident field intensity and the excited field near the structure (E/E_0), because opposing currents on the patch and the reflector that are too close cancel each other. One way to increase the field enhancement of an MIM absorber is by controlling the ratio between the metal patch area and the unit cell area (the filling factor) [86], [119], [120]. For that purpose, the filling factor is set to be lower than 10% to maintain a collective effect in a patch array [119], [120]. In [86], a circular disk array on a 10 nm–thick grounded Al_2O_3 spacer with a high filling factor of 19.6% resulted in a field enhancement of 75. A similar nanodisk array on a grounded SiO_2 spacer (23 nm– thick) with a lower filling factor of 2.18% achieved a higher field enhancement factor of 85 at a wavelength, 860 nm [119]. This implies that changing the filling factor from the MIM absorber for a given ultra-thin spacer cannot boost field enhancement significantly beyond 100 due to the aforementioned cancelation effect. For array cases using relatively thicker grounded spacers or those without a ground, controlling the filling factor can also increase the absorption rate or extinction ratio [80]–[82], [121]–[128]. Previous studies suggest that the maximum interaction occurs when in-phase coupling is maintained between scattered waves due to the array and LSPPs of each element [80], [82], [124]. Because the peak spectrum of LSPPs of each element in a MIM

absorber depends on spacer thickness, both the thickness and the filling factor should be considered to maximize absorption and field enhancement at a given wavelength.

In this chapter, we presented a new IR absorber structure that can overcome the limitation of low field enhancement in ultra-thin spacer-based MIM absorbers. The proposed structure maintains perfect absorption from impedance-matching with the surrounding medium by utilizing a reactive impedance surface (RIS). The RIS is a metallic patch array on a grounded dielectric substrate that can alter its surface impedance, unlike a common metallic reflector. Previously, the RIS has been used for an antenna ground plane to improve antenna performance at microwave frequencies by offsetting the near-field capacitive feature through engineered surface impedance [52], [129]. In this study, the metal structure on the top of the absorber uses a circular disk array, and the RIS compensates for the capacitive nature of the disk. To the best of our knowledge, this is the first attempt to use a RIS to improve the performance of a MIM-based IR absorber. Numerical simulations achieved an absorption efficiency of 98% and a high electric field enhancement factor of 180 at 230 THz (at a wavelength of 1.3 μm) using a circular nanodisk with a filling factor of 4.33% and without an ultra-thin dielectric spacer. The value of the electric field enhancement from this structure was much higher than the maximum enhancement value of near 85 associated with circular nanodisks with grounded ultra-thin spacers [86], [119], [120]. We further demonstrate a polarization-independent property of the proposed absorber by illuminating two different linearly polarized incident waves. The superior performance of the proposed IR absorber can be used to enhance the sensitivity of sensors, including LSPR sensors and surface-enhanced infrared spectroscopy.

3.2   Design of Circular Nanodisk on SiO$_2$ Substrate

In the MIM absorber based circular nanodisk design, the metallic elements and insulators were gold and silicon dioxide (SiO$_2$), respectively. For proper modeling in the near-IR region, frequency-dependent dielectric constant values for SiO$_2$ from previous experimental studies were used [92], [93]. All outer boundaries of the air box for the single nanodisk simulations were set by the radiation boundary. Meanwhile, an infinite array of circular nanodisks were realized by the periodic boundary condition (PBC) along the y–z and x–z planes and radiation boundaries at the top and bottom. The structure was then illuminated with an x–polarized incident plane wave in a normal direction (wave vector k

is along the negative z–axis). The absorption rate of the circular nanodisk array was calculated using the equation $A = 1 - (P_r/P_i) - (P_t/P_i)$, where P_r, P_t, and P_i are the reflected, transmitted, and incident power, respectively. The electric field enhancement factor was calculated at a hot spot 1 nm below the nanodisk edge [86], [130]. Field enhancement was defined as the ratio between the magnitudes of the electric fields at the measurement point and the incident electric field (E/E_0) [86], [120], [125], [131], [132].
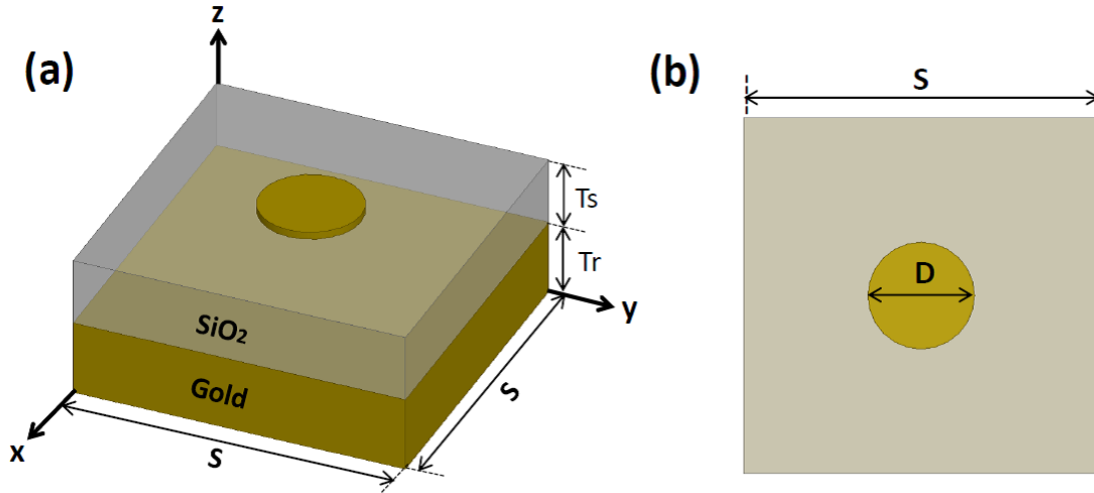
Figure 3.1 (a) Schematic view of the circular nanodisk mounted on the SiO_2 grounded (b) Top view (the x−y plane) with a circular nanodisk diameter (D) of 235 nm and a substrate size (S) of 1.3 µm.

Firstly, a single circular nanodisk was designed over a SiO_2 grounded substrate in the radiation boundary. A schematic view of the design is shown in Figure 3.1. The substrate size (S), thicknesses of the gold reflector (T_r) and disk were fixed at 1.3 µm, 200 nm, and 10 nm, respectively. An x-polarized plane wave ($E_0 = 1$ V/m) was illuminated normally from above the structure, the electric field (E) 1 nm below the edge of the nanodisk was calculated, and E/E_0 was used for a field enhancement factor [86], [130]. To accurately calculate the field enhancement factor, a 10 nm × 10 nm × 10 nm SiO_2 box enclosing the field calculation point was inserted and mesh sizes smaller than 1 nm were used. With this simulation setup, we found that 235 nm for the disk diameter (D) and 40 nm for the SiO_2 thickness (T_s) provided the maximum field enhancement at 230 THz. Figure 3.2(a) shows the electric field enhancement of the single nanodisk on the grounded SiO_2 substrate versus frequency. A maximum field enhancement of 159 occurred at 229 THz. We avoided tuning the structure at a nanometer level to realize the resonance at precisely 230 THz. Figure 3.2(b) displays the z component of electric field distribution

(Ez) in the x−z plane along the disk's central axis, indicating that the strong electric fields were confined to the interface between the edges of the nanodisk and the SiO_2 substrate. This electric field confinement was due to out-of-plane coupling between the nanodisk and the gold reflector [70], [86], [106].
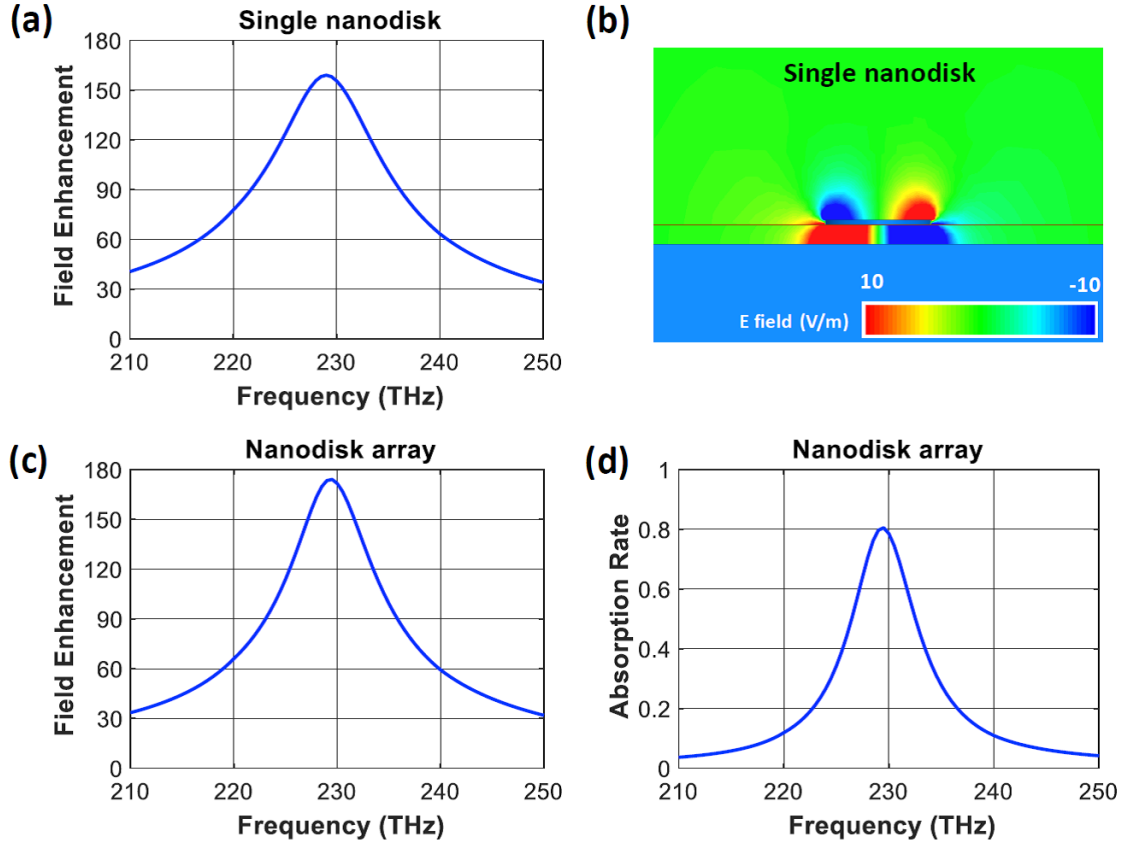
Figure 3.2 (a) The electric field enhancement of the single nanodisk with a disk diameter (D) of 235 nm and a SiO_2 thickness (T_s) of 40 nm (b) The z component of the electric field distribution (E_z) in the x−z plane (c) The electric field enhancement, and (d) the absorption rate of the nanodisk array with an antenna pitch size (P) of 1 μm.

Using the single nanodisk with maximum field enhancement at 229 THz, we designed its two-dimensional array with master and slave boundaries along the x−z and y−z planes of the simulation boundary. An antenna pitch size (P) of 1 μm produced peak field enhancement at 230 THz and this result can be attributed to in-phase coupling between the diffraction mode from the array and the LSPPs from the individual nanodisk. This pitch size with the given disk size is equivalent to a filling factor of 4.33% that follows trends from previous studies [81], [82], [119], [124]. The electric field

37

enhancement and absorption rate of the nanodisk array on the grounded 40 nm–thick SiO_2 substrate with an optimum pitch are presented in Figures 3.2(c) and 3.2(d). The nanodisk in the array structure exhibited resonance near 230 THz with a higher field enhancement factor of 174, compared with a value of 159 from the single nanodisk. The absorption rate of 81% at 230 THz is not perfect because the disk was designed to achieve high field enhancement and the magnetic resonance was not strong enough to realize impedance-matching with air.

3.3   Reactive Impedance Surface (RIS)
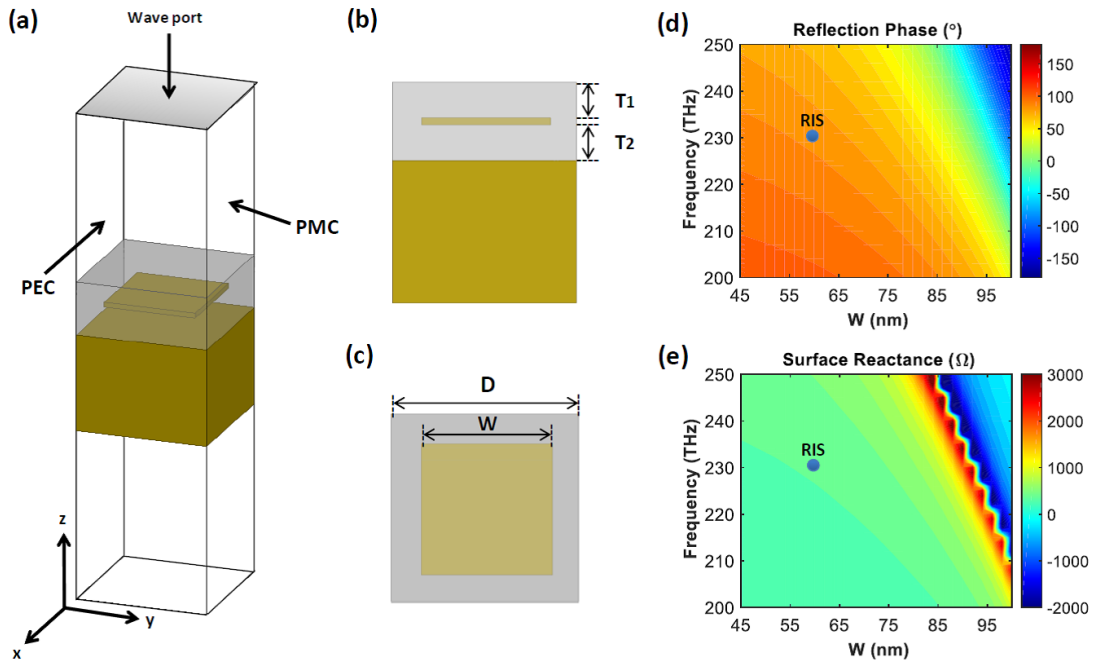
Figure 3.3 (a) Schematic view of the metallic patch unit cell with PEC and PMC boundary conditions and wave port excitation. (b) Side view (y−z plane) with dimensions of $T_1 = T_2 = 50$ nm. (c) Top view (x−y plane) with the patch periodicity (D) and patch width (W). (d) Reflection phase and (e) surface reactance of the RIS as a function of patch width (W) and frequency (D = 125 nm).

We designed a RIS that will be integrated with a nanodisk array to achieve perfect absorption and high electric field enhancement. The RIS consisted of a square patch array on a 50 nm–thick SiO_2 grounded substrate (T_2). A 50 nm–thick layer of SiO_2 was placed as a spacer (T_1) between the patch array and the top of the structure. The top surface of the

SiO$_2$ spacer was used as a reference plane to calculate the phase of the reflection coefficient, and the nanodisk array was then mounted on that. A schematic view and the detailed simulation setup are presented in Figures 3.3(a), 3.3(b), and 3.3(c). The RIS was designed to provide a 90° reflection phase at a resonant frequency of 230 THz because the surface reactance is dominant over surface resistance. First, we set the patch periodicity (D) at 125 nm to fit under the optimum pitch (1 μm) of the nanodisk array and tuned the patch width (W) to realize a 90° reflection phase. In the unit cell simulation for the RIS, an infinite array of metallic patches was modeled using a perfect electric conductor (PEC) and perfect magnetic conductor (PMC) boundary in the y−z and x−z planes of the simulation boundary, and a wave port was used to determine the magnitude and phase of the reflection coefficient of the patch. The surface reactance (Z_{surf}) of the RIS was then determined from the complex reflection coefficient (Γ) using the equation $Z_{surf} = [(1 + Γ)/(1 − Γ)] \times Z_0$, where Z_0 is the characteristic impedance of the vacuum.

Figures 3.3(d) and 3.3(e) depict the phase of reflection coefficient and surface reactance as a function of patch width (W) and frequency, with a fixed patch periodicity (D) of 125 nm. The phase of the reflection coefficient and surface reactance changed from −100° to +100° and −2000 Ω to 3000 Ω, respectively. We marked points that provided a 90° reflection phase at 230 THz with blue dots and found that a width of 60 nm meets the condition and the corresponding surface reactance was 405 Ω.

3.4 Performance Analysis of Circular Nanodisk Mounted on RIS

Finally, the nanodisk array was integrated with a metallic patch array that functioned as the RIS. The nanodisk was mounted atop the patch array with a 50 nm−thick SiO$_2$ spacer (T$_1$). The SiO$_2$ thickness between the patch array and gold reflector (T$_2$) was set to 50 nm. Figure 3.4 shows a schematic design view of the circular nanodisk unit cell combined with the RIS. The overall area of the combined unit cell was 1 μm × 1 μm and the nanodisk was mounted on 8 × 8 RIS patches with a 60 nm patch width (W) and 125 nm periodicity (D).
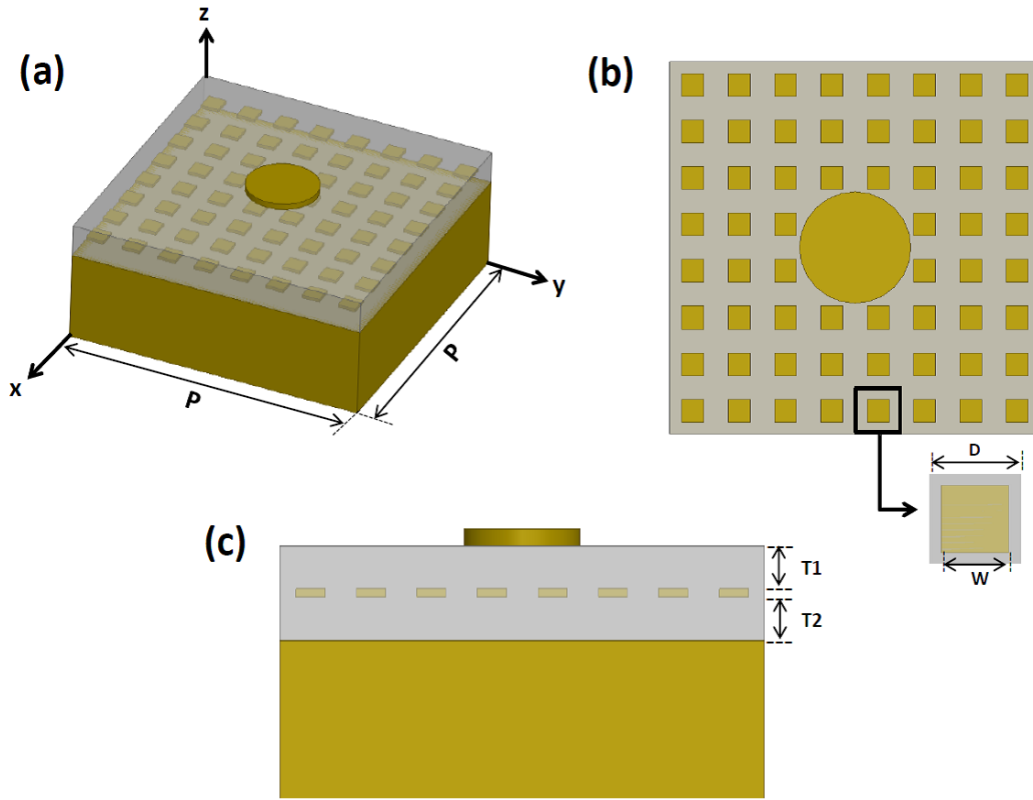
Figure 3.4. (a) Schematic view of the nanodisk mounted atop 8 × 8 RIS patches. (b) Top view (the x−y plane) of the structure (c) Side view (the y−z plane) with T1 = T2 = 50 nm for thicknesses of the SiO$_2$ spacers on top and bottom of the patch array.

The field enhancement and absorption rate of the nanodisk array combined with the 60 nm−wide RIS patch and a value of 50 nm for both T$_1$ and T$_2$ are shown in Figures 3.5(a) and 3.5(b) (red-color). We found that the addition of the RIS patch array under the nanodisk increased the resonant frequency to 239 THz, while the field enhancement and the absorption rate were 175 and 85%. The imperfect absorption at 239 THz can be attributed to the mismatch between the surface impedance of the structure and the characteristic impedance of the vacuum. We calculated the surface impedance of the integrated structure and found that surface impedance was 244–j175Ω at 239 THz, which has a lower resistance than the 377 Ω of the vacuum. We also concluded that the surface inductance from the RIS patch (T$_1$ = T$_2$ = 50 nm and W = 60 nm) did not cancel capacitance from the nanodisk at 230 THz. Then, we tuned the spacer thickness to find the optimum field enhancement and absorption rate at 230 THz. Figure 3.5(a) and 3.5(b)

confirm that as the spacer thickness reduces, the resonant frequency shifts to the lower due to high capacitance from the thinner spacer.
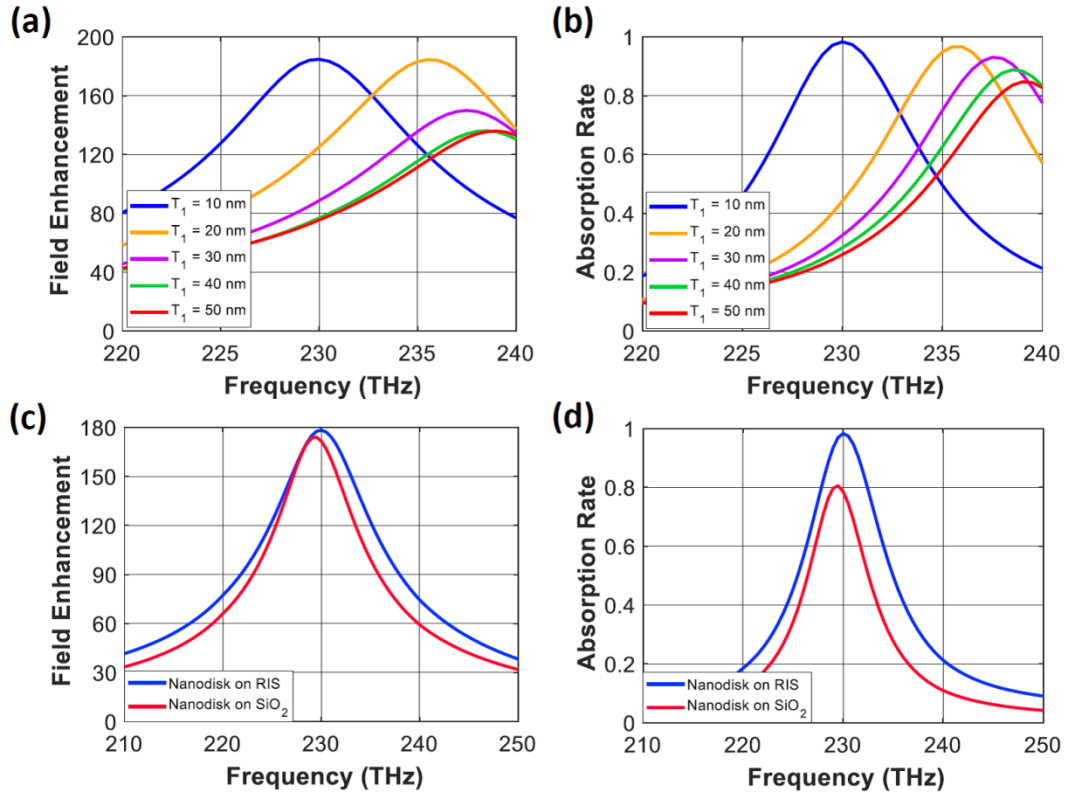
Figure 3.5. (a) Electric field enhancement and (b) absorption rate of the nanodisk arrays combined with the 60 nm−wide RIS patch array with a different spacer thickness (T_1). The performance comparison between the circular nanodisk on the RIS and the grounded SiO_2 substrate in terms of (c) electric field enhancement and (d) absorption rate.

Finally, a T_1 value of 10 nm provided resonance at 230 THz with a high field enhancement value of 180 and almost perfect absorption (98%) at 230 THz (blue-line), as shown in Figures 3.5(a) and 3.5(b). From the simulation, the integrated structure with T_1 of 10 nm produced a surface impedance of 377+j39 Ω at 230 THz, which shows a similar resistance with the characteristic impedance of the vacuum. We further calculated the surface reactance of the patch array for the 60 nm-wide RIS (T_1 = 10 nm and T_2 = 50 nm) and verified that the surface reactance value became 225 Ω, which is lower than 405 Ω from the RIS (T_1 = 50 nm and T_2 = 50 nm) at 230 THz. Because the reactance values from the RISs were calculated from the wave port, a disk sitting near a RIS would experience a different reactance. To estimate the effective inductance of the RIS which compensated the

capacitance of the disk, we calculated the capacitance of the disk using an equation (C_m =$c1\varepsilon d\varepsilon 0A/d$) for a parallel plate capacitor with a modification (adding c1) which reflects the LSPP effect [133]. The capacitance (C_m) of the circular disk (D = 235 nm) sitting on the ground with 70 nm-thick SiO_2 was 4.4 aF. Here, a fitting constant (c1) of 0.2 was used to consider non-uniformly distributed charges on the disk. Cm indicates capacitance from one edge of the disk, so the overall capacitance of the disk should be $2C_m$. On the other hand, the inductance from the disk itself was neglected because the level was near fH. The final 8.8 aF capacitance of the disk requires 54 fH inductance to maintain the resonance at 230 THz. Because 225 Ω at 230 THz from the optimum RIS is equivalent to 156 fH, we can estimate that about one-third of the inductance calculated from the wave port is effective in the RIS-combined structure. The calculated capacitance of the circular disk is also from approximation; thus, the effective inductance from the RIS can be varied. However, it is important to note that a significant portion of inductance from the RIS is needed to effectively cancel the capacitance of the disk and realize almost perfect absorption at 230 THz.

Figures 3.5(c) and 3.5(d) compare field enhancement and absorption rate values between the optimum RIS-integrated structure (T_1 = 10 nm and T_2 = 50 nm) and the nanodisk array on the grounded 40 nm-thick SiO_2 substrate. The peak values near 230 THz for both cases were 180 versus 174 in the field enhancement and 98% versus 81% in the absorption rate. This result means that only a RIS-integrated absorber can achieve near-perfect absorption along with high field enhancement (> 100), even with a thick SiO_2 spacer. We further calculated a field intensity ratio at the hotspot with and without the nanodisk in the RIS-combined absorber and found that the value is 140. Due to a slightly enhanced field intensity of 1.29 V/m in the absence of the disk, the ratio became lower than the field enhancement factor (180) but still higher than 100.

Furthermore, Figure 3.5(d) shows that the nanodisk array on the RIS had a wider absorption bandwidth compared with the nanodisk array on the grounded SiO_2 spacer due to an increased overall volume of SiO_2 that maintains high near-field coupling. The absorption bandwidths of the nanodisk array on the RIS and the grounded SiO_2 substrate were 4.13% and 3.47% (based on full width at half maximum), respectively. Finally, the final RIS-integrated MIM absorber outperformed the reported ultra-thin spacer-based circular nanodisk structures that exhibited the maximum field enhancement near 85 with an absorption rate of 95% [86], [119], [120], [125]–[127]. Additionally, the field

enhancement of 180 (E/E_0) from the proposed absorber can be converted to a surface-enhanced Raman scattering (SERS) factor which is used for IR spectroscopy applications. Because the SERS factor is proportional to $|E/E_0|^4$, the proposed absorber will show 16 times higher SERS factor compared to the other absorbers. Furthermore, the RIS-combined absorber can be used for a single molecule detection as its SERS enhancement of 10^9 is higher than the threshold levels, 10^7-10^8 [134], [135].
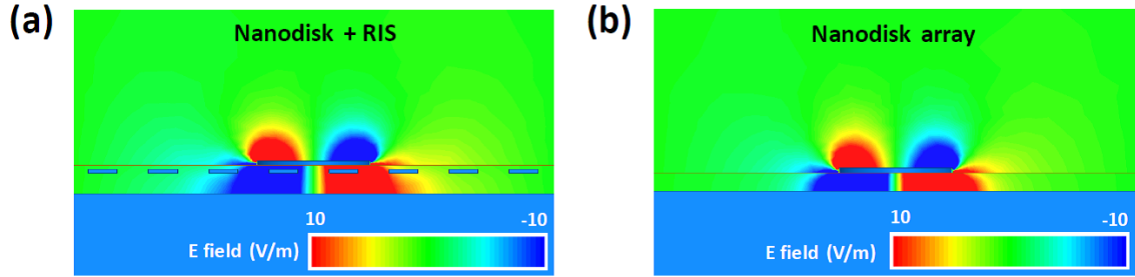
Figure 3.6 The z component of the electric field (E_z) in the x−z plane along the disk's central axis for (a) the nanodisk combined with the 60 nm−wide RIS patch and SiO_2 spacers and (b) the nanodisk array on the grounded SiO_2 substrate.

To understand the coupling mechanism between the nanodisk array and the RIS patch array, we calculated the z component of the electric field (E_z) in the x−z plane along the disk's central axis Figure 3.6(a) shows that the coupling between the LSPPs and the array diffraction was not disturbed due to the RIS patch array, and strong fields were maintained in a wider area between the disk and the reflector compared with the fields from the nanodisk array in Figure 3.6(b). From this analysis, we concluded that the higher field enhancement and absorption rate from the nanodisk array combined with the RIS patch could be attributed to the strong coupled field in a larger volume.

3.5   Polarization Independence of IR Absorber based on RIS

We further investigated the polarization sensitivity of the proposed IR absorber to demonstrate its polarization independence. Due to the circular shape of the nanodisk and the square shape of the metal patch array for the RIS, we expected the same optical response for x- and y-polarized incident waves. In numerical simulations, the circular disk array integrated with the RIS patch (W = 60 nm, T_1 = 10 nm, T_2 = 50 nm) was illuminated with a y-polarized incident plane wave additionally in a normal direction from the top.
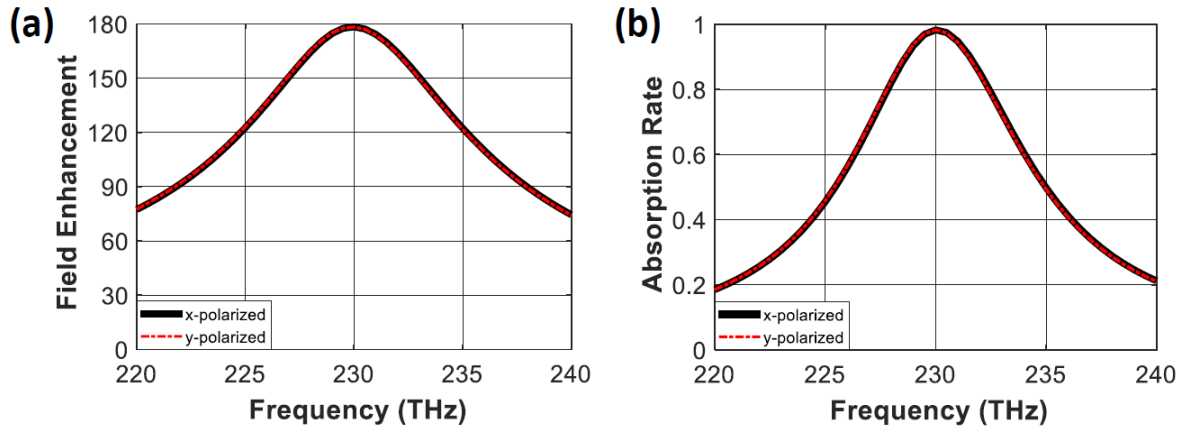
Figure 3.7 Demonstration of polarization independence of the proposed absorber. (a) Electric field enhancement and (b) absorption rate of the proposed absorber with different types of polarization.

Figure 3.7 shows the electric field enhancement and the absorption rate of the integrated absorber with x- and y-polarized incident plane waves in a normal direction. The exact overlaps of the parameters indicate the polarization independence of the proposed absorber, although the RIS patch was combined. The symmetrical arrangement of the RIS patch array beneath the circular nanodisk allowed for stable near-field coupling for both x- and y-polarized incident field cases. This polarization-independent feature from the RIS-integrated nanodisk absorber would therefore guarantee robust performance, even with unpolarized or any linearly polarized incident waves.

3.6 Discussion on Fabrication and Experiment of IR Absorber based on RIS-combined Nanodisk

Similar to other nanostructures, nanometer-scaled gold shapes (< 100 nm) for the disk and the RIS can be patterned using e-beam lithography (EBL) or focused ion beam (FIB) milling, and the SiO_2 layers between metallic structures can be deposited using atomic layer deposition (ALD) [136]–[140]. In the multi-layer RIS-combined nanodisk array, depositing gold inside SiO_2 layers and alignment between the disk and the RIS patch would be challenging tasks. We found a solution where gold patterning inside a SiO_2 layer, such as a buried nanoantenna, was realized by filling gold in an engraved SiO_2 substrate etched by reactive ion etching (RIE) [138]. Also, the alignment between metallic patterns in two layers was resolved with the EBL technique using alignment marks [59]. In

experiments, the absorption rate can be measured using Fourier Transform Infrared (FTIR) spectrometer along with a microscope [86]. Furthermore, the field enhancement can be measured using near-field scanning optical microscopy (SNOM) with scattering-type scanning methods [141].

3.7 Conclusion

In this chapter, we proposed a polarization-independent perfect IR absorber based on a circular nanodisk array combined with a RIS to achieve high electric field enhancement and perfect absorption. The proposed absorber, with a filling factor of 4.33%, produced an electric field enhancement value of 180 and a near-perfect absorption rate of 98% at 230 THz. These values were higher than the 174 and 81% associated with a circular nanodisk array on a grounded 40 nm–thick SiO_2 substrate with the same filling factor. The proposed MIM absorber also outperformed other reported ultra-thin spacer-based MIM absorbers for which the field enhancement saturates near 85. Furthermore, we demonstrated a polarization-independent property of the proposed absorber by illuminating x- and y-polarized incident waves. Due to the symmetrical arrangement of the circular disk and patches for the RIS, the proposed absorber was stable with the polarization change of the incident wave, confirming the merits of the proposed absorber. In applications, a RIS-integrated MIM absorber with a superior field enhancement can be used to enhance the sensitivity of sensors, such as LSPR sensors and surface-enhanced infrared spectroscopy.

Chapter 4

Single Metal Nanoantenna Combined Bimetal Nano-thermocouple

This chapter discussed a novel design of a bowtie nanoantenna coupled with a bimetal thermocouple operating at a wavelength of 10.6 µm. The antenna design aims to achieve a high-temperature difference (ΔT) between the antenna center and the relatively cold area. The bowtie nanoantenna was made with a single metal without a thermal conductivity gap at the antenna center to maintain a high temperature by lowering heat flows. Then, a bimetal nano-thermocouple with a high Seeback coefficient gap (ΔS) is connected at the center. An open-circuit voltage (V_{oc}) is generated due to the temperature difference (ΔT) between the antenna center and the end of the nano-thermocouple. In the design method, the antenna and nano-thermocouple were made from a material with low thermal conductivity and high ΔS to generate high ΔT and V_{oc}. The nanoantenna was designed on a quarter wavelength-thick SiO_2 backed by a metal reflector for efficient heating at the antenna center. The lateral size of the device was also tuned to launch in-phase coupling of standing waves at the antenna center. Numerical simulation using COMSOL multiphysics 5.0 was performed to calculate the current density and the temperature difference between the antenna center and the end of the nano-thermocouple.

4.1   Introduction

IR harvesting devices from low-temperature heat (< 400 °C) are attracting significant attention because waste energy from low-temperature heat sources accounts for 85% of the total waste heat energy in the world [1], [5], [142]. The IR harvester based on thermophotovoltaics is a promising device for exploiting wasted IR energy; however, the devices operate at higher temperatures (> 1000 °C) [143]–[145]. To overcome this issue, researchers have developed IR-DC conversion devices based on nanoantennas because of their capability to efficiently absorb incident IR radiation [40]–[42]. Generally, using a

zero-bias rectifier that consists of a dipole nanoantenna and an ultrafast metal-insulator-metal (MIM) diode is a common method for IR harvesting devices [59], [146]–[148]. The diode utilizes a few-nanometer-thick oxide sandwiched between metallic antenna arms for electron tunneling [59], [146]. Owing to electron tunneling, current flows through the thin oxide at an antenna gap [59]. However, this method suffers from low rectification efficiency owing to the high RC time constant and responsivity-resistance trade-off, that is, a higher responsivity results in a higher resistance [58].

Another promising device for IR energy harvesting is a thermoelectric nanoantenna, which consists of a nanoantenna and nano-thermocouple connected at the antenna center. The nanoantenna absorbs IR energy and heats the antenna center (the hot junction) from its higher current compared to the end of the nano-thermocouple (the cold junction). The thermocouple then converts the temperature difference (ΔT) between the hot and cold junctions into an open-circuit output voltage (V_{oc}) via the Seebeck effect [149]. In (4.1), V_{oc} is directly proportional to ΔT and a relative Seebeck coefficient gap (ΔS) between two different metals of the nano-thermocouple [149]–[151].

$$V_{oc} = \int_{T_1}^{T_2} (\Delta S) dT = \Delta S \times \Delta T \qquad (4.1)$$

Recently, a bimetal dipole nanoantenna made from titanium (Ti) and nickel (Ni) was studied for IR harvesting devices by maximizing the Joule heating [151]. However, owing to the difference in thermal conductivity of the metals, less heat can be maintained at the hot junction because the heat tends to flow toward the material with higher thermal conductivity [151]–[154]. As a solution to this issue, a single metal nanoantenna was used to avoid heat spread such that the high temperature at the hot junction could be maintained [155], [156]. Previous studies revealed that a palladium (Pd) dipole nanoantenna integrated with a single metal Pd nano-thermocouple achieved a ΔT of ~25 mK with a V_{oc} of 0.03 μV. Despite the single-metal antenna, V_{oc} is still limited owing to the low Seebeck effect realized by the width difference of the single-metal thermocouple. To further increase V_{oc}, Szakmany et al. combined a single-metal antenna with a bimetal nano-thermocouple (Ni-Pd) and improved V_{oc} to 0.4 μV [157]. The higher V_{oc} resulted from the higher Seebeck coefficient realized by the bimetal thermocouple.

Recently, V_{oc} was further improved by minimizing parasitic heat loss from the hot junction of the antenna into the substrate [153], [155], [157], [158]. For physical implementation, Szakmany et al. placed a dipole nanoantenna combined with a bimetal

nano-thermocouple over an oxide membrane and achieved V_{oc} of 0.25 μV, which is 2.5 times higher than the 0.1 μV from the antenna directly mounted on the substrate. A similar antenna that was suspended over an air-filled cavity generated a V_{oc} of 38 μV from a ΔT of ~4.22 K. The higher ΔT was attributed to the lower heat transfer from the air underneath the hot junction of the antenna [158]. However, the suspended nanoantennas on the oxide membrane and air cavity will have a complex fabrication process and shorter durability owing to the fragility of the devices, limiting their usage for high V_{oc} massive array devices.

In this chapter, for the first time, we designed a substrate-mounted thermoelectric nanoantenna by utilizing vertical and horizontal bouncing standing waves from a reflector and an open-ended substrate to maximize V_{oc} instead of using a membrane structure. First, we combined a high-gain bowtie-shaped antenna instead of a dipole-type antenna and a bimetal thermocouple to achieve a higher Seebeck effect. Second, we utilized a quarter-wave-thick silicon dioxide (SiO_2) substrate on a metal ground for in-phase coupling between the incident and reflected waves near the antenna. Third, we etched the SiO_2 substrate to realize open-ended boundaries and controlled the size to constructively couple the excited field and standing waves at the antenna center. In simulations, the optimum thermoelectric nanoantenna device showed a V_{oc} of 2.06 μV for ΔT of 76.33 mK. In addition, the fabricated device exhibited a V_{oc} of 2.03 μV, which is approximately five times larger than 0.4 μV of the state-of-the-art thermoelectric nanoantenna mounted on a Si substrate [157]. Furthermore, we verified for the first time a significant increase in V_{oc} in a thermoelectric device by utilizing in-phase coupling between the electric fields and standing waves at the hot junction via an open-ended substrate.

4.2   Thermoelectric Nanoantenna Design

We designed a thermoelectric nanoantenna to achieve a resonant wavelength of 10.6 μm (28.3 THz frequency), which is marked by a high current density at the antenna center. For the antenna structure, Ti with a low thermal conductivity of 21.9 W/(m·K) was selected for high thermal impedance. A schematic of the Ti-based nanoantenna integrated with the Ni-Ti-based bimetal thermocouple on a SiO_2 substrate is presented in Figure 4.1. A pair of Ni and Ti was used as a bimetal nano-thermocouple because of the high Seebeck coefficient difference of ~27 μV/K, and each metal branched out from the antenna center, which is the hot junction of the device. To avoid undesired current flow in the

48

thermocouple and maintain a low temperature at its endowing to the incident wave, we connected the nano-thermocouple perpendicular to the antenna axis along the y-axis. The geometrical parameters, including the antenna length, antenna width, bowtie angle, the antenna center size, and thermocouple width, are denoted as L, W, α, r, and d, respectively, as shown in Figure 4.1. The substrate size and nano-thermocouple length are represented by S and L_t, respectively. Meanwhile, the antenna center with dimensions of 70 nm $\times$ 70 nm and ends of the nano-thermocouple represent the hot and cold junctions, respectively.
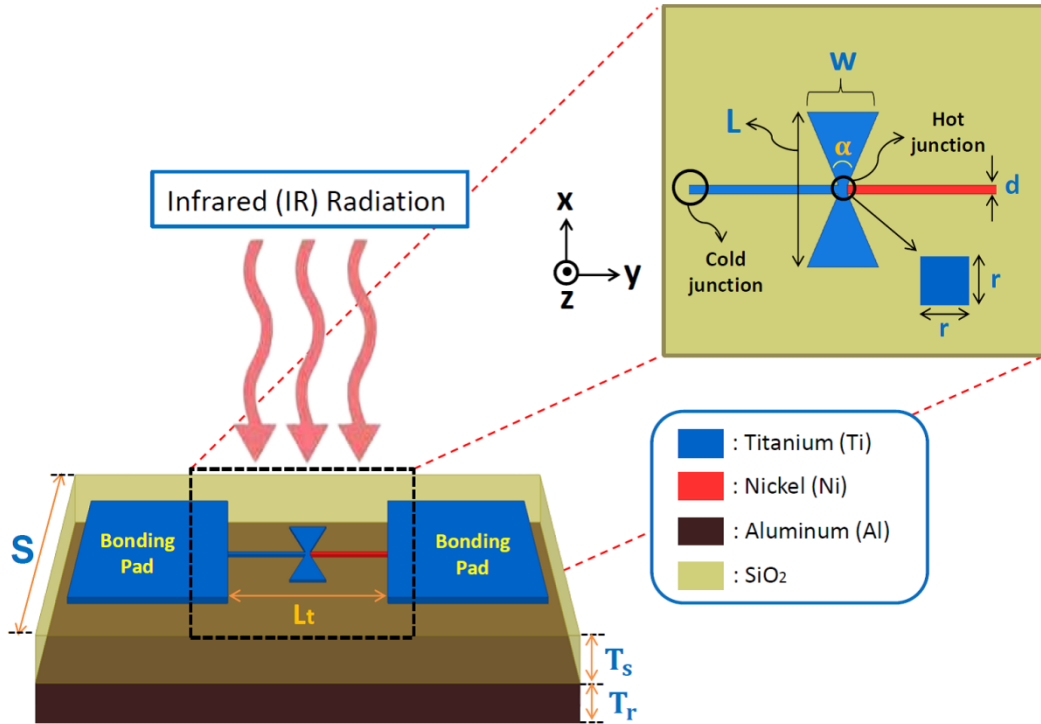
Figure 4.1 The schematic of the thermoelectric nanoantenna on an Al-grounded SiO_2 substrate. The geometric parameters are the substrate size (S), substrate thickness (Ts), nano-thermocouple length (L_t), and reflector thickness (T_r). The thermoelectric nanoantenna geometry consists of a bowtie nanoantenna and bimetal nano-thermocouple. L, W, α, r, and d are the antenna length, the antenna width, the bowtie angle, the antenna center size, and the nano-thermocouple width, respectively.

To maximize V_{oc} from the device at 28.3 THz, we directly placed the nanoantenna on a quarter-wavelength thick SiO_2 substrate backed with an aluminum (Al) reflector for in-phase coupling between the incident and reflected waves to increase the current density

at the antenna center. We then defined the area of the device by cutting the SiO_2 layer with open-ended boundaries to utilize horizontally bouncing standing waves along the x-axis. We fixed the SiO_2 and Al thicknesses (T_s and T_r) to 1.2 μm and 200 nm, which are a quarter-wavelength in SiO_2 medium and larger than the skin depth of ~4.8 nm of Al at 10.6 μm, respectively.

For the IR-to-heat transfer simulations, we utilized COMSOL Multiphysics and set the thermal properties of all materials, including mass density, thermal conductivity, and heat capacity, from a previous study [159]. In the heat transfer analysis, we used convective boundary conditions and set the heat transfer coefficient from the structure to air at 5 W/(m^2·K) [160]. In the full-wave electromagnetic analysis, we applied a perfectly matched layer (PML) to the simulation boundary to model the device sitting on an unbounded free space. The frequency-dependent dielectric constants and conductivities of all materials in the far-IR region have also been applied [161]–[163]. We set an x-polarized incident wave as the source of the IR wave, where the electric fields are parallel to the antenna axis with an intensity of 1.42 W/cm^2. The proper IR-to-heat transfer setup led to temperature distribution on the devices, and we fixed the temperatures at the antenna center and end of the thermocouple as Thot and Tcold for hot and cold junctions, respectively. Finally, we used the temperature difference, $\Delta T = T_{hot} - T_{cold}$ and calculated the output voltage using $V_{oc} = (S_{Ni} - S_{Ti}) \Delta T$, where S_{Ni} and S_{Ti} are the Seebeck coefficients of Ni and Ti, respectively [149].

4.3   Antenna Parameter Optimization via Standing Waves Interference

To determine the optimum dimensions for obtaining maximum V_{oc} at 28.3 THz, we simultaneously tuned the antenna length (L) and substrate size (S). In this optimization, we maintained a square shape of the SiO_2 substrate with S and optimized L_t later. Tuning L and S aims to determine the maximum current density at the antenna center and minimum at the end of the nano-thermocouple. The optimum S provides a high ΔT owing to the in-phase coupling between the electric field of the antenna and the standing waves from the open-ended SiO_2. Here, the thicknesses of the antenna and nano-thermocouple were kept constant at 60 nm. Simultaneously, the bowtie angle (α) and nano-thermocouple width (d) were set to 50° and 70 nm, respectively. ΔT at 28.3 THz as a function of L and S is presented in Figure 4.2(a), which shows that the optimum L for maximum ΔT at 28.3 THz is 1225 nm. In addition, among S values from 4 to 12 μm, 6 μm maintained the maximum

ΔT of 60.08 mK. The optimum L of 1225 nm and S of 6 μm indicate that the current density is maximum at the antenna center and minimum at the end of the nano-thermocouple. However, for fabrication, an S of 6 μm was not large enough to provide a sufficient distance from the antenna arms to the substrate edge. Therefore, we considered a larger S for fabrication to guarantee the stability of the fabricated devices. Owing to this fabrication issue, we calculated ΔT by increasing S from 15 to 55 μm and with a fixed L of 1225 nm.
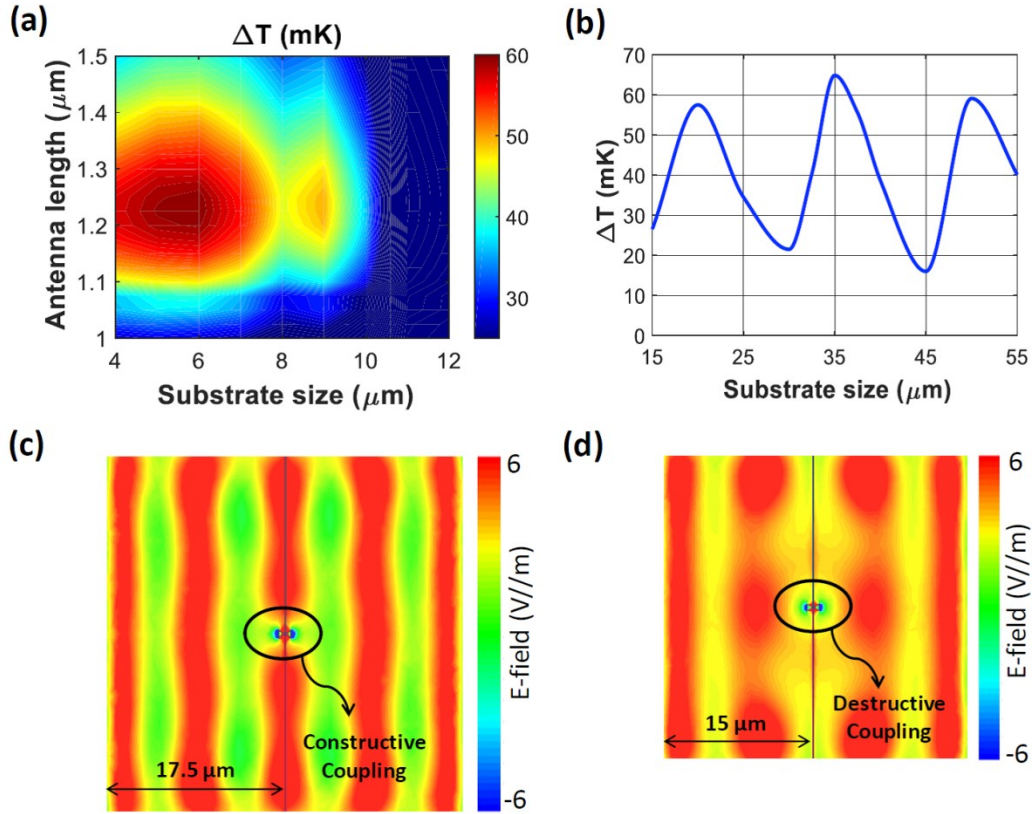
Figure 4.2 (a) Contour plot of ΔT at 28.3 THz as a function of substrate size (S) and antenna length (L). The values of S vary from 4 to 12 μm. (b) ΔT at 28.3 THz with varying S values and a fixed L of 1225 nm. Cross-sectional view of the Ex distribution at 28.3 THz on the x-y plane in the middle of the antenna along the z-axis for (c) S = 35 μm and (d) S = 30 μm.

Figure 4.2(b) shows ΔT at 28.3 THz as a function of S, ranging from 15 to 55 μm, clearly indicating several temperature peaks with the given variation of S. The substrate sizes for the minimum and maximum peaks (S_{min} and S_{max}) follow the Equations (4.2) and (4.3) if the effective wavelength (λ_{eff}) = 7.5 μm which will be found from the x-component of the

electric field (E_x) distribution inside the substrate from full-wave simulations. $S_{parasitic}$ represents the extra length to support a desired mode for the minimum and maximum fields at the antenna center due to parasitic effect from the nanoantenna and the open-ended substrate. We set values of $S_{parasitic}$ for S_{min} and S_{max} to 7.5 μm and 5 μm, respectively, to fit the temperature trend in Figure 4.2(b).

$$S_{min} = n \times \lambda_{eff} + S_{parasitic} \text{ (7.5 μm) if n = an odd number} \qquad (4.2)$$

$$S_{max} = n \times \lambda_{eff} + S_{parasitic} \text{ (5 μm) if n = an even number} \qquad (4.3)$$

Here, n corresponds to a mode number of TM_{n0} mode excited in the substrate and the E_x can be represented by Equation (4.4).

$$E_x = E_0 \cos\left(\frac{\pi}{S}x\right) \qquad (4.4)$$

When n = 4, Equation (3) provides S_{max} = 35 μm that corresponds to a maximum ΔT of 64.89 mK shown in Figure 4.2(b). To understand temperature-dependence from a TM mode excited in the antenna, we calculated the E_x on the x-y plane and in the middle of the antenna along the z-axis from S = 35 μm and S = 30 μm, as shown in Figure 2(c) and 2(d). From peak-to-peak distances of E_x from both Figures, we confirm that λ_{eff} is 7.5 μm inside the SiO_2 substrate. Figure 4.2(c) shows the maximum E_x magnitude at the center for an S of 35 μm; this trend corresponds to the maximum peak of the standing waves at the center from TM_{40} mode. This high E_x boosts the current density at the antenna center; thus, a higher ΔT of 64.89 mK is achieved. Conversely, a low electric field at the center from an S of 30 μm is shown in Figure 4.2(d) due to the minimum E_x at the center from TM_{30}. As a result, S of 30 μm has a lower ΔT of 21.52 mK compared with the 35 μm case.

4.4 Thermoelectric Nanoantenna Analysis

In this section, the discussion regarding the thermo-electric nanoantenna analysis includes the electric fields and temperature distribution along with the structure are presented. This analysis aims to understand the coupling behavior between electric fields from the antenna and the standing waves generated by a finite size from the open-ended SiO_2 substrate. Then, we calculated the antenna input impedance to find out the resonant nature of the proposed thermoelectric nanoantenna.

4.4.1 Coupling Behavior of Thermoelectric Nanoantenna

(a)

(b)

(c)

(d)
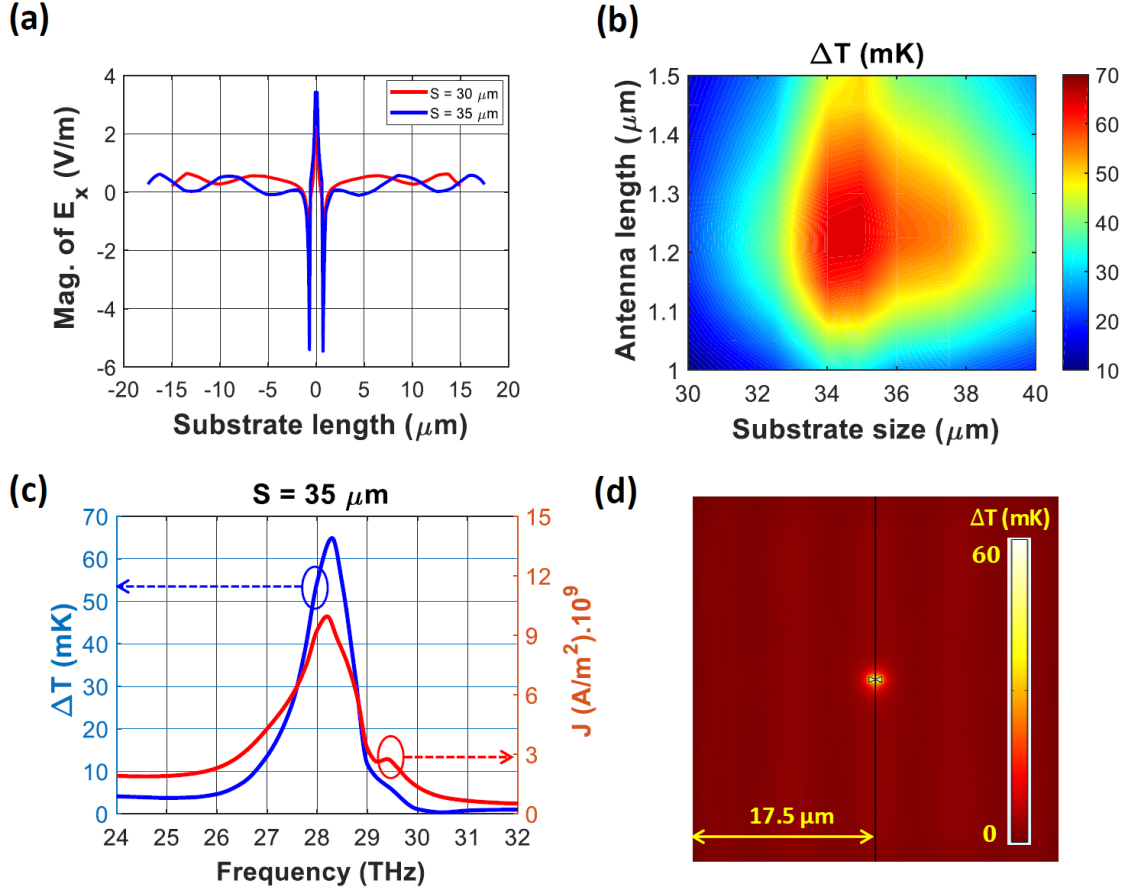
Figure 4.3 (a) Magnitude of E_x in the middle of the antenna along z-axis. (b) Contour plot of ΔT at 28.3 THz as a function of S and L. S varies from 30 to 40 μm. (c) ΔT and current density at the antenna center of the proposed thermoelectric nanoantenna as a function of frequency where L and S are 1225 nm and 35 μm, respectively. (d) Cross-sectional view of the temperature distribution at 28.3 THz along the same x-y plane.

To quantitatively understand the coupling between standing waves and antenna's electric field, we calculated the magnitude of E_x in the middle of antenna along the z-axis, as shown in Figure 4.3(a). One thing to note is that the E_x at the center is high for both S of 30 μm and 35 μm due to the electric field from the antenna coupled to standing waves from the substrate. Specifically, S of 35 μm provides higher E_x at the center due to the magnitude of standing waves is maximum as previously shown in Figure 4.2(c). Finally,

we chose S = 35 μm for the optimum dimension because this S is also adequately large that provides a sufficient distance between the antenna arms and substrate edge for stable fabrication. To confirm that L = 1225 nm maintains the maximum ΔT with an increased S of 35 μm, we further calculated ΔT by simultaneously varying L from 1 to 1.5 μm and S from 30 to 40 μm, as shown in Figure 4.3(b). The plot confirms that L = 1225 nm and S = 35 μm maintained a peak ΔT of 64.89 mK. Figure 4.3(c) presents the frequency response of ΔT (blue line) from the optimum dimensions (L = 1225 nm and S = 35 μm) and proves the highest ΔT of 64.89 mK at the operating frequency of 28.3 THz. Also, the current density at the antenna center along with the frequency for the same L and S confirms the maximum current density of 9.95×10^9 A/m^2 at 28.3 THz (red line). The highest current density corresponds to the highest temperature at the antenna center at 28.3 THz. Figure 4.3(d) shows the temperature distribution for L = 1225 nm and S = 35 μm at 28.3 THz on the x-y plane in the middle of the antenna, clearly indicating the highest temperature at the antenna center with a distinct difference compared with the end of the nano-thermocouple when S = 35 μm.

4.4.2 Input Impedance Analysis
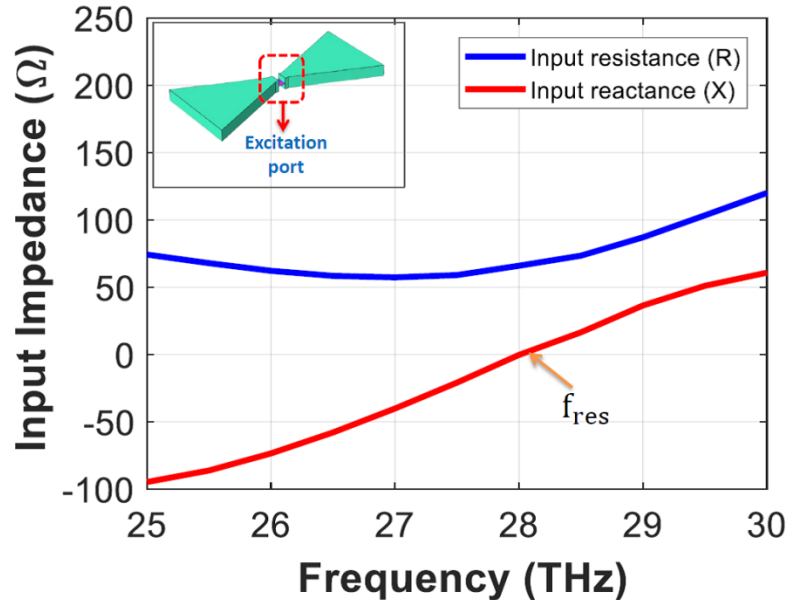
Figure 4.4 Input impedance of the Ti-based nanoantenna. The input resistance and reactance are represented by a blue line and red line, respectively. Inset shows the antenna structure in the simulation, where the two metallic arms are connected using a lumped port for calculating the input impedance.

To understand the nature of the resonance mode of the optimum thermoelectric antenna with L = 1225 nm, we calculated the antenna input impedance using a voltage gap source excitation in the perfectly matched layer (PML) boundary [71], [151], [164]. In this calculation, the two antenna arms were excited using a lumped port, as shown in the inset of Figure 4.4. The calculated input impedance of the antenna in Figure 4.4 indicates series resonance with an input resistance of ~65 Ω at 28.1 THz. The series resonant frequency from the input impedance is slightly lower than the desired frequency of 28.3 THz due to a small capacitance between the two arms of the antenna. This simulation result confirms that the nanoantenna operates at a series resonance near 28.3 THz, resulting in the highest current at the antenna center owing to its low resistance. Correspondingly, a high temperature occurs at the antenna center because of the Joule heating effect inside the metal [165], [166].

4.5   Nano-thermocouple Length Optimization
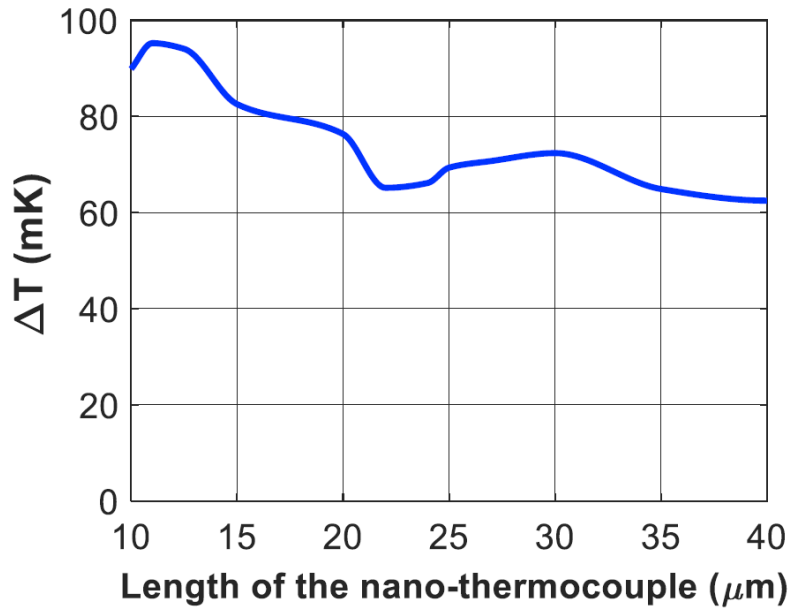
Figure 4.5 Temperature difference at the antenna center as a function of the nano-thermocouple length (L_t).

On top of the optimum nanoantenn and substrate, we further find the optimum dimension of the connection line to the bond pads which are needed for electrical contact with the measurement instrument. Here, bonding pads were connected to the ends of the thermocouple; the length of the thermocouple (L_t) thus determines the length of the

connection line and is parameterized to find the maximum ΔT at the antenna center. We thus investigated the Lt-dependence on ΔT and further tuned Lt under the optimum values of L and S. Figure 4.5 presents ΔT for varying Lt values from 10 to 40 µm and confirms that a 11 µm-long thermocouple provides the highest ΔT of 95.24 mK. In this case, the confined field at the antenna center effectively heated the hot junction of the thermocouple. The lower ΔT values from the other longer nano-thermocouples originate from the higher temperature at the cold junction owing to the excited field along the thermocouple. Despite the highest ΔT from the 11 µm-long nano-thermocouple, we chose a 20 µm length to consider a misalignment margin from UV lithography. In the simulation, the antenna combined with the 20 µm-long nano-thermocouple shows a ΔT of 76.33 mK, which is equivalent to a V_{oc} of 2.06 µV.

4.6   Conclusion

This chapter proposed an IR harvesting devices based on a single nanoantenna combined with a bimetal nano-thermocouple. The antenna was designed to achieve high current density and temperature difference (ΔT) at 28.3 THz (10.6 µm in wavelength). In the design, a bowtie nanoantenna made from a single metal, titanium (Ti), was chosen to efficiently capture the IR radiation and generate high current density at the antenna center. The single metal antenna guarantees high temperature at the antenna center by reducing heat flow due to the absence of a thermal conductivity gap. Then, a pair of nickel (Ni) and titanium (Ti) was connected to the antenna center, which functions as a nano-thermocouple to convert the temperature difference (ΔT) into an output voltage (V_{oc}). The antenna structure was then mounted on a quarter wavelength-thick of SiO_2 grounded substrate to generate in-phase coupling between the incident and reflected waves. The antenna parameters were optimized based on the coupling between the antenna's electric field and standing waves from the open-ended substrate and in-phase coupling between the incident and reflected wave. Firstly, we optimized the antenna size and found that the maximum ΔT of 76.33 mK (equal to V_{oc} of 2.06 µV) at 28.3 THz was achieved when L, S, and L_t are 1225 nm, 35 µm, and 20 µm, respectively. This high ΔT corresponds to series resonance from the antenna input impedance calculation that enables currents to flow from the first to the second arm and maximum at the antenna center.

Chapter 5

Thermoelectric Nanoantenna Fabrication and Measurement Setups

This work aims to experimentally demonstrate an IR energy harvesting device by utilizing a thermo-electric nanoantenna consisting of a bowtie nanoantenna coupled Bimetal nano-thermocouple. Therefore, this chapter discusses the detailed experimental methods covering the nanoantenna fabrication using a nano-fabrication technique such as electron beam lithography (EBL), electron beam evaporation, UV lithography, and thin film deposition. Also, the detailed nanoantenna measurement setup for both electrical and infrared (IR) measurement is presented. Note that the optimum nanoantenna parameter such as antenna length (L) and substrate size (S) used in the fabrication is taken from the simulation results discussed in chapter 4.

5.1 Thermoelectric Nanoantenna Fabrication

The fabrication of the proposed thermoelectric nanoantenna was performed at the UNIST Nano Fabrication Center. Several fabrication processes are required for a completed device, such as thin-film deposition, spin coating, electron beam lithography (EBL), thin film evaporation, UV lithography, dry etching, etc. This section will discuss the fabrication process for the bowtie nanoantenna, nano-thermocouple, and bonding pad in detail.

5.1.1 *Buffered Oxide Etch* (BOE) Removal

The proposed thermoelectric nanoantenna is fabricated over the single side polished p-type (525 ± 25) μm-thick silicon (Si) wafer with a resistivity of ($1\sim30$) Ω.Cm. The typical silicon wafer contains ~2 Å thicknesses of native silicon dioxide (SiO$_2$) that thermally grows over the Si wafer surface during the deposition of the Si layer. This native oxide layer increases the surface roughness of the Si wafer, thus, affecting the quality of a

deposited thin-film over the Si wafer. Therefore, *buffered oxide etch* (BOE) is the first process needed to remove the native oxide over the Si surface using *buffered hydrofluoric acid* (HF) and *de-ionized* water. The BOE process stops at the Si layer and does not continue further since this etching method is susceptible. In our experiment, the BOE process is based on the following chemical reaction:

$$SiO_2 + 6HF \rightarrow H_2SiF_6 + 2H_2O$$
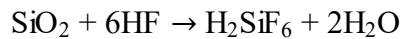
H2SiF6 is dissolved in water, the reaction was performed in an HF liquid, and ammonium fluoride (NH4F) as a buffering agent was added to maintain the concentration of HF and control the acidity (pH). The chemical buffering reaction is described as follows:

$$NH4F \leftrightarrow NH3 + HF$$
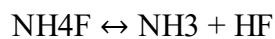
When the SiO_2 layer was completely etched, the Si wafer was transferred to the first de-ionized rinse water using polytetrafluorosthylene (PTFE) beaker tools, and the sample was kept for 5 minutes. Then, the sample was moved to the second de-ionized rinse water and rinsed for 5 minutes. Lastly, the sample was removed from the PTFE beaker and dried with an N2 gun.

5.1.2 Metal and Dielectric Deposition

Since the structure is placed on SiO_2 grounded substrate, the detailed fabrication process will be further explained in this section. First, 200 nm thickness of aluminium (Al) as a metallic ground plane is deposited over the Si wafer using 10 nm thickness of Titanium (Ti) as an adhesion layer. The Ti material was chosen due to its properties, such as high reactivity, and can respond chemically with Si wafer and Al overlayer. In the experiment, the Temescal FC-2000 e-beam evaporation system was used, and the detailed parameter during the evaporation process is described in Table 5.1.

Secondly, the 1.2 μm-thickness of the SiO_2 layer was deposited over the 200 nm Al ground plane using the plasma-enhanced chemical vapor deposition (PECVD) method. The PECVD method was chosen because of the high quality of the deposited thin film, uniform thickness, good resistance from cracking, and good adhesion of the thin-film to the substrate. In our fabrication process, the SiO_2 layer was formed by combining silicon precursor gasses such as silane (SiH_4), nitrous oxide (N_2O), and nitrogen (N2). The Sorona PEH-600 PECVD system was used for the deposition process, and the recipe during the

process is presented in Table 5.2. The overall device after Al and SiO_2 deposition can be seen in Figure 5.1.

Table 5.1 The detailed recipe used in the 200 nm-thick Al ground plane deposition using electron beam evaporation systems.

Process name (unit)	Step 1	Step 2	Step 3
Base pressure (Torr)	3×10^{-6}	-	-
Dome rotation speed (rpm)	20	-	-
Soak 1 rise time (sec)	50	-	-
Soak 1 power (%)	13	-	-
Soak 1 time (sec)	30	-	-
Soak 2 rise time (sec)	-	20	-
Soak 2 power (%)	-	15	-
Soak 2 time (sec)	-	50	-
Deposition rate (Å /sec)	-	-	1
Thickness setpoint (kÅ)	-	-	0.05
Rate ramp time (sec)	-	-	10

Table 5.2 The detailed recipe used in the deposition of 1.2 μm thick-SiO_2 process using plasma-enhanced chemical vapor deposition (PECVD) method.

Step name	Heat delay	Gas flow	Process	Pumping
Time (sec)	300	60	645	120
Pressure (Torr)	-	1	-	0
Temperature	350	-	-	-
RF power (300 W)	-	-	100	0
CF_4 (500sccm)	-	-	-	-
SiH_4 (500sccm)	-	262	-	0
NH_3 (50sccm)	-	-	-	-
N2O (2000 sccm)	-	700	-	0
N_2 (1000sccm)	100	0	-	-
O_2 (500sccm)	-	0	-	-
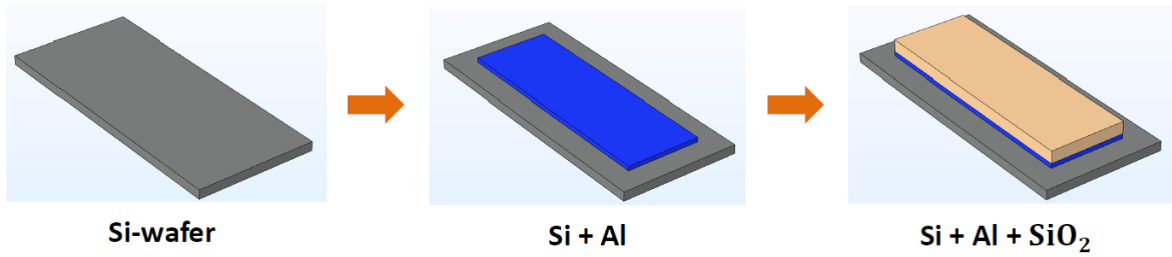
Figure 5.1. The overall devices after Al and SiO$_2$ deposition using e-beam evaporator and PECVD, respectively.

5.1.3 Fabrication of Bowtie Nanoantenna and Nano-thermocouple
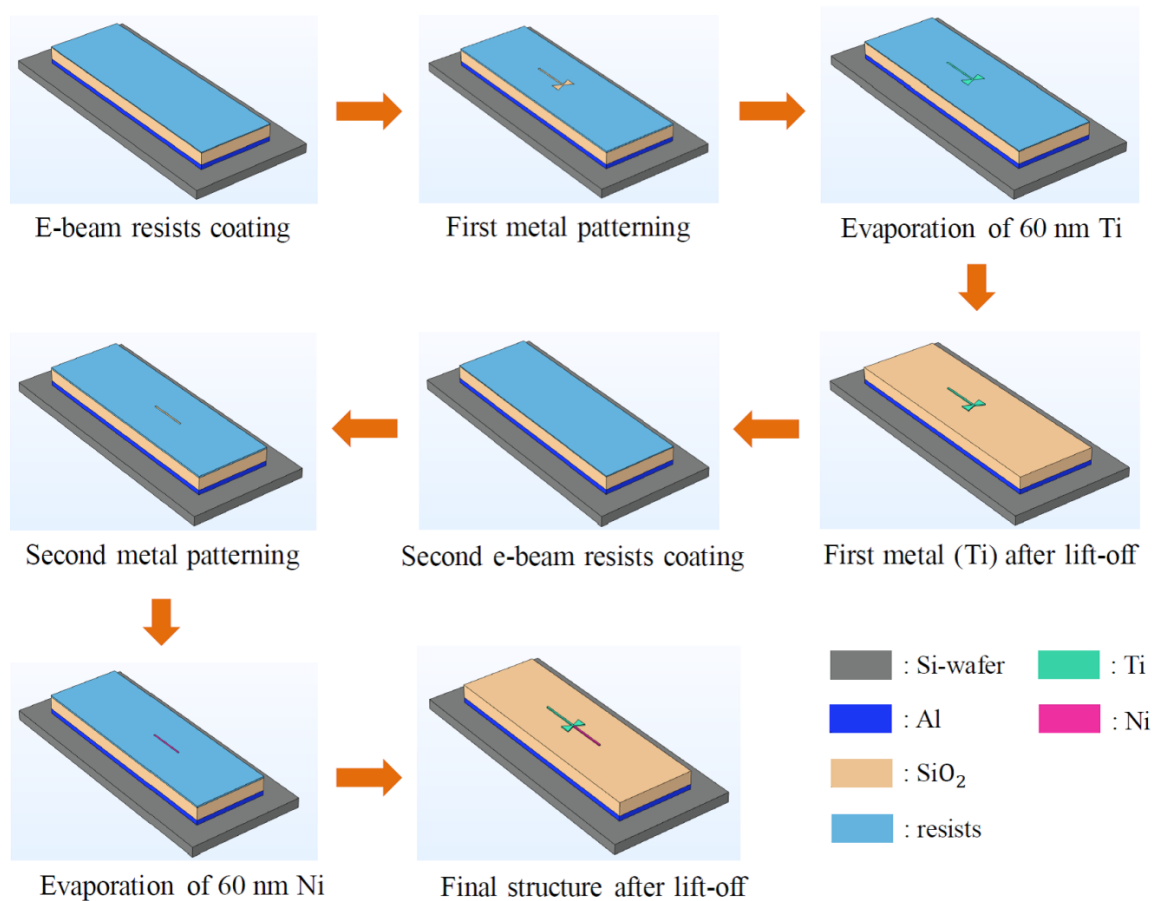
Figure 5.2. The detailed fabrication step of the bowtie nanoantenna combined nano-thermocouple using e-beam lithography (EBL) and e-beam evaporator.

The bowtie nanoantenna and nano-thermocouple are placed directly over the SiO$_2$ grounded substrate. The fabrication was done using electron beam lithography (EBL) for shape patterning and electron beam evaporation for metallization. The fabrication requires a two step EBL process since the structure is made from two metals: nickel (Ni) and

titanium (Ti). Due to misalignment from the e-beam machine that cannot be avoided, we deliberately make an overlapping area between the antenna center and nano-thermocouple to guarantee the good connectivity. The detailed fabrication step can be seen in Figure 5.2.

In the fabrication process, firstly, the AR-P 6200.9 e-beam resists were deposited into the sample using a spin coating technique. A rotation speed of 4000 rpm for 1 minute was applied to achieve 100 nm thickness. The sample was then baked for 3 minutes at 150°C baking temperature. Second, the patterning of bowtie shape nanoantenna and nano-thermocouple was done using the NB3 EBL system with a current of 0.7 nA and 4 C/m^2 doses. Then, the shape was developed using AR 600-546 e-beam resists developer for 1 minute, cleaning with isopropyl alcohol (IPA) fluid, and drying with an N2 gun. Then, the Ti metalization with 60 nm thickness was done using the Temescal FC-2000 e-beam evaporator system. Finally, the lift-off process using AR-P 6200.9 remover was performed for 5 hours to remove the e-beam resists. Checking using an optical microscope is needed to ensure that the e-beam resists are perfectly removed from the surface. The second patterning and maturation process for Ni also uses the same process. However, a 5 nm Ti adhesion layer is used during the 60 nm Ni metallization sing e-beam evaporator.

5.1.4 Fabrication of Bonding Pad

To investigate the antenna performance, a bonding pad is needed to electrically connect the device to the measurement probe for both electrical and infrared (IR) measurements. The bonding pad was patterned using the UV lithography and metalized with an e-beam evaporator in this work. The detailed fabrication step is illustrated in Figure 5.3. Firstly, the sample was coated with HMDS + AZ5214E photoresists (PR) using spin coating with a speed of 4000 rpm for 30 seconds to achieve a 1.5 μm photoresist thickness. The sample was then baked using a hot plate with 110°C temperature for 90 seconds. We utilized a negative photoresist type to avoid undesired contact between the bonding pad and isolation line. Then, the bonding pad patterning was done with a soda-lime photomask using the MDA400S UV lithography system. The sample was exposed by a UV lamp with an energy of 40 MJ/Cm^2, and baking the exposed sample at 125°C within 90 seconds. To generate a negative type of the patterned shape, the second UV exposure was performed without a photomask with an exposure energy of 130 MJ/Cm^2. The shape was then developed for 2 minutes on a beaker using a DPD-200 photoresists developer, and the shaking technique was used for perfect shape development. Next, the metallization

of 400 nm thickness of Ti is done using the Temescal FC-2000 e-beam evaporator system. Finally, the lift-off process was performed in $(CH3)_2CO$ solvent for 6 hours, and flushing technique to perfectly remove photoresists from the surface
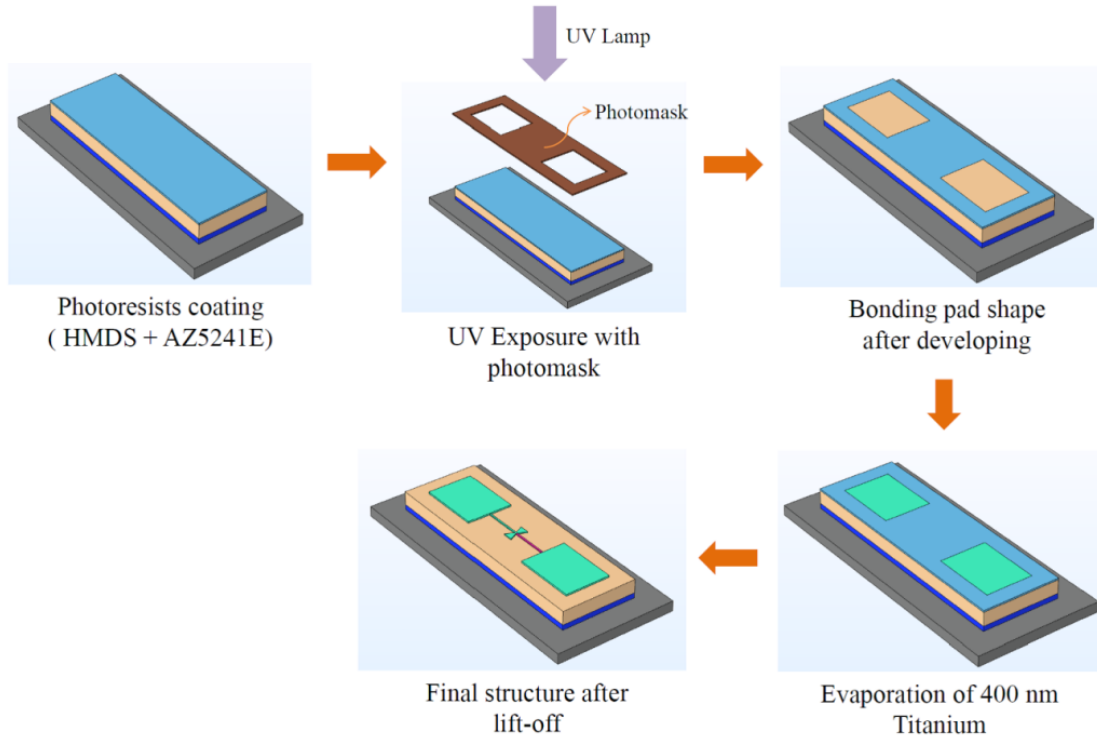
Figure 5.3 The detailed fabrication step of the bonding pad using a UV lithography system and e-beam evaporator.

5.1.5 Dry Etching

In the fabrication process, we fabricated several thermoelectric nanoantennas in the SiO_2 grounded substrate; thus, an isolation area is needed to provide good electrical insulation between the devices. To realize that, we performed dry etching, and the process was done by exposing reactive ion gasses to the isolation line pattern. In this work, the isolation line was patterned using UV lithography with a soda-lime photomask. Our device requires two dry etching steps, i.e., dielectric etching and metal etching to remove 1.2 μm-thick of SiO_2 substrate and 200 nm Al ground plane, respectively. The detailed dry etching process for the isolation line is presented in Figure 5.4.

Table 5.3 The detailed recipe used in the dry etching process using dielectric and metal reactive ion etching machine.

Etching parameter (unit)	Dielectric etching	Metal etching
Gas	CF_4, CHF_3, N_2	BCl_3, Cl_2, N_2
Temperature (°C)	20	20
Etching time (sec)	360	225
Pressure (mTorr)	20	20
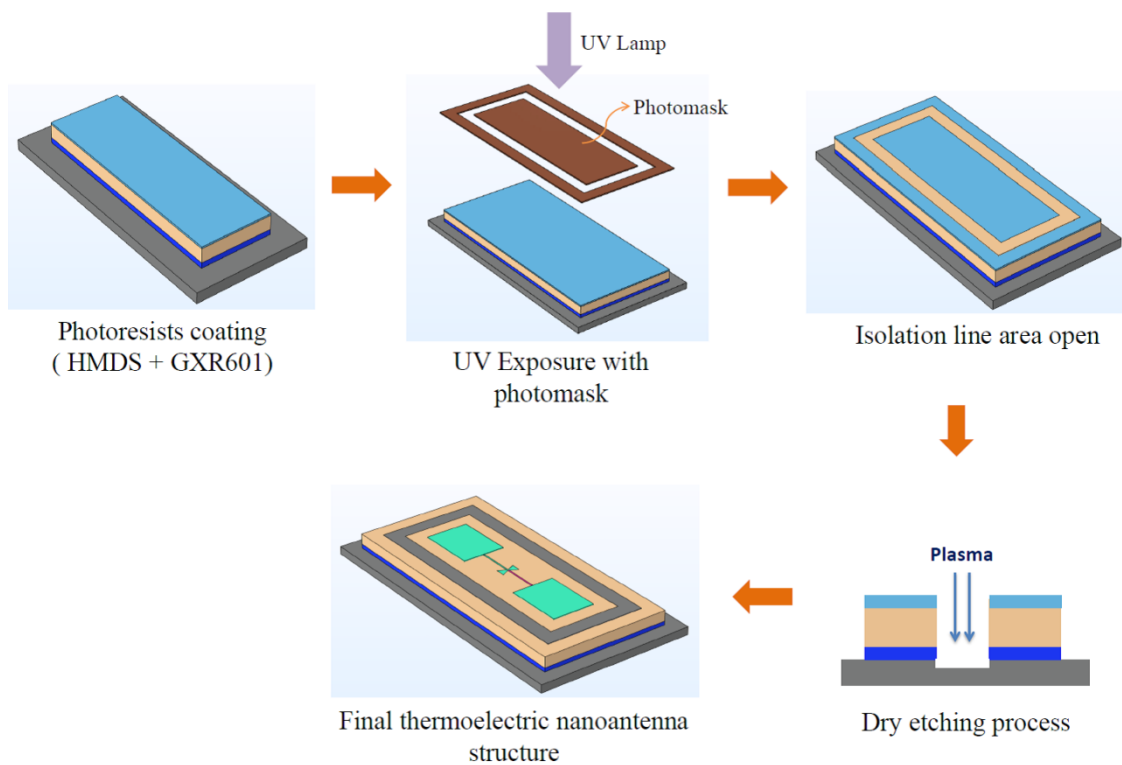
Figure 5.4 The detailed dry etching process for the device isolation line using dielectric and metal reactive ion etching machine.

Firstly, the sample was coated with HMDS + GXR 601 photoresists using spin coating with a speed of 3000 rpm for 30 seconds to achieve a 3 μm thickness of photoresists. The GXR 601 photoresists were selected instead of AZ5214E due to their ability to protect the sample from reactive ion gasses; thus, the photoresists thickness can be maintained after the dry etching process finishes. Secondly, the sample was baked on a hot plate at 110°C temperature for 90 seconds. Then, the isolation line was patterned using the MDA400S UV lithography system with a soda-lime photomask, and a UV lamp

exposed the sample with an energy of 60 MJ/Cm^2. The patterned isolation line was then developed for 2 minutes on a beaker using DPD-200 photoresists developer and shaking technique to open the isolation area. The 1.2 μm thickness of SiO$_2$ was etched using Lab star-R dielectric reactive ion etching machine with two times running (600 nm SiO$_2$ etching for each run), while the 200 nm Al ground plane was etched using a Lab star-M metal reactive ion etching machine. The detailed recipe for the dry etching process is shown in Table 5.3. After the dry etching process finished, the photoresists were removed with ultrasonic acetone for 1 minute and cleaned with an N2 gun. Finally, the residual photoresists were removed using a V15-G PR asher for 15 minutes with oxygen flow and RF power of 300 ml per minute and 200 Watt, respectively. Our devices are etched until the Si wafer to ensure good electrical insulation between the devices. The etching depth was then measured using a P-6 surface profiler and verified by ST 4000-DLX thin film measurement system using a reference silicon bar. The thickness verification was done by comparing the reflectance intensity of the reference silicon bare and the formed isolation line of the sample at a wavelength range of (400~800) nm.

5.2   Thermoelectric Nanoantenna Measurement Setup

After all fabrication processes are completed, the measurement is performed to characterize the performance of our proposed thermoelectric nanoantenna. First, we conducted DC electrical measurement to confirm the quality of the fabricated devices in terms of connectivity between the antenna, nano-thermocouple, and bonding pad. The measurement results were also used for the device's DC resistance calculation.   The second measurement is an IR measurement, and this can be done by illuminating the devices with external IR radiation to measure the V_{oc} response from the devices. Additionally, the device is illuminated with a different polarization of the incident IR waves to investigate the polarization-dependent characteristic. The detailed setup for both measurements is explained in this section.

5.2.1 Electrical Measurement

The electrical measurement aims to measure the current response of the devices with the given bias voltage. The obtained I-V curve characteristics were used to analyze the quality of the fabricated device and calculate the DC resistance. The detailed electrical measurement setup is presented in Figure 5.5. The measuring device was mounted over the

device stage in the probe station, and the device's I-V response was obtained by connecting the device's bonding pad to a Keithley 2601B source meter unit. In the measurement, the bias voltage was varied from -5 V to 5 V with a 0.1 V step level, and the measured current value with the given bias voltage was recorder and plotted on the measurement computer. Then, the device DC resistance was calculated using the slope of the I-V curve by R=dV/dI.
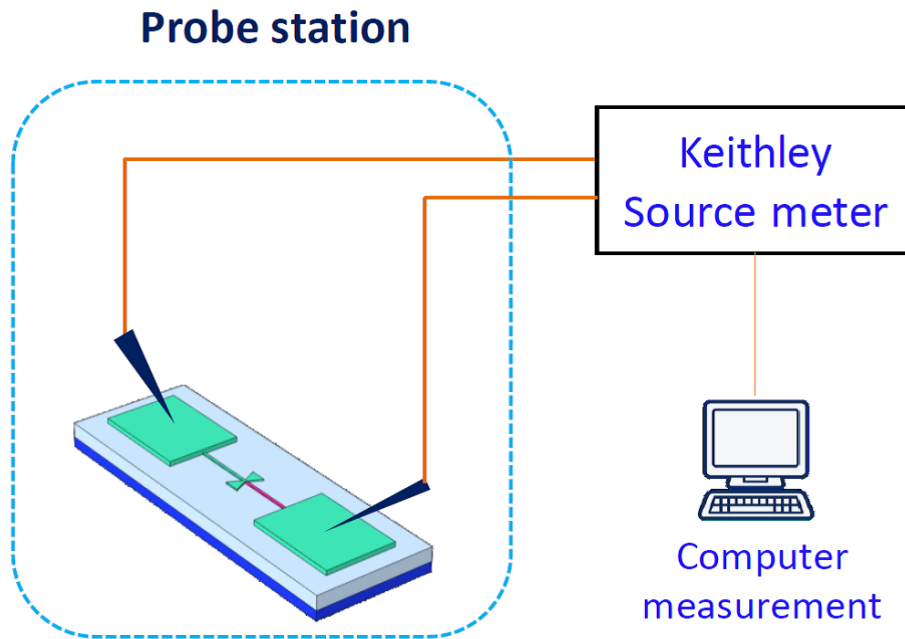
Figure 5.5 The detailed DC electrical measurement setup.

5.2.2 Infrared (IR) Measurement

We built an optical measurement setup to characterize the V_{oc} response of the thermoelectric antenna to external IR radiation, and its schematic is shown in Figure 5.6. The device was mounted on a micrometer device stage inside the probe station and connected with two measurement probes. The device was illuminated with a linearly polarized CO_2 laser (synrad 48.1) operating at a wavelength of 10.6 μm with the polarization of the electric field (E_0) parallel to the antenna axis. Because the CO_2 laser beam was invisible, we aligned a diode laser of a wavelength of 650 nm with the CO_2 laser to track the laser beam. The laser output was modulated using a mechanical chopper to form a square wave at a frequency of 1 kHz. The waves were then passed through a half-wave plate (HWP) to match the polarization to the antenna axis. The V_{oc} response of the

device was measured using an SR830 DSP lock-in amplifier with a sensitivity of 500 µV/pA.
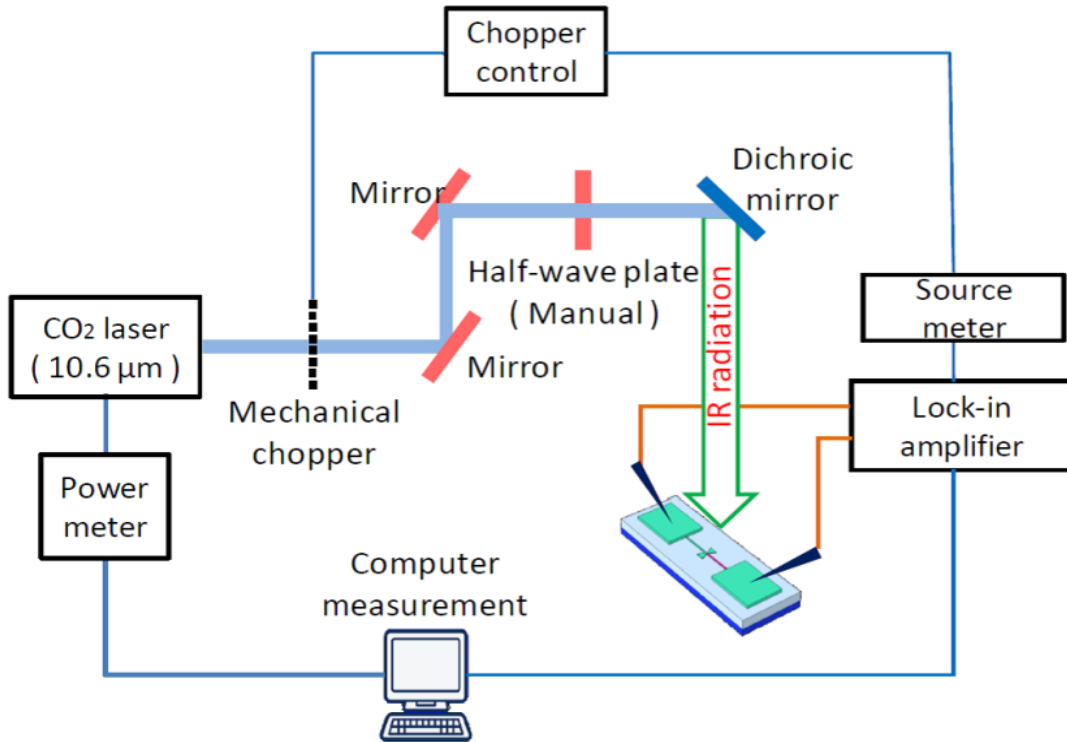
Figure 5.6 Optical measurement setup for the nanoantenna coupled with bimetal nano-thermocouple

5.3 Conclusion

This chapter presents the fabrication process and measurement setup of the proposed thermoelectric nanoantenna. The proposed thermoelectric nanoantenna was fabricated on a Si wafer using several nanofabrication techniques such as electron beam lithography (EBL), electron beam evaporation, and UV lithography. The Al ground plane and SiO_2 substrate were deposited using an e-beam evaporator and plasma-enhanced chemical vapor deposition (PECVD), respectively. The fabrication of bowtie nanoantenna and bimetal nano-thermocouple requires two-step e-beam lithography (EBL) for shape patterning and an e-beam evaporator for metallization. First, the bowtie nanoantenna and nano-thermocouple were patterned on the e-beam resist layer using an EBL system, and the metalization was done using an e-beam evaporator with a lift-off process for 5 hours. Second, the bonding pad for measurement was patterned and metalized using UV lithography and e-beam evaporation, respectively. Lastly, the dry etching for the isolation

line for electrical insulation between the devices was done using a dielectric and metal dry etching process. After all fabrication processes were completed, a DC measurement was performed to obtain the device's I-V characteristics and confirm the quality of the fabricated device. Then, an IR measurement was conducted to investigate the V_{oc} response of the device to the external IR radiation with a different polarization angle and different laser intensity to characterize the device response as an IR detector.

Chapter 6

Performance Analysis of Single Bowtie Nanoantenna Combined Bimetal Nano-thermocouple

In this chapter, the fabrication results and the performance of the fabricated devices are discussed and analyzed. First, the quality of the fabricated devices was characterized using SEM (scanning electron microscope) to measure the device size and thickness. Then, an electrical measurement was performed to check the connectivity between the antenna, nano-thermocouple, and bonding pad. Finally, IR measurement was done using the IR measurement set up to investigate the device's V_{oc} response to the external IR radiation with a different polarization angle. The measurement results showed that the proposed thermoelectric nanoantenna design achieved a high V_{oc} of 2.03 μV due to the optimum coupling between the antenna's electric field and standing waves from the open-ended SiO_2 substrate. This V_{oc} value of 2.03 μV is higher than the value of 0.4 μV from the reported bimetal nano-thermocouple-based single nanoantenna mounted on Si substrate. The proposed device also shows linear V_{oc} response with the gradually increased power density of external IR radiation, indicating that the device has a square-law detector characteristic. The detailed explanation of the device's performance and characteristics are presented and discussed in this section.

6.1   Fabrication Results

The overall device consists of a 1.2 μm thick SiO_2 substrate backed with a 200 nm-thick Aluminium (Al) ground plane. The bowtie nanoantenna made from Titanium (Ti) and bimetal nano-thermocouple made from Nickel (Ni)-Ti are directly mounted over the SiO_2 substrate. The device was fabricated over the Si wafer using nanofabrication techniques such as electron beam lithography (EBL), electron beam evaporation, UV lithography, dry etching, etc. First, the Al ground plane with 200 nm thickness and 1.2 μm-thick of SiO_2 substrate was deposited over the Si wafer using electron beam lithography

and plasma-enhanced chemical vapor deposition (PECVD). The fabrication results were checked using a scanning electron microscope (SEM) to verify the fabrication quality and geometry size of the fabricated devices. Figure 6.1 shows a cut view of an SEM image of the deposited Al and SiO_2 layers with thicknesses of 1.2 μm and 176 nm, respectively. The smaller thickness of Al compared to the target thickness of 200 nm was due to the difference in vacuum pressure during the evaporation process. However, this thickness was acceptable because of the low skin depth (~4.8 nm) of Al at 28.3 THz.
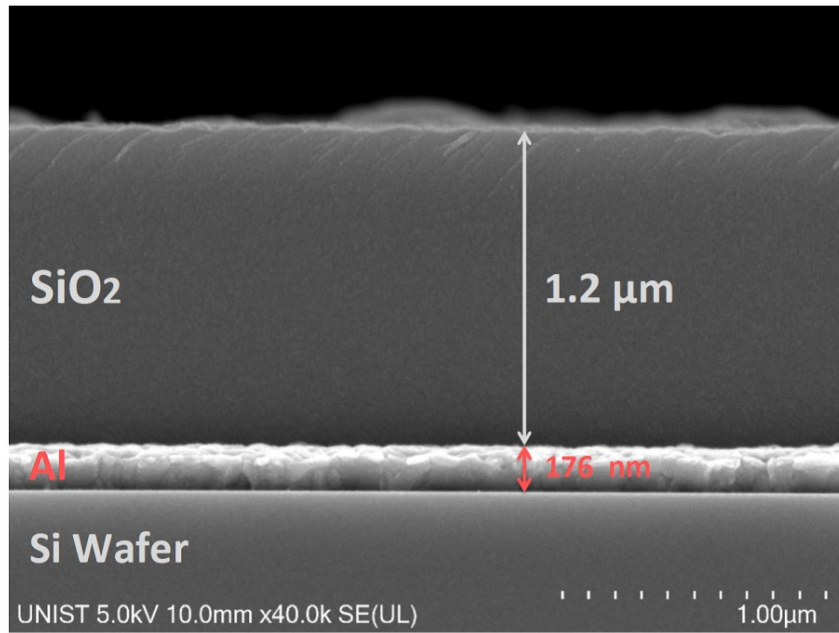
Figure 6.1 Cut view of a SEM image of the deposited 176 nm-thick Al and 1.2 μm-thick SiO_2 layer using e-beam evaporator and plasma-enhanced chemical vapor deposition (PECVD).

The fabricated devices, which consist of a bowtie nanoantenna combined with a bimetal nano-thermocouple, are shown in the SEM images in Figure 6.2. Figure 6.2(a) verifies the proper connection between the nano-thermocouple and bonding pads and reveals that the substrate size (S) and the nano-thermocouple length (L_t) are ~33 μm and 19.8 μm that correspond to the optimum dimensions of 35 μm and 20 μm, respectively. The isolation line with 10 μm width is fabricated to provide open-ended boundaries of the device. It is observable that the nanoantenna slightly moved away from the center owing to fabrication uncertainty from the photolithography of the bonding pads and its effect will be analyzed in the measurement section. Figure 6.2(b), a SEM image of the nanoantenna,

confirms that the device maintains the desired antenna length of 1225 nm and nano-thermocouple width of 70 nm via e-beam lithography.
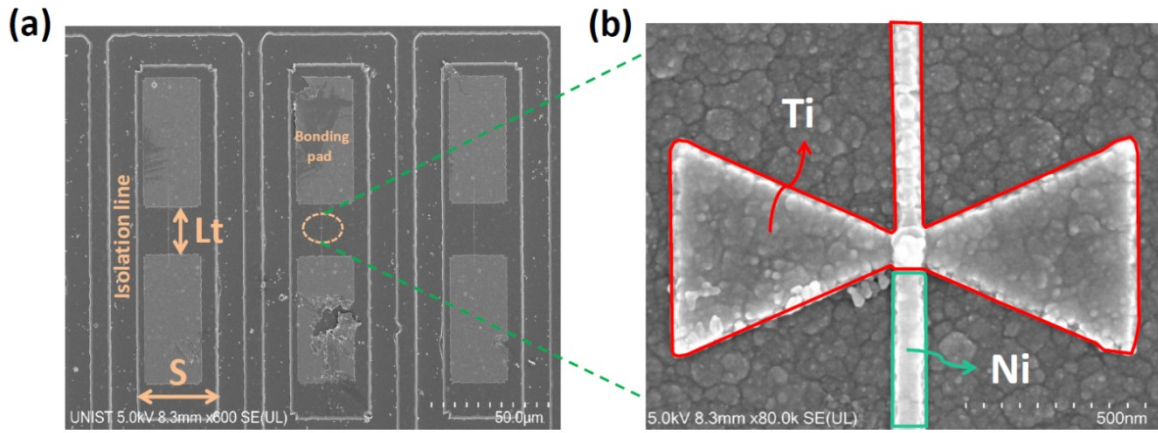
Figure 6.2. SEM image of the fabricated device (top view). (a) Single thermoelectric nanoantenna consists of a bowtie nanoantenna, bimetal nano-thermocouple, and the bonding pad. (b) The fabricated bowtie nanoantenna with the antenna length and the nano-thermocouple width are 1,225 nm and 70 nm, respectively.

In addition, the isolation area was etched using dielectric and metal etching machines with an etching depth of 1.4 μm until the Si wafer to ensure good electrical insulation between the devices. To verify the etching quality, the etching depth verification using a ST4000-DLX thickness measurement system was performed to compare the reflectance intensity of reference silicon bare and the formed isolation line in the fabricated device. Figure 6.3 shows the comparison reflectance intensity from the silicon bare and the device isolation line at (400~800) nm wavelength. It is seen from Figure 6.3 that the intensity signal from reference silicon (blue line) and the formed isolation line (gray line) has the same magnitude along with the wavelength range, indicating that the isolation line was etched until the Si wafer. Additionally, a contact measurement using a P-6 surface profiler was also performed to extract the topographic data from the sample and determine the etching depth of the isolation line. The measurement was done by moving a probe along the surface to acquire the surface height to reference. In our measurement, the reference surface is the SiO_2 layer since the etching depth is calculated relative to the SiO_2. Figure 6.4 shows the etching depth measurement of the isolation line along the surface, and it is seen that the etching depth of ~1.4 μm was achieved. This result satisfies with the

previous verification using thickness measurement, as shown in Figure 6.3. In addition, the etching depth deviation of 0.017 μm from the scan length in Figure 6.4 indicates a small surface roughness of the deposited SiO_2 layer.
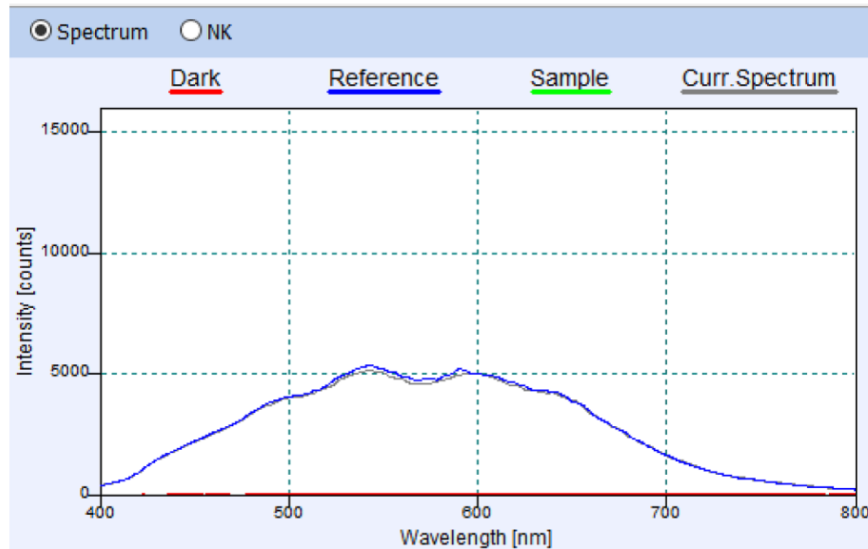
Figure 6.3. Reflectance intensity of the reference silicon bare and the formed isolation line of the sample at a wavelength range of (400~800) nm.
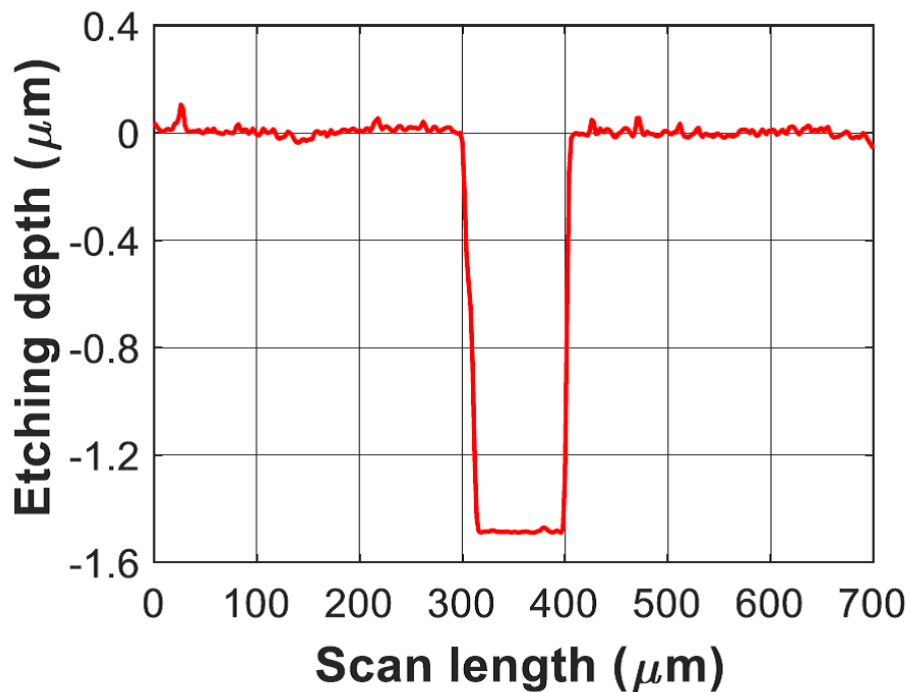
Figure 6.4. The measured etching depth along with the scanned length, the measurement was done using a surface profiler.

6.2   Discussion on Device Measurement

The fabricated devices were then measured to verify the device performance to the external IR radiation. First, an electrical DC measurement was performed to check the device connectivity and calculate the DC resistance of the device. Then, an open-circuit voltage (V_{oc}) measurement was carried out to understand the device characteristics with a different polarization angle of incident IR radiation. The V_{oc} measurement with different laser power density was then performed to characterize the linearity of device response. Lastly, the lateral substrate size (S) effect was also investigated by measuring the V_{oc} from the thermoelectric nanoantenna device with a different lateral substrate size (S). This measurement aims to prove the optimum V_{oc} provided by the optimum substrate size (S) due to the coupling between standing waves and electric fields from the antenna.

6.2.1 DC Electrical Measurement
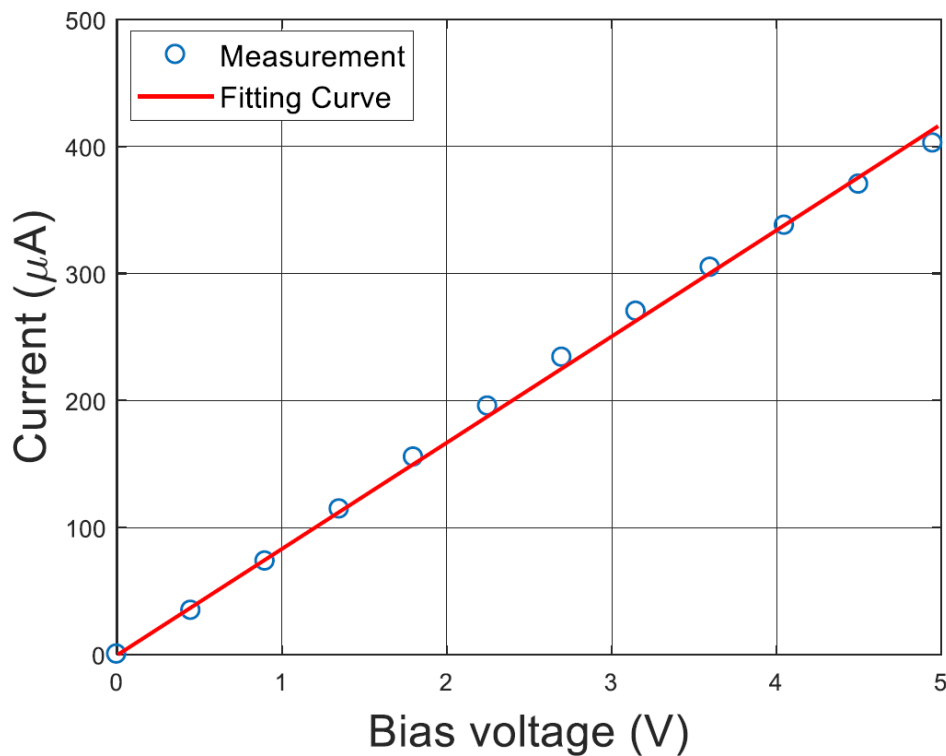
Figure 6.5 The measured I–V response of the device with bias voltage varying from 0 to 5 V.

First, we verified the physical connectivity between the bowtie nanoantenna and bimetal nano-thermocouple by measuring the DC resistance from the measurement pads. We applied voltages to the pads using two probes from a Keithley source meter and determined the I–V response. Figure 6.5 shows the measured I–V curve of the device with a voltage variation between 0 and 5 V in steps of 0.1 V. The linearity of the current response indicates proper connectivity with a DC resistance of 12.5 kΩ, which is calculated as Rdc = dV/dI.

6.2.2 V_{oc} Dependence of Power Density and Polarization Variation

We measured the V_{oc} response of the devices by varying the laser power density to verify whether the device response originated from external IR radiation. During the measurement, the polarization angle (θ) was set to be 0°, where the antenna axis was aligned with the polarization vector of the incident IR wave. Figure 6.6 shows the measured Voc response with laser power densities ranging from 0 to 2 W/cm2. The almost zero V_{oc} for zero laser intensity confirms that V_{oc} from the device does not originate from external noise signals. The linear response of V_{oc} to the laser power density indicates the nature of the square-law detector [58], [167]. A higher input power density increases the current density at the antenna center and results in a larger ΔT between the hot and cold junctions.
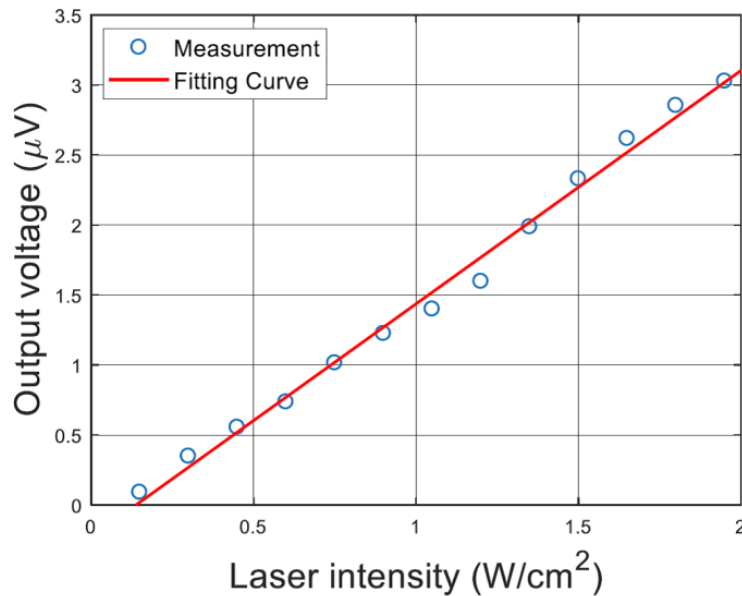
Figure 6.6. Measured V_{oc} of the thermoelectric antenna with laser power densities varying from 0 to 2 W/cm^2.

We then measured the polarization-dependence of V_{oc} by rotating the HWP to change the polarization angle (θ) of the linearly polarized incident wave. The polarization angle (θ) is defined as the angle between the antenna axis and polarization vector of the electric field. Figure 6.7 shows the measured V_{oc} as a function of θ based on a fixed laser power density of 1.48 W/cm2. The 0° polarization angle provides a maximum V_{oc} of 2.03 µV and the peaks repeat every 180°, where the incident polarization aligns with the antenna axis. The measurement results confirm that the proposed device with resonance from an open-ended substrate outperforms a similar Si-mounted thermoelectric nanoantenna with V_{oc} of 0.4 µV by five times [157].
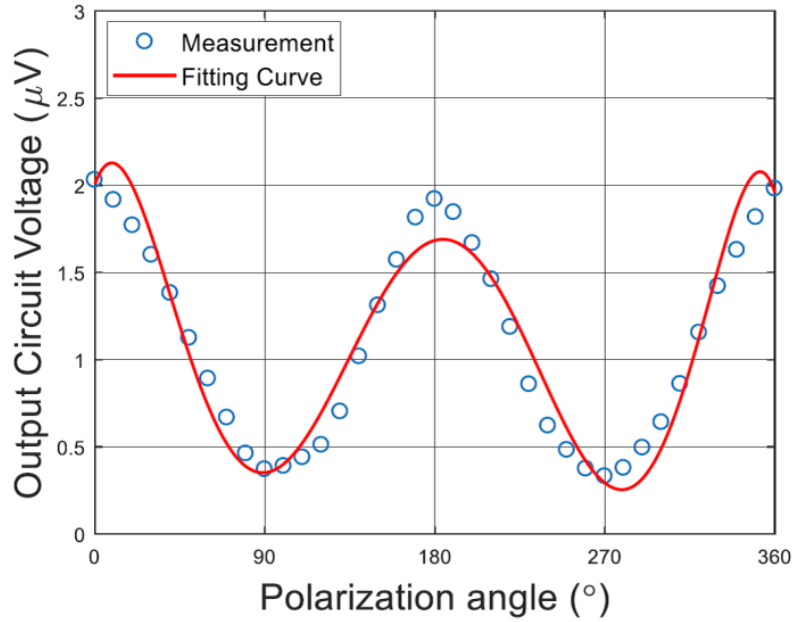
Figure 6.7 Measured V_{oc} response of the device with different polarization angles.

Figure 6.7 shows a cosine squared curve of the V_{oc} response, which corresponds to the linear polarization nature of the dipole antenna [168]. The polarization-dependent V_{oc} confirmed that the source of the output signal was the absorption of the nanoantenna. In this device, the total $V_{oc(\theta)}$, which is a function of $V_{oc}(\perp)$ and $V_{oc}(\parallel)$ which are the V_{oc} values from perpendicular and parallel polarizations, respectively, and θ can be formulated as shown in Equation (2).

$$V_{oc(\theta)} = V_{oc(\perp)} + V_{oc(\parallel)} \cos^2(\theta - \theta_0) \tag{6.1}$$

where θ_0 is the specific angle that provides maximum V_{oc}. Here, θ_0 is 0°, where the antenna axis is aligned with the polarization vector of the input IR wave. It should be noted that the polarization-dependent V_{oc} response does not reach zero voltage for $\theta = 90°$ and 270°, where the antenna axes and incident polarization vector are perpendicular. We expect that the non-negligible V_{oc} of 0.06 μV in both cases can be attributed to fields excited inside the finite-sized SiO_2 substrate and thermionic emission-related current flows in the thermocouple from the IR illumination [169]–[171].

6.2.3 V_{oc} Dependence on SiO_2 Size Variation
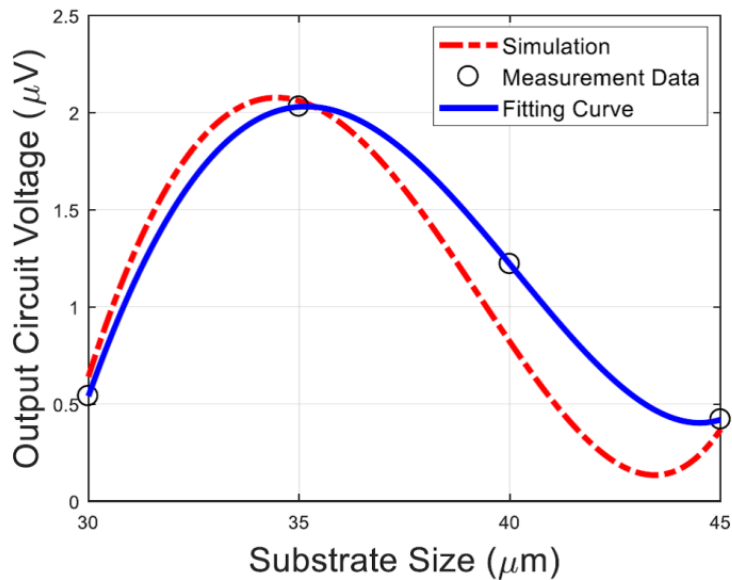
Figure 6.8. V_{oc} response of the device with different substrate sizes at 0° polarization angle of the incident laser.

Finally, we investigated the effect of the horizontal size (S) of the open-ended SiO_2 substrate on V_{oc} of the thermoelectric nanoantenna. We fabricated devices with optimum metallic structures by varying S from 30 to 45 μm with a 5 μm gap and measured V_{oc} at 0° polarization angle. Figure 6.8 presents the measured and simulated S-dependent V_{oc} responses, which confirm that the highest V_{oc} of 2.03 μV comes from S of 35 μm. This V_{oc} value is four times higher than the minimum V_{oc} of approximately 0.5 μV from S = 30 μm and 45 μm. S of 40 um provides an intermediate V_{oc} of 1.2 μV. Through this measurement result, we prove for the first time that standing waves generated from open-ended thermoelectric antenna devices contribute to a significant improvement in V_{oc}.

Furthermore, we noted a minor shift between the measured and simulated data, and found that a reduction in S moved the V_{oc} maximum to the right side in the simulations. The reduced device size owing to the uncertainty of UV lithography can be attributed to this shift.

In addition, we measured polarization-dependent V_{oc} for S = 30 µm and 40 µm on top of S = 35 µm to confirm the dipole-like responses. Figure 6.9 shows the cosine-shaped V_{oc} responses as a function of θ for S = 30, 35, and 40 µm, and confirms that all the V_{oc} responses result from the polarization-dependent IR absorption of the nanoantenna. It is to be noted that at 90° polarization angle, the device with S = 35 µm provides a higher V_{oc} of 0.36 µV than 0.11 µV from the other two cases. To check whether S can affect V_{oc} at θ = 90°, we calculated the electric field distributions for substrate sizes (S) of 30 and 35 µm, as shown in Figure 6.10. The results show that the S values of 30 and 35 µm provide similar standing wave patterns near the antenna center. The standing waves have the maximum magnitude at the center of the y-axis and created constructive coupling with the antenna. This pattern led to a similar V_{oc} level for both sizes and proved that S did not affect V_{oc} at θ = 90°. Therefore, the device-dependent V_{oc} at 90° polarization angle in the measurement is partially due to the shift in the antenna position along the y-axis during the fabrication process.
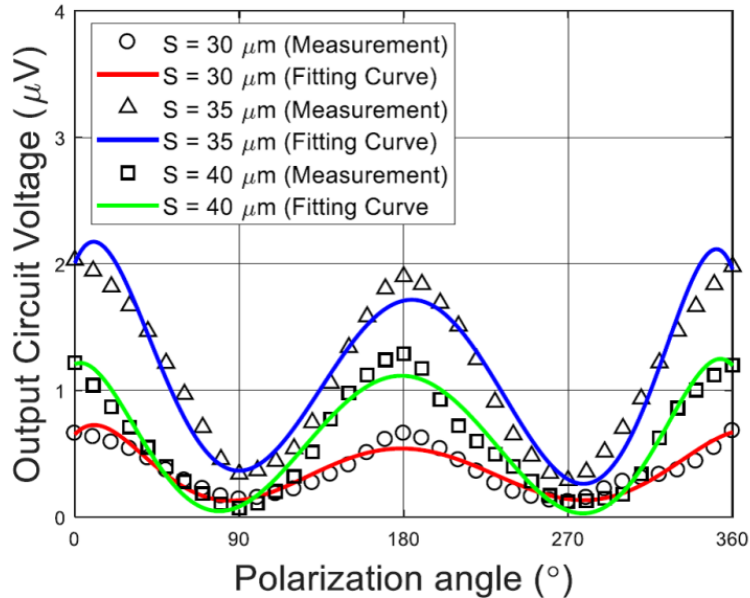
Figure 6.9. Polarization-dependent measurement of V_{oc} responses for different substrate sizes.
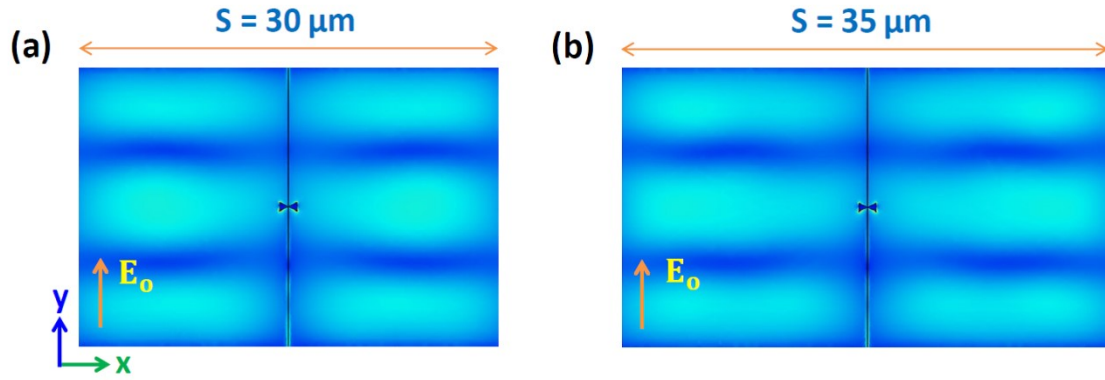
Figure 6.10. The simulation results of electric field distribution along x–y plane for substrate sizes of 30 μm and 35 μm at 90° polarization angle.

6.3 Device Performance Comparison

Performance comparison of the proposed work with the other counterparts measured with a similar level of input laser power density is provided in **Table 1**, and a normalized V_{oc} ($V_{oc, norm}$), which is V_{oc} normalized by an input power density of 1.48 W/cm^2, is added for a fair comparison. The $V_{oc, norm}$ is formulated as $V_{oc, norm} = V_{oc[ref]} \times (P_{d[this\ work]} / P_{d[ref]})^{1/2}$, where the V_{oc} and P_d are the output voltage and laser power density, respectively. Table 1 clearly shows that the proposed device achieves the highest $voice, norm$ with a 4-fold increase compared to the reported thermoelectric nanoantennas on a grounded substrate. Additionally, the measured V_{oc} of 2.03 μV from our device corresponds to an output power (P_{out}) of 3.29×10^{-16} W, calculated using $P_{out} = V_{oc}^2/R_{DC}$, where V_{oc} and R_{dc} are the output voltage and DC resistance of the device, respectively. Meanwhile, the device generates current (I) of 1.6×10^{-10} A which is determined by $I = V_{oc}/R_{dc}$. We understand that the power and current which are generated by our device are still low; however, compared to the infrared (IR) energy harvesting devices based nanoantenna combined diode, our proposed device has ten times better performance in terms of power conversion efficiency. The nanoantenna combined diode shows high diode resistance and leads to low power transfer from the antenna to the diode. Our devices offer higher V_{oc} because the device does not require an impedance matching technique for maximum power transfer between antenna and nano-thermocouple.

Table 6.1. Performance comparison of the present study with state-of-the-art single thermoelectric nanoantenna structure studies for V_{oc} measurement

Ref.	Year	Structure	Laser density	ΔT (mK)	V_{oc}	$V_{oc(norm)}$*
[167]	2013	Single metal Pd dipole antenna on grounded substrate combine bimetal (Pd-Au) nano-thermocouple	1.42 W/cm^2	46 mK	132 nV	0.0134 μV
[156]	2015	Single metal Pd dipole antenna on grounded substrate combne single metal (Pd) nano-thermocouple	1.42 W/cm^2	40.98 mK	0.025 μV	0.025 μV
		Single metal Pd dipole antenna on grounded substrate combne bimetal (Pd-Au) nano-thermocouple		42.66 mK	0.125 μV	0.127 μV
[157]	2019	Single metal Pd dipole antenna combined single metal (Pd) nano-thermocouple	1.42 W/cm^2	~25 mK (on substrate) ~91.6 mK (on membrane) ~2.08 K (suspended)	0.03 μV (on substrate) 0.11 μV (on membrane) 2.5 μV (suspended)	0.03 μV (substrate) 0.11 μV (membrane) 2.55 μV (membrane)
		Single metal Pd dipole antenna combned bimetal (Ni-Pd) nano-thermocouple		~44.4 mK (on substrate) ~266.6 mK (on membrane) ~4.22 K (suspended)	0.4 μV (on substrate) 2.4 μV (on membrane) 38 μV (suspended)	0.41 μV (substrate) 2.45 μV (membrane) 38.79 μV (suspended)
This work	**2021**	**Single metal Ti bowtie antenna on grounded substrate combne bimetal (Ni-Ti) nano-thermocouple**	**1.48 W/cm^2**	**76.33 mK (on substrate)**	**2.03 μV**	**2.03 μV**

Based on the investigations mentioned, we concluded that the proposed thermoelectric nanoantenna design is one of the promising structures to improve the performance of nanoantenna-based IR harvesting devices. Additionally, we designed the proposed devices consisting of a single metal nanoantenna with low thermal conductivity to maintain the high temperature at the antenna center. Then, a bimetal nano-thermocouple was chosen due to its high difference in the Seebeck coefficient and connected to the antenna terminal to generate high V_{oc}. In the fabrication, we fabricated the device on fabricable Silicon (Si) wafer and utilized the optimum wafer size to guide the standing waves in a proper position to increase efficiency. This design concept allows the fabricated

devices to have better stability due to the antenna and the nano-thermocouple are directly placed on the substrate instead of hanging over the air-filled cavity.

6.4 Conclusion

The proposed device was fabricated using common nanofabrication methods such as electron beam lithography (EBL), electron beam evaporation, and UV lithography. Then, the fabricated device was characterized using a *scanning electron microscope* (SEM) to confirm the fabrication quality. The I−V curve measurement was performed to satisfy the connectivity between the antenna, nano-thermocouple, and bonding pad. Then, the device's V_{oc} response was measured in the probe station and IR measurement system using a CO_2 laser with a 10.6 μm wavelength. A V_{oc} of 2.03 μV was measured from a fabricated device via a 28.3 THz CO_2 laser-based measurement setup. This value is five times higher than the 0.4 μV of another thermoelectric antenna mounted on a grounded substrate [157]. We also verified that the V_{oc} response of the fabricated devices depends on the horizontal substrate size, proving that the horizontal bouncing standing wave from the open-ended SiO_2 boosted V_{oc} by five times. This is the first reported phenomenon in a thermoelectric antenna and is groundbreaking because the fabrication process does not degrade the stability of the device, unlike the recently reported thermoelectric antennas hanging up over an air-filled cavity [157], [158]. Therefore, we expect that the proposed thermoelectric nanoantenna design will be a viable solution for a high output IR harvester using massive nanoantenna arrays.

Chapter 7

Conclusions and Future Work

7.1   Summary of Achievements

This dissertation presents a novel plasmonic nanoantenna design to achieve a high field enhancement and absorption rate in the IR frequency range. The novel design method can overcome the limitations of a conventional nanoantenna design using a grounded substrate. To achieve this goal, we designed a bowtie nanoantenna array combined with an artificial impedance surface to realize high field enhancement and absorption rate at the same time. Also, the artificial surface with high surface reactance characteristics was investigated and utilized to improve the absorption efficiency of the IR absorber-based MIM (metal insulator metal) structure. In addition, for IR energy harvesting application, a thermoelectric nanoantenna was investigated, and its response in terms of open-circuit voltage (V_{oc}) was measured and analyzed.

Firstly, nanoantenna combined with artificial impedance surface was presented, and the novel nanoantenna design concept can simultaneously achieve high field enhancement and absorption rate. The optimization method uses a bowtie nanoantenna array combined with artificial impedance surfaces that acts as a high impedance surface (HIS) and reactive impedance surface (RIS) with resistive and inductive characteristic, respectively, at the resonant frequency. The results showed that the nanoantenna array combined with the HIS could not achieve a high absorption rate due to the reflective nature of HIS. Finally, the bowtie nanoantenna array mounted over the highly inductive characteristic of RIS achieved a field enhancement value of 228 and a near-perfect absorption rate of 98% at 230 THz. Our approach to the nanoantenna design method overcomes the limitation of the conventional nanoantenna designed on grounded dielectric substrates. We then investigated the surface roughness effect and showed that the proposed RIS-combined nanoantenna's performance is less degraded than conventional nanoantenna on grounded dielectric substrates. We conclude that the proposed RIS-combined bowtie

nanoantenna array with superior performance can be used to improve the efficiency of IR and optical detectors, plasmonic sensors, and IR energy harvesting devices.

In the subsequent investigation, an IR absorber based on a circular nanodisk array combined with a RIS was presented to achieve near-perfect absorption with high field enhancement near-IR range. The proposed IR absorber achieved near-perfect absorption of 98% with the electric field enhancement value of 180 at 230 THz due to the impedance matching between the structure and the surrounding medium. This value is even higher than the value of 81% and 174 from the circular nanodisk array on 40 nm on a conventional grounded substrate. Hereinafter, we investigated the ability of the proposed structure for polarization-independent response by illuminating the structure with $x-$ and $y-$polarized incident waves. The results showed that the proposed structure was stable even with polarization changes due to the symmetrical arrangement of the circular nanodisk and RIS. Based on the performance of the proposed structure, we conclude that a RIS-integrated MIM absorber with near-perfect absorption and superior field enhancement can be used to enhance the sensitivity of sensors, such as LSPR sensors and surface-enhanced infrared spectroscopy.

For an IR harvesting device application, a single nanoantenna combined with a bimetal nano-thermocouple, or called as thermoelectric nanoantenna was investigated. A bowtie nanoantenna made from a single metal, titanium (Ti), was designed to capture IR radiation and generate a high-temperature difference (ΔT) between the antenna center and relatively cold area. The antenna made from single metal guarantees high temperature in the gap by reducing heat flow due to a low thermal conductivity gap. Then, a pair of nickel (Ni) and titanium (Ti), which function as a nano-thermocouple was connected to the antenna center to convert the temperature difference (ΔT) into an output voltage (V_{oc}) through Seebeck effect. Our optimization method involved the optimum coupling between the antenna's electric field and standing waves from the SiO_2 substrate with a quarter-wavelength thick. The optimized antenna size achieved a maximum ΔT of 76.33 mK (equal to V_{oc} of 2.06 μV) at 28.3 THz, corresponding to series resonance from the antenna input impedance calculation. The proposed thermoelectric nanoantenna was then fabricated over a Silicon wafer using a common nano-fabrication technique such as electron beam lithography (EBL), electron beam evaporation, and UV lithography.

For device characterization, an electrical measurement was performed to calculate the device's DC resistance and confirm the fabrication quality in terms of the connectivity

between the antenna, the nano-thermocouple, and the bonding pad. Next, the V_{oc} response from the device was measured using an IR measurement setup using a CO_2 laser with a 10.6 μm wavelength and intensity of 1.4 W/cm^2. The measurement results showed that the proposed thermoelectric nanoantenna generates V_{oc} of 2.03 μV. This value is higher among the state-of-the-art thermoelectric nanoantenna mounted on grounded substrates. Also, polarization-dependent measurement showed that the cosine function from the V_{oc} response of our proposed devices follows the classical dipole antenna theory. We then investigated the effect of lateral substrate size on the V_{oc} and found that maximum V_{oc} occurs when the substrate size is 35 μV, this size provides in-phase coupling between the antenna's electric fields and standing waves. Additionally, the stability of our proposed thermo-electric nanoantenna device would be improved since the antenna and nano-thermocouple are directly placed on the substrate rather than hanging up over the air-filled cavity. Therefore, we claimed that the proposed thermoelectric nanoantenna design concept would be a promising method to realize practical IR harvesting devices.

7.2   Future Work

In this dissertation, full-wave simulation results related to nanoantenna optimization for achieving high field enhancement and absorption rate were presented. Moreover, the field enhancement can still be increased by combining the structure with a focusing nano lens. This structure enabled the incident wave to be enhanced several times and focused properly into the structure; thus, a giant field enhancement would be achieved. Additionally, the fabrication process using nanofabrication technique and measurement has not been done before and can be considered in future work. Using the currently available nanofabrication techniques, the nanometer-sized gold antenna can be patterned using electron beam lithography (EBL) [172]–[174], and the SiO_2 dielectric substrate with micrometer thickness can be deposited using plasma-enhanced chemical vapor deposition (PECVD) [175]–[177]. The deposition of gold inside the SiO_2 dielectric substrate for patch array fabrication might be the most challenging part; however, that problem can be solved by patterning gold inside SiO_2 and etching using the reactive ion etching (RIE) technique [178]. For nanoantenna measurement, the field distribution of the proposed nanoantenna structure can be visualized using near-field scanning optical microscopy (SNOM) with the scattering scanning method [179]. Another technique to visualize the near-field distribution of nanoantenna is using a near-field optical vector network analyzer method

[180]. The electric field magnitude of the nanoantenna structure is then determined from the field distribution; thus, field enhancement at a specific area that can be calculated. Meanwhile, the absorption rate can be measured using Fourier transform infrared (FTIR) spectrometer combined optical microscope. The absorption rate can be calculated from the reflectance provided by the FTIR spectrum at the near-infrared regime.
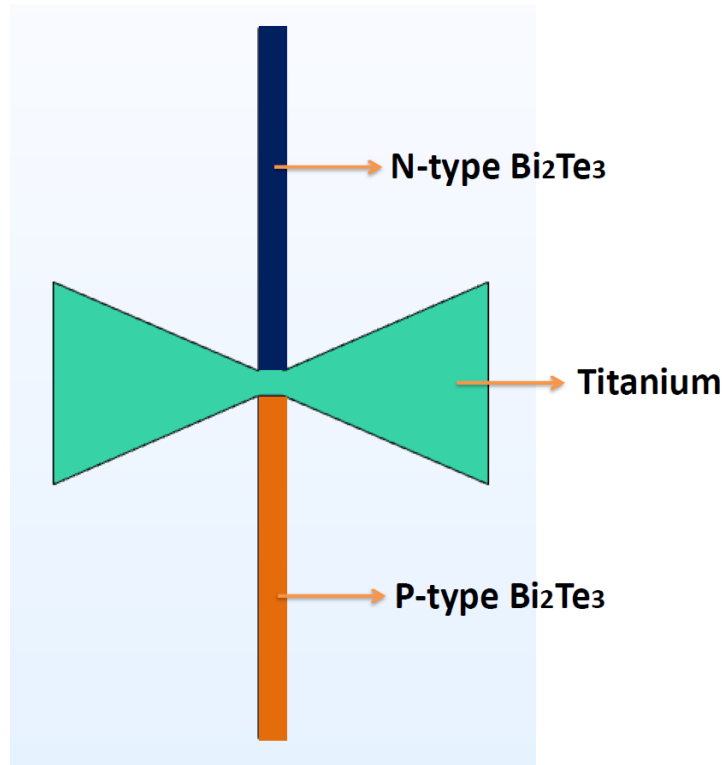
Figure 7.1 A novel single thermoelectric nanoantenna structure consists of a bowtie nanoantenna combined n-type and p-type bismuth telluride (Bi_2Te_3) as a pair of nano-thermocouple.

For energy harvesting purposes, a thermoelectric nanoantenna consisting of a single bowtie nanoantenna combined with a bimetal nano-thermocouple was presented. Even though the proposed produces a high V_{oc} of ~2 μV among the state-of-the-art thermo-electric nanoantenna on a dielectric grounded substrate, the calculated efficiency of ~10^{-9}% is still low and needs to be improved. The efficiency can be improved by increasing the produced V_{oc} and lowering the DC resistance of the device. To achieve that goal, ΔT between the hot and cold junction should be high enough, and this can be realized by increasing the current density at the antenna center; thus, the high V_{oc} would be achieved. Since V_{oc} is directly proportional to the relative Seebeck coefficient (ΔS), thus, other methods to improve V_{oc} is by increasing the relative Seebeck coefficient of the nano-

thermocouple. Instead of using metal as a nano-thermocouple, the utilization of a pair of thermoelectric materials such as n-type and p-type of bismuth telluride (Bi_2Te_3), as shown in Figure 7.1, would provide ultrahigh ΔS and the V_{oc} will eventually increase significantly. Meanwhile, lowering the DC resistance can be done by improving the nanoantenna fabrication quality, especially in the connection between the antenna gap and nano-thermocouple. To achieve that purpose, misalignment during shape patterning using EBL should be avoided so that the contact area between the antenna gap and the nano-thermocouple is large enough. The DC device's resistance will be high if the contact area is too small due to the misalignment since the resistance is inversely proportional to the area. Another way to reduce the DC resistance is by selecting a low resistivity material for the antenna and nano-thermocouple. However, the fabrication of this structure would be a challenging task because it involves metal and semiconductor patterning simultaneously during the nanofabrication process.
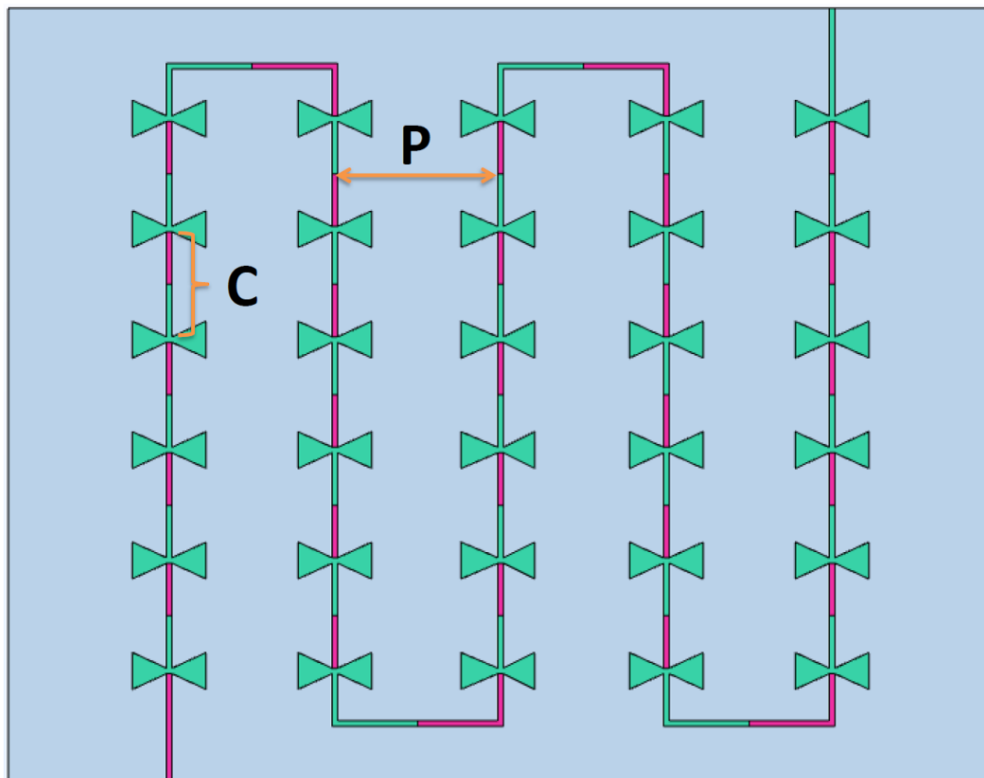
Figure 7.2 The schematic design of 5 × 6 thermoelectric nanoantenna array consists of 30 antennae in a series connection.

Another method to boost V_{oc} is connecting several antennas in a series connection and arranging them in a finite array structure. Firstly, the nano-thermocouple length (C)

and the antenna pitch size (P) are optimized based on the position of standing waves to obtain the optimum V_{oc} value for each parameter. Here, the nano-thermocouple length (C) and antenna pitch size (P) are defined as the distance between two antennas in the vertical and horizontal positions, respectively. Finally, the finite thermoelectric nanoantenna structure can be designed using the optimum C and P, where the standing waves from the substrate with a quarter-wavelength thick are mostly coupled to the antenna in the array. Figure 7.2 shows the schematic design of the (5 × 6) thermoelectric nanoantenna array, consisting of 30 antennas in series connection. Even though the array structure with the higher number of antennas would experience a decrease of ΔT due to heat energy density distribution along with the structure, the sum of V_{oc} from each element in the array allows the higher V_{oc} compared to V_{oc} from a single thermoelectric nanoantenna.

7.3   List of Publications

International journal:

1. **Anam, M.K** and Choi, S. (2020). Perfect absorption efficiency circular nanodisk array integrated with a reactive impedance surface with high field enhancement. *Nanomaterials*. 10(2). 258. (SCIE, IF 5.719)

2. **Anam, M.K** and Choi, S. (2020). Bowtie nanoantenna array integrated with artificial impedance surfaces for realizing high field enhancement and perfect absorption simultaneously. *IEEE Access*. 8. 99858-99869. (SCIE, IF 3.367)

3. **Anam, M.K** and Choi, S. (2022). Infrared Thermoelectri Nanoantenna with Maximum Output Voltage Using Grounded and Open-Ended SiO_2. *Advanced Optical Materials* (in preparation).

International conferences:

1. **Anam, M. K** and Choi, S. (2020). Nanoantenna Array Design on Grounded Dielectric Substrate for High Field Enhancement and Absorption. *2020 IEEE Wireless Communications and Networking Conference Workshops (WCNCW)* (pp. 1-4). Seoul, South Korea.

2. **Anam, M.K** and Choi, Sangjo. (2020). Nanoantenna array integrated with reactive impedance surface (RIS) for achieving perfect absorption with high field

enhancement. *2020 IEEE International Symposium on Antenna and Propagation*, Montreal, Canada.

Domestic conferences:

1. **Anam, M.K** and Choi, S. (2019). Perfectly matched nanoantenna array integrated with artificial impedance surface for high field enhancement. *2019 KIEES Summer Conference*. Jeju, South Korea.

2. **Anam, M.K** and Choi, S. (2020). Design optimization of thermoelectric nanoantenna for infrared (IR) harvesting applications. *2020 KIEES Summer Conference*. Jeju, South Korea.

3. **Anam, M.K** and Choi, S. (2021). Thermoelectric nanoantenna optimization via standing waves interference for infrred (IR) harvester. *2021 KIEES Winter Conference*. Yeosu, South Korea.

4. **Anam, M.K** and Choi, S. (2021). Polarization dependent single thermoelectric nanoantenna for infrared (IR) harvesting and detection appliations. *2021 KIEES Summer Conference*. Jeju, South Korea.

Patent:

1. Choi, S and **Anam, M.K**. (2020). Bowtie nanoantenna array structure (Korean Patent No. 10-2181804-0000). *Korean Intellectual Property Office (KIPO)*. https://doi.org/10.8080/1020190139267.

2. Choi, S and **Anam, M.K**. (2022). Perfect Absorption Efficiency Circular Nanodisk Array Integrated with a Reactive Impedance Surface with High Field Enhancement. *Korean Intellectual Property Office (KIPO)*. https://doi.org/10.8080/1020200072360.

REFERENCES

[1]   M. A. Bramson, "Infrared radiation: a handbook for applications, with a collection of reference tables," 1968.

[2]   W. L. Wolfe, *The infrared handbook*, vol. 10. The Office, 1978.

[3]   R. D. Hudson, *Infrared system engineering*, vol. 1. Wiley-Interscience New York, 1969.

[4]   A. Rogalski, *Infrared and terahertz detectors*. CRC Press, 2019.

[5]   E. F. J. Ring, "The discovery of infrared radiation in 1800," *The Imaging Science Journal*, vol. 48, no. 1, pp. 1–8, 2000.

[6]   M. Iqbal, *An introduction to solar radiation*. Elsevier, 2012.

[7]   J. M. Robinson, "Fire from space: Global fire evaluation using infrared remote sensing," *International Journal of Remote Sensing*, vol. 12, no. 1, pp. 3–24, 1991.

[8]   A. F. Bagley, S. Hill, G. S. Rogers, and S. N. Bhatia, "Plasmonic photothermal heating of intraperitoneal tumors through the use of an implanted near-infrared source," *ACS nano*, vol. 7, no. 9, pp. 8089–8097, 2013.

[9]   K.-N. Lee, D.-S. Lee, S.-W. Jung, Y.-H. Jang, Y.-K. Kim, and W.-K. Seong, "A high-temperature MEMS heater using suspended silicon structures," *Journal of Micromechanics and Microengineering*, vol. 19, no. 11, p. 115011, 2009.

[10]   M. Kulick, "Evaluation of the combination of radio frequency, infrared energy and mechanical rollers with suction to improve skin surface irregularities (cellulite) in a limited treatment area," *Journal of Cosmetic and Laser Therapy*, vol. 8, no. 4, pp. 185–190, 2006.

[11]   T. J. Wieting and J. L. DeRosa, "Effects of surface condition on the infrared absorptivity of 304 stainless steel," *Journal of Applied Physics*, vol. 50, no. 2, pp. 1071–1078, 1979.

[12]   R. B. Barnes, "Thermography of the Human Body: Infrared-radiant energy provides new concepts and instrumentation for medical diagnosis.," *Science*, vol. 140, no. 3569, pp. 870–877, 1963.

[13]   L. J. Jiang *et al.*, "A perspective on medical infrared imaging," *Journal of medical engineering & technology*, vol. 29, no. 6, pp. 257–267, 2005.

[14]   H. Dehghani *et al.*, "Near infrared optical tomography using NIRFAST: Algorithm for numerical model and image reconstruction," *Communications in numerical methods in engineering*, vol. 25, no. 6, pp. 711–732, 2009.

[15]   X. Song *et al.*, "Automated region detection based on the contrast-to-noise ratio in near-infrared tomography," *Applied optics*, vol. 43, no. 5, pp. 1053–1062, 2004.

[16]   G. Gaussorgues and S. Chomet, *Infrared thermography*, vol. 5. Springer Science & Business Media, 1993.

[17]   B. B. Lahiri, S. Bagavathiappan, T. Jayakumar, and J. Philip, "Medical applications of infrared thermography: a review," *Infrared Physics & Technology*, vol. 55, no. 4, pp. 221–235, 2012.

[18]   C. Meola and G. M. Carlomagno, "Recent advances in the use of infrared thermography," *Measurement science and technology*, vol. 15, no. 9, p. R27, 2004.

[19]   K. Schreiner, "Night vision: infrared takes to the road," *IEEE Computer Graphics and Applications*, vol. 19, no. 5, pp. 6–10, 1999.

[20] T. Tsuji, H. Hattori, M. Watanabe, and N. Nagaoka, "Development of night-vision system," *IEEE Transactions on Intelligent Transportation Systems*, vol. 3, no. 3, pp. 203–209, 2002.

[21] L. J. Jiang *et al.*, "A perspective on medical infrared imaging," *Journal of medical engineering & technology*, vol. 29, no. 6, pp. 257–267, 2005.

[22] E. F. J. Ring and K. Ammer, "The technique of infrared imaging in medicine," *Thermology international*, vol. 10, no. 1, pp. 7–14, 2000.

[23] K. Krishnamurthy, H. K. Khurana, J. Soojin, J. Irudayaraj, and A. Demirci, "Infrared heating in food processing: an overview," *Comprehensive reviews in food science and food safety*, vol. 7, no. 1, pp. 2–13, 2008.

[24] N. K. Rastogi, "Recent trends and developments in infrared heating in food processing," *Critical reviews in food science and nutrition*, vol. 52, no. 9, pp. 737–760, 2012.

[25] J. B. Carruther and J. M. Kahn, "Angle diversity for nondirected wireless infrared communication," *IEEE Transactions on Communications*, vol. 48, no. 6, pp. 960–969, 2000.

[26] V. Jungnickel, V. Pohl, S. Nonnig, and C. Von Helmolt, "A physical model of the wireless infrared communication channel," *IEEE Journal on Selected Areas in Communications*, vol. 20, no. 3, pp. 631–640, 2002.

[27] K. J. Buettner and C. D. Kern, "The determination of infrared emissivities of terrestrial surfaces," *Journal of Geophysical Research*, vol. 70, no. 6, pp. 1329–1337, 1965.

[28] R. H. Kingston, *Detection of optical and infrared radiation*, vol. 10. Springer, 2013.

[29] P. Capper and C. T. Elliott, *Infrared detectors and emitters: materials and devices*, vol. 8. Springer Science & Business Media, 2013.

[30] J. D. Vincent, *Fundamentals of infrared detector operation and testing*. 1990.

[31] H. Budzier and G. Gerlach, *Thermal infrared sensors: theory, optimisation and practice*. John Wiley & Sons, 2011.

[32] S. Sedky, P. Fiorini, K. Baert, L. Hermans, and R. Mertens, "Characterization and optimization of infrared poly SiGe bolometers," *IEEE transactions on Electron Devices*, vol. 46, no. 4, pp. 675–682, 1999.

[33] N. Nelms and J. Dowson, "Goldblack coating for thermal infrared detectors," *Sensors and Actuators A: Physical*, vol. 120, no. 2, pp. 403–407, 2005.

[34] A. Rogalski, "Recent progress in infrared detector technologies," *Infrared Physics & Technology*, vol. 54, no. 3, pp. 136–154, 2011.

[35] S. Komiyama, O. Astafiev, V. Antonov, T. Kutsuwa, and H. Hirai, "A single-photon detector in the far-infrared range," *Nature*, vol. 403, no. 6768, pp. 405–407, 2000.

[36] Z. L. Yuan, B. E. Kardynal, A. W. Sharpe, and A. J. Shields, "High speed single photon detection in the near infrared," *Applied Physics Letters*, vol. 91, no. 4, p. 041114, 2007.

[37] B. S. Karasik, A. V. Sergeev, and D. E. Prober, "Nanobolometers for THz photon detection," *IEEE Transactions on Terahertz Science and Technology*, vol. 1, no. 1, pp. 97–111, 2011.

[38] A. Rogalski, "History of infrared detectors," *Opto-Electronics Review*, vol. 20, no. 3, pp. 279–308, 2012.

[39] A. Rogalski, "Infrared detectors: status and trends," *Progress in quantum electronics*, vol. 27, no. 2–3, pp. 59–210, 2003.

[40] L. Novotny and N. Van Hulst, "Antennas for light," *Nature photonics*, vol. 5, no. 2, p. 83, 2011.

[41] P. Muehlschlegel, H.-J. Eisler, O. J. Martin, B. Hecht, and D. W. Pohl, "Resonant optical antennas," *science*, vol. 308, no. 5728, pp. 1607–1609, 2005.

[42] H. Fischer and O. J. Martin, "Engineering the optical response of plasmonic nanoantennas," *Optics express*, vol. 16, no. 12, pp. 9144–9154, 2008.

[43] Y. Yifat, M. Ackerman, and P. Guyot-Sionnest, "Mid-IR colloidal quantum dot detectors enhanced by optical nano-antennas," *Applied Physics Letters*, vol. 110, no. 4, p. 041106, 2017.

[44] T. Kemsri *et al.*, "Angular-dependent photodetection enhancement by a metallic circular disk optical antenna," *AIP Advances*, vol. 7, no. 2, p. 025013, 2017.

[45] N. Mojaverian, G. Gu, and X. Lu, "A plasmonic dipole optical antenna coupled quantum dot infrared photodetector," *Journal of Physics D: Applied Physics*, vol. 48, no. 47, p. 475102, 2015.

[46] D. P. Fromm, A. Sundaramurthy, P. J. Schuck, G. Kino, and W. E. Moerner, "Gap-dependent optical coupling of single 'bowtie' nanoantennas resonant in the visible," *Nano letters*, vol. 4, no. 5, pp. 957–961, 2004.

[47] S. Dodson, M. Haggui, R. Bachelot, J. Plain, S. Li, and Q. Xiong, "Optimizing electromagnetic hotspots in plasmonic bowtie nanoantennae," *The journal of physical chemistry letters*, vol. 4, no. 3, pp. 496–501, 2013.

[48] L. Lin and Y. Zheng, "Optimizing plasmonic nanoantennas via coordinated multiple coupling," *Scientific reports*, vol. 5, p. 14788, 2015.

[49] J. Hao, J. Wang, X. Liu, W. J. Padilla, L. Zhou, and M. Qiu, "High performance optical absorber based on a plasmonic metamaterial," *Applied Physics Letters*, vol. 96, no. 25, p. 251104, 2010.

[50] C. Wu *et al.*, "Large-area wide-angle spectrally selective plasmonic absorber," *Physical Review B*, vol. 84, no. 7, p. 075102, 2011.

[51] D. Sievenpiper, L. Zhang, R. F. Broas, N. G. Alexopolous, and E. Yablonovitch, "High-impedance electromagnetic surfaces with a forbidden frequency band," *IEEE Transactions on Microwave Theory and techniques*, vol. 47, no. 11, pp. 2059–2074, 1999.

[52] H. Mosallaei and K. Sarabandi, "Antenna miniaturization and bandwidth enhancement using a reactive impedance substrate," *IEEE Transactions on antennas and propagation*, vol. 52, no. 9, pp. 2403–2414, 2004.

[53] D. H. Schaubert, D. M. Pozar, and A. Adrian, "Effect of microstrip antenna substrate thickness and permittivity: comparison of theories with experiment," *IEEE Transactions on Antennas and Propagation*, vol. 37, no. 6, pp. 677–682, 1989.

[54] L. V. Brown, X. Yang, K. Zhao, B. Y. Zheng, P. Nordlander, and N. J. Halas, "Fan-shaped gold nanoantennas above reflective substrates for surface-enhanced infrared absorption (SEIRA)," *Nano letters*, vol. 15, no. 2, pp. 1272–1280, 2015.

[55] S. Ogawa and M. Kimata, "Metal-insulator-metal-based plasmonic metamaterial absorbers at visible and infrared wavelengths: A review," *Materials*, vol. 11, no. 3, p. 458, 2018.

[56] F. J. González and G. D. Boreman, "Comparison of dipole, bowtie, spiral and log-periodic IR antennas," *Infrared Physics & Technology*, vol. 46, no. 5, pp. 418–428, 2005.

[57] P. Esfandiari *et al.*, "Tunable antenna-coupled metal-oxide-metal (MOM) uncooled IR detector," in *Infrared Technology and Applications XXXI*, 2005, vol. 5783, pp. 470–482.

[58] J. A. Bean, A. Weeks, and G. D. Boreman, "Performance Optimization of Antenna-Coupled AlOx-Pt Tunnel Diode Infrared Detectors," *IEEE Journal of Quantum Electronics*, vol. 47, no. 1, pp. 126–135, 2010.

[59] G. Jayaswal, A. Belkadi, A. Meredov, B. Pelz, G. Moddel, and A. Shamim, "Optical rectification through an Al2O3 based MIM passive rectenna at 28.3 THz," *Materials Today Energy*, vol. 7, pp. 1–9, Mar. 2018, doi: 10.1016/j.mtener.2017.11.002.

[60] A. Sundaramurthy, K. B. Crozier, G. S. Kino, D. P. Fromm, P. J. Schuck, and W. E. Moerner, "Field enhancement and gap-dependent resonance in a system of two opposing tip-to-tip Au nanotriangles," *Physical Review B*, vol. 72, no. 16, p. 165409, 2005.

[61] E. Cubukcu, N. Yu, E. J. Smythe, L. Diehl, K. B. Crozier, and F. Capasso, "Plasmonic laser antennas and related devices," *IEEE Journal of Selected Topics in Quantum Electronics*, vol. 14, no. 6, pp. 1448–1461, 2008.

[62] A. Kinkhabwala, Z. Yu, S. Fan, Y. Avlasevich, K. Müllen, and W. E. Moerner, "Large single-molecule fluorescence enhancements produced by a bowtie nanoantenna," *Nature Photonics*, vol. 3, no. 11, p. 654, 2009.

[63] L. Tang *et al.*, "Nanometre-scale germanium photodetector enhanced by a near-infrared dipole antenna," *Nature Photonics*, vol. 2, no. 4, p. 226, 2008.

[64] N. Liu, M. Mesch, T. Weiss, M. Hentschel, and H. Giessen, "Infrared perfect absorber and its application as plasmonic sensor," *Nano letters*, vol. 10, no. 7, pp. 2342–2348, 2010.

[65] J. Chen *et al.*, "Optical cavity-enhanced localized surface plasmon resonance for high-quality sensing," *IEEE Photonics Technology Letters*, vol. 30, no. 8, pp. 728–731, 2018.

[66] L. Dong *et al.*, "Nanogapped Au antennas for ultrasensitive surface-enhanced infrared absorption spectroscopy," *Nano letters*, vol. 17, no. 9, pp. 5768–5774, 2017.

[67] M. Gallo, L. Mescia, O. Losito, M. Bozzetti, and F. Prudenzano, "Design of optical antenna for solar energy collection," *Energy*, vol. 39, no. 1, pp. 27–32, 2012.

[68] B. Pelz and G. Moddel, "Demonstration of distributed capacitance compensation in a metal-insulator-metal infrared rectenna incorporating a traveling-wave diode," *Journal of Applied Physics*, vol. 125, no. 23, p. 234502, 2019.

[69] S. Kim, J. Jin, Y.-J. Kim, I.-Y. Park, Y. Kim, and S.-W. Kim, "High-harmonic generation by resonant plasmon field enhancement," *Nature*, vol. 453, no. 7196, p. 757, 2008.

[70] Y. Chu and K. B. Crozier, "Experimental study of the interaction between localized and propagating surface plasmons," *Optics letters*, vol. 34, no. 3, pp. 244–246, 2009.

[71] K. Sarabandi and S. Choi, "Design optimization of bowtie nanoantenna for high-efficiency thermophotovoltaics," *Journal of Applied Physics*, vol. 114, no. 21, p. 214303, 2013.

[72] B. Wang, S. C. Singh, H. Lu, and C. Guo, "Design of Aluminum Bowtie Nanoantenna Array with Geometrical Control to Tune LSPR from UV to Near-IR for Optical Sensing," *Plasmonics*, pp. 1–13, 2019.

[73] C. Feuillet-Palma, Y. Todorov, A. Vasanelli, and C. Sirtori, "Strong near field enhancement in THz nano-antenna arrays," *Scientific reports*, vol. 3, p. 1361, 2013.

[74] T. J. Seok *et al.*, "Radiation engineering of optical antennas for maximum field enhancement," *Nano letters*, vol. 11, no. 7, pp. 2606–2610, 2011.

[75] L. Wang, L. Cai, J. Zhang, W. Bai, H. Hu, and G. Song, "Design of plasmonic bowtie nanoring array with high sensitivity and reproducibility for surface-enhanced Raman scattering spectroscopy," *Journal of Raman Spectroscopy*, vol. 42, no. 6, pp. 1263–1266, 2011.

[76] H. Chen, A. M. Bhuiya, R. Liu, D. M. Wasserman, and K. C. Toussaint Jr, "Design, fabrication, and characterization of near-IR gold bowtie nanoantenna arrays," *The Journal of Physical Chemistry C*, vol. 118, no. 35, pp. 20553–20558, 2014.

[77] K. D. Ko *et al.*, "Nonlinear optical response from arrays of Au bowtie nanoantennas," *Nano letters*, vol. 11, no. 1, pp. 61–65, 2010.

[78] B. J. Roxworthy and K. C. Toussaint, "Simultaneously tuning the electric and magnetic plasmonic response using capped bi-metallic nanoantennas," *Nanoscale*, vol. 6, no. 4, pp. 2270–2274, 2014.

[79] R. Fernández-García, Y. Sonnefraud, A. I. Fernández-Domínguez, V. Giannini, and S. A. Maier, "Design considerations for near-field enhancement in optical antennas," *Contemporary Physics*, vol. 55, no. 1, pp. 1–11, 2014.

[80] S. Zou, N. Janel, and G. C. Schatz, "Silver nanoparticle array structures that produce remarkably narrow plasmon lineshapes," *The Journal of chemical physics*, vol. 120, no. 23, pp. 10871–10875, 2004.

[81] Y. Chu, E. Schonbrun, T. Yang, and K. B. Crozier, "Experimental observation of narrow surface plasmon resonances in gold nanoparticle arrays," *Applied Physics Letters*, vol. 93, no. 18, p. 181108, 2008.

[82] B. Auguié and W. L. Barnes, "Collective resonances in gold nanoparticle arrays," *Physical review letters*, vol. 101, no. 14, p. 143902, 2008.

[83] F. Zhou, Y. Liu, and W. Cai, "Huge local electric field enhancement in hybrid plasmonic arrays," *Optics letters*, vol. 39, no. 5, pp. 1302–1305, 2014.

[84] A. El Eter, T. Grosjean, P. Viktorovitch, X. Letartre, T. Benyattou, and F. I. Baida, "Huge light-enhancement by coupling a bowtie nano-antenna's plasmonic resonance to a photonic crystal mode," *Optics express*, vol. 22, no. 12, pp. 14464–14472, 2014.

[85] J. Hao, L. Zhou, and M. Qiu, "Nearly total absorption of light and heat generation by plasmonic metamaterials," *Physical Review B*, vol. 83, no. 16, p. 165107, 2011.

[86] Y. Li, D. Li, C. Chi, and B. Huang, "Achieving strong field enhancement and light absorption simultaneously with plasmonic nanoantennas exploiting film-coupled triangular nanodisks," *The Journal of Physical Chemistry C*, vol. 121, no. 30, pp. 16481–16490, 2017.

[87] R. Alaee *et al.*, "Deep-subwavelength plasmonic nanoresonators exploiting extreme coupling," *Nano letters*, vol. 13, no. 8, pp. 3482–3486, 2013.

[88] F. Yang and Y. Rahmat-Samii, "Reflection phase characterizations of the EBG ground plane for low profile wire antenna applications," *IEEE Transactions on antennas and propagation*, vol. 51, no. 10, pp. 2691–2703, 2003.

[89] Y. Dong, H. Toyao, and T. Itoh, "Compact circularly-polarized patch antenna loaded with metamaterial structures," *IEEE transactions on antennas and propagation*, vol. 59, no. 11, pp. 4329–4333, 2011.

[90] S. N. Burokur, A.-C. Lepage, S. Varault, X. Begaud, G.-P. Piau, and A. De Lustrac, "Low-profile metamaterial-based L-band antennas," *Applied Physics A*, vol. 122, no. 4, p. 326, 2016.

[91] M. K. Anam and S. Choi, "Perfect Absorption Efficiency Circular Nanodisk Array Integrated with a Reactive Impedance Surface with High Field Enhancement," *Nanomaterials*, vol. 10, no. 2, p. 258, 2020.

[92] I. H. Malitson, "Interspecimen comparison of the refractive index of fused silica," *Josa*, vol. 55, no. 10, pp. 1205–1209, 1965.

[93] C. Z. Tan, "Determination of refractive index of silica glass for infrared wavelengths by IR spectroscopy," *Journal of Non-Crystalline Solids*, vol. 223, no. 1–2, pp. 158–163, 1998.

[94] P. B. Johnson and R.-W. Christy, "Optical constants of the noble metals," *Physical review B*, vol. 6, no. 12, p. 4370, 1972.

[95] M. Walther, D. G. Cooke, C. Sherstan, M. Hajar, M. R. Freeman, and F. A. Hegmann, "Terahertz conductivity of thin gold films at the metal-insulator percolation transition," *Physical Review B*, vol. 76, no. 12, p. 125408, 2007.

[96] Y. Sonnefraud *et al.*, "Experimental realization of subradiant, superradiant, and Fano resonances in ring/disk plasmonic nanocavities," *ACS nano*, vol. 4, no. 3, pp. 1664–1670, 2010.

[97] M. Decker *et al.*, "Dual-channel spontaneous emission of quantum dots in magnetic metamaterials," *Nature communications*, vol. 4, p. 2949, 2013.

[98] S. A. Maier, "Plasmonic field enhancement and SERS in the effective mode volume picture," *Optics Express*, vol. 14, no. 5, pp. 1957–1964, 2006.

[99] R. F. Oulton, V. J. Sorger, D. A. Genov, D. F. P. Pile, and X. Zhang, "A hybrid plasmonic waveguide for subwavelength confinement and long-range propagation," *nature photonics*, vol. 2, no. 8, p. 496, 2008.

[100] K. Arik, S. Abdollahramezani, S. Farajollahi, A. Khavasi, and B. Rejaei, "Design of mid-infrared ultra-wideband metallic absorber based on circuit theory," *Optics Communications*, vol. 381, pp. 309–313, 2016.

[101] B. Lee *et al.*, "Fano resonance and spectrally modified photoluminescence enhancement in monolayer MoS2 integrated with plasmonic nanoantenna array," *Nano letters*, vol. 15, no. 5, pp. 3646–3653, 2015.

[102] R. Méjard *et al.*, "Advanced engineering of single-crystal gold nanoantennas," *Optical Materials Express*, vol. 7, no. 4, pp. 1157–1168, 2017.

[103] A. Trügler, J.-C. Tinguely, G. Jakopic, U. Hohenester, J. R. Krenn, and A. Hohenau, "Near-field and SERS enhancement from rough plasmonic nanoparticles," *Physical Review B*, vol. 89, no. 16, p. 165409, 2014.

[104] K.-P. Chen, V. P. Drachev, J. D. Borneman, A. V. Kildishev, and V. M. Shalaev, "Drude Relaxation Rate in Grained Gold Nanoantennas," *Nano Lett.*, vol. 10, no. 3, pp. 916–922, Mar. 2010, doi: 10.1021/nl9037246.

[105] A. F. Mayadas and M. Shatzkes, "Electrical-resistivity model for polycrystalline films: the case of arbitrary reflection at external surfaces," *Physical review B*, vol. 1, no. 4, p. 1382, 1970.

[106] J. Cesario, R. Quidant, G. Badenes, and S. Enoch, "Electromagnetic coupling between a metal nanoparticle grating and a metallic surface," *Optics letters*, vol. 30, no. 24, pp. 3404–3406, 2005.

[107] X. Lu, L. Zhang, and T. Zhang, "Nanoslit-microcavity-based narrow band absorber for sensing applications," *Optics express*, vol. 23, no. 16, pp. 20715–20720, 2015.

[108] C. Chen, G. Wang, Z. Zhang, and K. Zhang, "Dual narrow-band absorber based on metal–insulator–metal configuration for refractive index sensing," *Optics letters*, vol. 43, no. 15, pp. 3630–3633, 2018.

[109] U. K. Chettiar, A. V. Kildishev, T. A. Klar, and V. M. Shalaev, "Negative index metamaterial combining magnetic resonators with metal films," *Optics Express*, vol. 14, no. 17, pp. 7872–7877, 2006.

[110] Y. Cui *et al.*, "A thin film broadband absorber based on multi-sized nanoantennas," *Applied Physics Letters*, vol. 99, no. 25, p. 253101, 2011.

[111] H.-H. Chen *et al.*, "A plasmonic infrared photodetector with narrow bandwidth absorption," *Applied Physics Letters*, vol. 105, no. 2, p. 023109, 2014.

[112] J. Y. Suen *et al.*, "Multifunctional metamaterial pyroelectric infrared detectors," *Optica*, vol. 4, no. 2, pp. 276–279, 2017.

[113] D. Hasan and C. Lee, "Hybrid Metamaterial Absorber Platform for Sensing of CO_2 Gas at Mid-IR," *Advanced Science*, vol. 5, no. 5, p. 1700581, 2018.

[114] A. Cattoni *et al.*, "λ3/1000 plasmonic nanocavities for biosensing fabricated by soft UV nanoimprint lithography," *Nano letters*, vol. 11, no. 9, pp. 3557–3563, 2011.

[115] C.-Y. Chang *et al.*, "Flexible Localized Surface Plasmon Resonance Sensor with Metal–Insulator–Metal Nanodisks on PDMS Substrate," *Scientific reports*, vol. 8, no. 1, p. 11812, 2018.

[116] K. Chen, T. D. Dao, S. Ishii, M. Aono, and T. Nagao, "Infrared Aluminum Metamaterial Perfect Absorbers for Plasmon-Enhanced Infrared Spectroscopy," *Advanced Functional Materials*, vol. 25, no. 42, pp. 6637–6643, 2015.

[117] E. Aslan, E. Aslan, M. Turkmen, and O. G. Saracoglu, "Metamaterial plasmonic absorber for reducing the spectral shift between near-and far-field responses in surface-enhanced spectroscopy applications," *Sensors and Actuators A: Physical*, vol. 267, pp. 60–69, 2017.

[118] J. B. Lassiter *et al.*, "Third-harmonic generation enhancement by film-coupled plasmonic stripe resonators," *Acs Photonics*, vol. 1, no. 11, pp. 1212–1217, 2014.

[119] Y. Chu, M. G. Banaee, and K. B. Crozier, "Double-resonance plasmon substrates for surface-enhanced Raman scattering with enhancement at excitation and stokes frequencies," *ACS nano*, vol. 4, no. 5, pp. 2804–2810, 2010.

[120] W. Cui *et al.*, "Hybrid Nanodisk Film for Ultra-Narrowband Filtering, Near-Perfect Absorption and Wide Range Sensing," *Nanomaterials*, vol. 9, no. 3, p. 334, 2019.

[121] P. Bouchon, C. Koechlin, F. Pardo, R. Haïdar, and J.-L. Pelouard, "Wideband omnidirectional infrared absorber with a patchwork of plasmonic nanoantennas," *Optics letters*, vol. 37, no. 6, pp. 1038–1040, 2012.

[122] S. Butun and K. Aydin, "Structurally tunable resonant absorption bands in ultrathin broadband plasmonic absorbers," *Optics express*, vol. 22, no. 16, pp. 19457–19468, 2014.

[123] A. Ghobadi, H. Hajian, A. R. Rashed, B. Butun, and E. Ozbay, "Tuning the metal filling fraction in metal-insulator-metal ultra-broadband perfect absorbers to maximize the absorption bandwidth," *Photonics Research*, vol. 6, no. 3, pp. 168–176, 2018.

[124] S. Zou and G. C. Schatz, "Theoretical studies of plasmon resonances in one-dimensional nanoparticle chains: narrow lineshapes with tunable widths," *Nanotechnology*, vol. 17, no. 11, p. 2813, 2006.

[125] B. C. Yildiz, M. Habib, A. R. Rashed, and H. Caglayan, "Hybridized plasmon modes in a system of metal thin film–nanodisk array," *Journal of Applied Physics*, vol. 126, no. 11, p. 113104, 2019.

[126] T. T. Van Nguyen, X. Xie, J. Xu, Y. Wu, M. Hong, and X. Liu, "Plasmonic bimetallic nanodisk arrays for DNA conformation sensing," *Nanoscale*, vol. 11, no. 41, pp. 19291–19296, 2019.

[127] B. Zhang and J. Guo, "Optical properties of a two-dimensional nanodisk array with super-lattice defects," *JOSA B*, vol. 30, no. 11, pp. 3011–3017, 2013.

[128] C.-W. Cheng, M. N. Abbas, C.-W. Chiu, K.-T. Lai, M.-H. Shih, and Y.-C. Chang, "Wide-angle polarization independent infrared broadband absorbers based on metallic multi-sized disk arrays," *Optics express*, vol. 20, no. 9, pp. 10376–10381, 2012.

[129] S. Jagtap, A. Chaudhari, N. Chaskar, S. Kharche, and R. K. Gupta, "A wideband microstrip array design using RIS and PRS layers," *IEEE Antennas and Wireless Propagation Letters*, vol. 17, no. 3, pp. 509–512, 2018.

[130] S. Butun, S. Tongay, and K. Aydin, "Enhanced light emission from large-area monolayer MoS2 using plasmonic nanodisc arrays," *Nano letters*, vol. 15, no. 4, pp. 2700–2704, 2015.

[131] W. Li and Y. Hou, "Electromagnetic field hugely enhanced by coupling to optical energy focusing structure," *Optics express*, vol. 25, no. 7, pp. 7358–7368, 2017.

[132] Y. Bao, Y. Hou, and Z. Wang, "Huge electric field enhancement of magnetic resonator integrated with multiple concentric rings," *Plasmonics*, vol. 10, no. 2, pp. 251–256, 2015.

[133] B. J. Lee, L. P. Wang, and Z. M. Zhang, "Coherent thermal emission by excitation of magnetic polaritons between periodic strips and a metallic film," *Optics Express*, vol. 16, no. 15, pp. 11328–11336, 2008.

[134] P. G. Etchegoin and E. C. Le Ru, "A perspective on single molecule SERS: current status and future challenges," *Physical Chemistry Chemical Physics*, vol. 10, no. 40, pp. 6079–6089, 2008.

[135] E. C. Le Ru, E. Blackie, M. Meyer, and P. G. Etchegoin, "Surface enhanced Raman scattering enhancement factors: a comprehensive study," *The Journal of Physical Chemistry C*, vol. 111, no. 37, pp. 13794–13803, 2007.

[136] C. Yang *et al.*, "Angle robust reflection/transmission plasmonic filters using ultrathin metal patch array," *Advanced Optical Materials*, vol. 4, no. 12, pp. 1981–1986, 2016.

[137] D. Chen, J. Zhou, M. Rippa, and L. Petti, "Structure-dependent localized surface plasmon resonance characteristics and surface enhanced Raman scattering performances of quasi-periodic nanoarrays: measurements and analysis," *Journal of Applied Physics*, vol. 118, no. 16, p. 163101, 2015.

[138] A. Kabiri, E. Girgis, and F. Capasso, "Buried nanoantenna arrays: versatile antireflection coating," *Nano letters*, vol. 13, no. 12, pp. 6040–6047, 2013.

[139] D. H. Kim, H. J. Lee, H. Jeong, B. Shong, W.-H. Kim, and T. J. Park, "Thermal Atomic Layer Deposition of Device-Quality SiO$_2$ Thin Films under 100° C Using an Aminodisilane Precursor," *Chemistry of Materials*, vol. 31, no. 15, pp. 5502–5508, 2019.

[140] Y.-S. Lee, D. Choi, B. Shong, S. Oh, and J.-S. Park, "Low temperature atomic layer deposition of SiO$_2$ thin films using di-isopropylaminosilane and ozone," *Ceramics International*, vol. 43, no. 2, pp. 2095–2099, 2017.

[141] P. Díaz-Núñez *et al.*, "On the Large Near-Field Enhancement on Nanocolumnar Gold Substrates," *Scientific reports*, vol. 9, no. 1, pp. 1–10, 2019.

[142] A. P. Raman, "Thermal light tunnels its way into electricity," *Science*, vol. 367, no. 6484, pp. 1301–1302, 2020.

[143] Y. Bi *et al.*, "Solution processed infrared-and thermo-photovoltaics based on 0.7 eV bandgap PbS colloidal quantum dots," *Nanoscale*, vol. 11, no. 3, pp. 838–843, 2019.

[144] C.-C. Chang *et al.*, "High-temperature refractory metasurfaces for solar thermophotovoltaic energy harvesting," *Nano letters*, vol. 18, no. 12, pp. 7665–7673, 2018.

[145] W. E. S. W. A. Rashid, P. J. Ker, M. Z. B. Jamaludin, M. M. A. Gamel, H. J. Lee, and N. B. Abd Rahman, "Recent development of thermophotovoltaic system for waste heat harvesting application and potential implementation in thermal power plant," *IEEE Access*, vol. 8, pp. 105156–105168, 2020.

[146] M. N. Gadalla, M. Abdel-Rahman, and A. Shamim, "Design, optimization and fabrication of a 28.3 THz nano-rectenna for infrared detection and rectification," *Scientific reports*, vol. 4, p. 4270, 2014.

[147] A. Y. Elsharabasy, A. S. Negm, M. H. Bakr, and M. J. Deen, "Global optimization of rectennas for IR energy harvesting at 10.6 μm," *IEEE Journal of Photovoltaics*, vol. 9, no. 5, pp. 1232–1239, 2019.

[148] A. Belkadi, A. Weerakkody, and G. Moddel, "Large errors from assuming equivalent dc and high-frequency electrical characteristics in metal–multiple-insulator–metal diodes," *ACS Photonics*, vol. 5, no. 12, pp. 4776–4780, 2018.

[149] D. M. Rowe, *CRC handbook of thermoelectrics*. CRC press, 2018.

[150] E. Briones *et al.*, "Seebeck nanoantennas for solar energy harvesting," *Applied Physics Letters*, vol. 105, no. 9, p. 093108, 2014.

[151] E. Briones, R. Ruiz-Cruz, J. Briones, and J. Simon, "Optimization of Seebeck nanoantenna-based infrared harvesters," *Optics Express*, vol. 28, no. 1, pp. 116–129, 2020.

[152] A. Cuadrado, E. Briones, F. J. González, and J. Alda, "Polarimetric pixel using Seebeck nanoantennas," *Optics express*, vol. 22, no. 11, pp. 13835–13845, 2014.

[153] E. Briones, C. Kuri, I. Cortes-Mestizo, J. Briones, and H. Vilchis, "Numerical conversion efficiency of thermally isolated Seebeck nanoantennas," *AIP Advances*, vol. 6, no. 11, p. 115018, 2016.

[154] B. N. Tiwari, P. J. Fay, G. H. Bernstein, A. O. Orlov, and W. Porod, "Effect of read-out interconnects on the polarization characteristics of nanoantennas for the long-wave infrared regime," *IEEE transactions on nanotechnology*, vol. 12, no. 2, pp. 270–275, 2013.

[155] G. P. Szakmany, A. O. Orlov, G. H. Bernstein, and W. Porod, "Response increase of antenna-coupled nanothermocouples by thermal insulation," *Journal of Vacuum Science & Technology B, Nanotechnology and Microelectronics: Materials, Processing, Measurement, and Phenomena*, vol. 36, no. 5, p. 052203, 2018.

[156] G. P. Szakmany, A. O. Orlov, G. H. Bernstein, and W. Porod, "Polarization-dependent response of single-and bi-metal antenna-coupled thermopiles for infrared detection," *IEEE Transactions on Terahertz Science and Technology*, vol. 5, no. 6, pp. 884–891, 2015.

[157] G. P. Szakmany, A. O. Orlov, G. H. Bernstein, and W. Porod, "Fabrication of suspended antenna-coupled nanothermocouples," *Journal of Vacuum Science & Technology B, Nanotechnology and Microelectronics: Materials, Processing, Measurement, and Phenomena*, vol. 37, no. 5, p. 052201, 2019.

[158] G. P. Szakmany, A. O. Orlov, G. H. Bernstein, and W. Porod, "Cavity-Backed Antenna-Coupled Nanothermocouples," *Scientific reports*, vol. 9, no. 1, pp. 1–7, 2019.

[159] D. R. Lide, *CRC handbook of chemistry and physics*, vol. 85. CRC press, 2004.

[160] B. Mora-Ventura, J. E. Sánchez, G. González, and F. J. González, "Thermal impedance analysis of nano-dipole linear arrays for energy harvesting applications," *Infrared Physics & Technology*, p. 103332, 2020.

[161] J. Kischkat *et al.*, "Mid-infrared optical properties of thin films of aluminum oxide, titanium dioxide, silicon dioxide, aluminum nitride, and silicon nitride," *Applied optics*, vol. 51, no. 28, pp. 6789–6798, 2012.

[162] M. A. Ordal, R. J. Bell, R. W. Alexander, L. L. Long, and M. R. Querry, "Optical properties of Au, Ni, and Pb at submillimeter wavelengths," *Applied Optics*, vol. 26, no. 4, pp. 744–752, 1987.

[163] M. A. Ordal, R. J. Bell, R. W. Alexander, L. A. Newquist, and M. R. Querry, "Optical properties of Al, Fe, Ti, Ta, W, and Mo at submillimeter wavelengths," *Applied optics*, vol. 27, no. 6, pp. 1203–1209, 1988.

[164] A. Alu and N. Engheta, "Input impedance, nanocircuit loading, and radiation tuning of optical nanoantennas," *Physical review letters*, vol. 101, no. 4, p. 043901, 2008.

[165] G. Baffou, R. Quidant, and C. Girard, "Heat generation in plasmonic nanostructures: Influence of morphology," *Applied Physics Letters*, vol. 94, no. 15, p. 153109, 2009.

[166] L. Khosravi Khorashad, L. V. Besteiro, Z. Wang, J. Valentine, and A. O. Govorov, "Localization of excess temperature using plasmonic hot spots in metal nanostructures: combining nano-optical antennas with the Fano effect," *The Journal of Physical Chemistry C*, vol. 120, no. 24, pp. 13215–13226, 2016.

[167] G. P. Szakmany, P. M. Krenz, A. O. Orlov, G. H. Bernstein, and W. Porod, "Antenna-coupled nanowire thermocouples for infrared detection," *IEEE Transactions on Nanotechnology*, vol. 12, no. 2, pp. 163–167, 2012.

[168] C. A. Balanis, *Antenna theory: analysis and design*. John wiley & sons, 2015.

[169] C. Herring and M. H. Nichols, "Thermionic emission," *Reviews of modern physics*, vol. 21, no. 2, p. 185, 1949.

[170] E. L. Murphy and R. H. Good Jr, "Thermionic emission, field emission, and the transition region," *Physical review*, vol. 102, no. 6, p. 1464, 1956.

[171] J. A. Bean, B. Tiwari, G. H. Bernstein, P. Fay, and W. Porod, "Thermal infrared detection using dipole antenna-coupled metal-oxide-metal diodes," *Journal of Vacuum Science & Technology B: Microelectronics and Nanometer Structures Processing, Measurement, and Phenomena*, vol. 27, no. 1, pp. 11–14, 2009.

[172] P. M. Mendes *et al.*, "Gold nanoparticle patterning of silicon wafers using chemical e-beam lithography," *Langmuir*, vol. 20, no. 9, pp. 3766–3768, 2004.

[173] W. Yue *et al.*, "Electron-beam lithography of gold nanostructures for surface-enhanced Raman scattering," *Journal of Micromechanics and Microengineering*, vol. 22, no. 12, p. 125007, 2012.

[174] M. H. Werts, M. Lambert, J.-P. Bourgoin, and M. Brust, "Nanometer scale patterning of Langmuir- Blodgett films of gold nanoparticles by electron beam lithography," *Nano Letters*, vol. 2, no. 1, pp. 43–47, 2002.

[175] M. F. Ceiler, P. A. Kohl, and S. A. Bidstrup, "Plasma-enhanced chemical vapor deposition of silicon dioxide deposited at low temperatures," *Journal of the Electrochemical Society*, vol. 142, no. 6, p. 2067, 1995.

[176] B. Shokri, M. A. Firouzjah, and S. I. Hosseini, "FTIR analysis of silicon dioxide thin film deposited by metal organic-based PECVD," in *Proceedings of 19th international symposium on plasma chemistry society*, 2009, vol. 2631, pp. 26–31.

[177] S. K. Ray, C. K. Maiti, S. K. Lahiri, and N. B. Chakrabarti, "TEOS-based PECVD of silicon dioxide for VLSI applications," *Advanced materials for optics and electronics*, vol. 6, no. 2, pp. 73–82, 1996.

[178] C.-C. Hu, W. Yang, Y.-T. Tsai, and Y.-F. Chau, "Gap enhancement and transmittance spectra of a periodic bowtie nanoantenna array buried in a silica substrate," *Optics Communications*, vol. 324, pp. 227–233, 2014.

[179] A. E. Klein, N. Janunts, M. Steinert, A. Tünnermann, and T. Pertsch, "Polarization-resolved near-field mapping of plasmonic aperture emission by a dual-SNOM system," *Nano letters*, vol. 14, no. 9, pp. 5010–5015, 2014.

[180] R. L. Olmon *et al.*, "Determination of electric-field, magnetic-field, and electric-current distributions of infrared optical antennas: a near-field optical vector network analyzer," *Physical review letters*, vol. 105, no. 16, p. 167403, 2010.